FACULTY OF SCIENCES

People's Democratic Republic of Algeria
Ministry of Higher Education and Scientific Research
Setif 1 University – Ferhat ABBAS
Faculty of Sciences
Department of Physics

Setif 1 University - Ferhat ABBAS

Thesis

Submitted in candidacy for the degree of

LMD DOCTORATE

Section of Physics

Option: Material physics

By: **Rima KICHE**

Titled

Elaboration of new molecular materials using bottom-up and self-assembly approaches with multiple optical, thermodynamic and thermal properties: experimental and theoretical approach

In front of the jury:

Pr. Noureddine BENOUATTAS	Setif 1 university	Chairperson
Dr. Louiza OUKSEL	Setif 1 university	Supervisor
Dr. Riadh BOURZAMI	Setif 1 university	Co-Supervisor
Pr. Laid KERKACHE	Setif 1 university	Examiner
Pr. Saifi ISSAADI	Setif 1 university	Examiner
Pr. Douniazed HANNACHI	Batna 1 universiy	Examiner

-June 24, 2025-

Acknowledgment

My thanks go first to Allah, the almighty and most merciful who enabled me to complete my studies.

To my supervisor Dr. Louiza OUKSEL for accompanying me in the laboratory (Electrochemistry and Materials Laboratory (LEM)), her advices, availability, discussions, providing materials and books, plus her encouragements. I am very grateful.

To my co-supervisor Dr. Riadh BOURZAMI for his teaching in simple and easy way, invaluable discussions, advices, availability, his help, providing helpful books, products and analysis, as well as his encouragements. I am eternally grateful.

I acknowledge, with a great respect the jury members: Pr. Noureddine BENOUATTAS, Pr. Laid KERKACHE, Pr. Saifi ISSAADI and Pr. HANNACHI Douniazed for their confidence in our research work and for kindly accepting to evaluate it. Thank you.

I would like to thank Dr. Mohamed BELHOUCINE for the elaboration and the provision of the ionic liquid materials.

I would like to thank, Dr. Hakima AIT YOUCEF for her advices and her help on elaboration of the hybrid materials, I would like to thank also Pr. Abdelkader. HELLEL for his advices, encouragements, and providing a helpful literature.

Thanks are due to all members: managements, professors, technicians and doctoral students of the LEM laboratory, where the experiments in this work were conducted. The work with them was appreciable.

I would like to thank the emerging materials unit's members where the thermal analysis were conducted, as well as, some theoretical calculations.

I would like to thank the technicians of the Growth and Characterization of New Semiconductors Laboratory (LCCNS) were the infra-red analysis were conducted.

I would like to thank my family mother, father and sisters for their constant moral support and encouragements. All my love for them.

Table of contents

Figure captions i
Scheme captions iv
Table captions v
List of abbreviations vii
General introduction 1
References 3

Chapter I

I. Bibliography 4
I.1 Ionic materials 4
I.1.1 Hybrid organic-inorganic materials 4
I.1.1.1 Definition 4
I.1.1.2 Classification 5
I.1.1.3 Approaches of elaboration 5
I.1.1.4 Common hybrids families 6
I.1.2 Ionic liquids 8
I.1.2.1 Definition 8
I.1.2.2 Elaboration 8
I.1.2.3 Classes of ILs 9
I.1.2.4 Key characteristics and techniques for understanding ILs 10
I.1.2.5 Comparable ILs to the used ones, their properties and some examples of applications 12
I.2 Aims of this work 16
I.3 References 17

Chapter II

II. Experimental and methods 22
II.1 Synthesis 22
II.1.1.1 Ionic organic-inorganic hybrid materials 22
II.1.2 Ionic materials 23
II.1.2.1 Ionic liquids 23

II.1.3 Organic molecules 23
II.2 Analysis techniques 24
II.2.1 Single crystal X-ray diffraction (SXRD) 24
II.2.2 UV–Visible and FT-IR spectroscopies 24
II.2.3 Thermo-gravimetric analysis 24
II.2.4 Atomic force microscopy (AFM) 25
II.3 Applications 25
II.3.1 Corrosion inhibition 25
II.3.1.1 Weight loss measurements 25
II.3.1.2 Electrochemical method 27
II.3.2 Carbon paste electrodes elaboration 28
II.3.2.1 Preparation of carbon paste electrodes (CPEs) 28
II.4 Quantum calculation methods 29
II.4.1 Born-Oppenheimer approximation 30
II.4.2 Hartree approximation 31
II.4.3 Hartree –Fock approximation 31
II.4.4 Density functional theory (DFT) 32
II.4.4.1 Hohenberg–Kohn theorems 32
II.4.4.2 Kohn-Sham approach 33
II.4.4.3 Exchange-correlation functional 33
II.5 Gaussian 34
II.5.1 Molecular Dynamic Simulation 34
II.6 References 36

Chapter III

III. Structural, spectroscopy and thermal properties of ionic organic-inorganic crystal materials 37
III.1 Introduction 37
III.2 First material 37
III.2.1 SXRD study 37
III.2.1.1 3D supra-molecular network 41
III.2.2 Spectroscopy studies 42
III.2.2.1 FT-IR spectroscopy 42

III.2.2.2 UV-Vis. spectroscopy 44
III.2.2.3 Thermo-gravimetric studies 44
III.3 Second material 45
III.3.1 SXRD study 45
III.3.1.1 3D supra-molecular network 49
III.3.2 Spectroscopy studies 51
III.3.2.1 FT-IR spectroscopy 51
III.3.2.2 UV-Visible spectroscopy 52
III.3.3 Thermo-gravimetric studies 53
III.4 Conclusions 53
III.5 References 55

Chapter IV

IV. Structural, spectroscopy, thermal and thermodynamic and NLO properties of three imidazolium based ionic liquids: theoretical and experimental approaches 57
IV.1 Introduction 57
IV.2 Optimized geometries 57
IV.3 Vibrational analysis 60
IV.4 Thermal analysis 62
IV.5 Quantum Chemistry results (DFT) 63
IV.5.1 Molecular orbitals (MOs) 63
IV.5.2 Mapping Electrostatic Potential (MEP), partial charges and dipolar moments 65
IV.5.3 Reactivity and stability 67
IV.5.4 Thermal and thermodynamics properties 68
IV.5.5 Non-linear optical properties (NLO) 70
IV.5.6 Optical properties 72
IV.6 Conclusion 74
IV.7 References 76

Chapter V

V. Corrosion inhibition and carbon paste electrodes elaboration applications 79
V.1 Corrosion inhibition 79
V.1.1 Weight loss measurements 79
V.1.1.1 Organic molecules 79
V.1.1.2 Ionic material 80
V.1.2 Atomic Force Microscopy 81
V.1.2.1 Organic molecules 81
V.1.2.2 Ionic material 83
V.1.3 Electrochemical results 84
V.1.3.1 Polarization studies 84
V.1.3.2 Electrochemical impedance spectroscopy (EIS) 85
V.1.4 Molecular Dynamic Simulation (MDS) 86
V.2 Electronic transport property of ionic liquids 89
V.2.1 Current-voltage characteristic (I-V) 89
V.2.2 Cyclic voltammetry analysis (CV) 90
V.2.3 Electrochemical impedance spectroscopy (EIS) 91
V.2.3.1 Mechanism of conductivity (charge transfer) 93
V.3 Conclusions 93
V.4 References 95
General conclusion 97
Perspectives 99

Figure captions

Chapter I

Figure I. 1. Timeline of the creation and multidisciplinary progress of hybrid materials made of organic and inorganic. 5

Figure I. 2. Top view (001) of the channels in the 3D Co-based organic-inorganic hybrid framework, Co (light blue) O (red), N (blue), C (gray). 6

Figure I. 3. Structure of a typical organic-inorganic phyllosilicate produced via the sol-gel process: d refers to the thickness of the layer and its interlayers. 7

Figure I. 4. 3D supramolecular network of $\{[Pb(H_2IEDC)_2)]\cdot 3H_2O\}n$ building by hydrogen bonding O−H⋯O and Pb⋯H interactions. 8

Figure I. 5. TGA response of $[PC_6C_6C_6C_{14}][N(CN)_2]$, $[PC_6C_6C_6C_{14}][Cl]$ and $[PC_6C_6C_6C_{14}][NTF_2]$ ILs. 12

Figure I. 6. Background current subtracted CV of different concentrated dopamine at 0.1 V in phosphate buffer solution. 14

Figure I. 7. Mechanism of mild steel corrosion inhibition with ImILs in sulphuric acid at (a) Anodic and (b) Cathodic sites. 15

Chapter II

Figure II. 1. Specimens protocol preparation. 26

Figure II. 2. Weight loss measurements protocol. 26

Figure II. 3. A descriptive scheme of the three-electrode cell. 29

Chapter III

Figure III. 1. (a) Asymmetric unit, (b) unit cell. Unit cell provided by (c) inversion centers, (d) screw axes, and (e) glide planes for the 2,4-diamino-6-phenyl-1,3,5-triazinium perchlorate, (f) powder XRD pattern. 38

Figure III. 2. (a) and (b) Supra-molecular chains along (Oa) direction, (c) Supra-molecular parallel-displaced π-stacking formed along (Ob) direction, (d) Supra-molecular network along (Ob) direction. 42

Figure III. 3. FT-IR spectrum of 2,4-diamino-6-phenyl-1,3,5-triazinium perchlorate. 43

Figure III. 4. UV-Vis. electronic spectrum of 2,4-diamino-6-phenyl-1,3,5-triazinium perchlorate. 44

Figure III. 5. TGA/DTG curves of (a) benzoguanamine and (b) 2,4-diamino-6-phenyl-1,3,5-triazinium perchlorite. 45

Figure III. 6. (a) Asymmetric unit (b) unit cell (c) unit cell provided by inversion center (yellow color) for the 2,4,6-triamino-1,3,5-triazin-1,3-dium bisperchlorate monohydrate, (d) powder XRD pattern 46

Figure III. 7. (a) Supramolecular hybrid chain along (Oa) direction illustrating the alternation of the anion and cation molecules, (b) supramolecular hybrid layer along the plan (Oab), (c) inorganic supramolecular chain, (d) supramolecular inorganic layer along the plan (Oab), (e) illustration of the junction between the two hybrid supramolecular chains, provide by the symmetry centers, (f) 3D supramolecular network illustrating lamellar-like structure, (g) remarked supramolecular chains along the direction (1, 0, -3), (h) parallel-displacer stacking of the triazin rings along (Oa) direction. 50

Figure III. 8. FT-IR spectrum of the 2,4,6-triamino-1,3,5-triazin-1,3-dium bisperchlorate monohydrate ($C_3H_8\ N_6^{2+}.2Cl\ O_4^-.H_2O$). 51

Figure III. 9. UV–Visible absorption electronic spectrum of 2,4,6-triamino-1,3,5-triazin-1,3-dium bisperchlorate monohydrate ($C_3H_8\ N_6^{2+}.2Cl\ O_4^-.H_2O$). 52

Figure III. 10. TGA-DTG curves of the 2,4,6-triamino-1,3,5-triazin-1,3-dium bisperchlorate monohydrate ($C_3H_8\ N_6^{2+}.2Cl\ O_4^-.H_2O$). 53

Chapter IV

Figure IV. 1. Optimized molecular structures and angles between the carrying plans for $VBmim^+$ cation (a and b), [$VBmim^+$, Cl^-] (c and d), [$VBmim^+$, PF_6^-] (e and f) and [$VBmim^+$, NTF_2^-] (g and h). 58

Figure IV. 2. Experimental (black) and theoretical (red) FTIR spectra of the following ILs: (a) [$VBmim^+$, Cl^-], (b) [$VBmim^+$, NTF_2^-], and (c) [$VBmim^+$, PF_6^-]. 61

Figure IV. 3. TGA (a) and DSC (b) curves of [$VBmim^+$, PF_6^-] [$VBmim^+$, Cl^-], and [$VBmim^+$, NTF_2^-]. 63

Figure IV. 4. Plots of MOs for [$VBmim^+$, Cl^-], [$VBmim^+$, NTF_2^-] and [$VBmim^+$, PF_6^-]..... 65

Figure IV. 5. (a): Total electron density surfaces mapped with electrostatic potential, (b): partial charges, and (c) dipolar moments of [$VBmim^+$, PF_6^-], [$VBmim^+$, Cl^-], and [$VBmim^+$,NTF_2^-].... 66

Figure IV. 6. Variation of the enthalpy (kJ.mol^{-1}), heat capacity (J.mol^{-1}.K^{-1}) and entropy (J.mol^{-1}.K^{-1}) as function of temperature for (a): [VBmim^{+}, Cl^{-}], (b): [VBmim^{+}, PF$_6^{-}$] and (c): [VBmim^{+}, NTF$_2^{-}$]. 70

Figure IV. 7. UV-Visible absorption spectra and oscillator strength of [VBmim^{+}, Cl^{-}], [VBmim^{+}, PF$_6^{-}$] and [VBmim^{+}, NTF$_2^{-}$]. 73

Chapter V

Figure V. 1. AFM images of the XC48 steel surface, (a) Before immersion, (b) after 24 h immersion in HCl, (c) After 24 h immersion in HCl /0.4 mM DH4MPMP, (d) After 24 h immersion in HCl /0.4 mM H4MPMPA. 82

Figure V. 2. AFM images of the XC48 steel surface, immersion in 1M HCl solution without and with the the 2,4,6-triamino-1,3,5-triazin-1,3-dium bisperchlorate monohydrate inhibitor. 83

Figure V. 3. AFM images of the XC48 steel surface, immersion in 1M HCl solution without and with the [VBmim^{+}, Cl^{-}] inhibitor. 84

Figure V. 4. Tafel curves of XC48 steel obtained at 293 K in HCl 1N solution for various concentrations of (a) DH4MPMP and (b) H4MPMPA. 85

Figure V. 5. Nyquist impedance plots of XC48 steel obtained at 298K in HCl 1N solutions containing different concentrations of (a): DH4MPMP and (b): H4MPMPA. 86

Figure V. 6. Equilibrium configurations of DH4MPMP (d, e, f), H4MPMPA (a, b, c), and water field on the Fe (110) surface. 88

Figure V. 7. Curves of current voltage of CPE, CPE/[VBmim^{+}, Cl^{-}], CPE/[VBmim^{+}, PF$_6^{-}$] and CPE/[VBmim^{+}, NTF$_2^{-}$], in 0.1 M of KCl and 0.1 M of Fe(CN)$_6^{3-/4-}$ solution and a scan rate of 100 mV/s 90

Figure V. 8. Cyclic voltammograms of unmodified CPE and modified CPE with (a):the [VBmim^{+}, Cl^{-}], (b): the [VBmim^{+}, PF$_6^{-}$] and (c): the [VBmim^{+}, NTF$_2^{-}$] in 0.1 M of KCl and 0.1 M of Fe(CN)$_6^{3-/4-}$ solution and a scan rate of 100 mV/s. 91

Figure V. 9. Nyauist plots of unmodified CPE and modified CPEs with (a):the [VBmim^{+}, Cl^{-}], (b): the [VBmim^{+}, PF$_6^{-}$] and (c): the [VBmim^{+}, NTF$_2^{-}$]in 0.1M KCl and 0.1 M Fe(CN)$_6^{3-/4-}$ solution, and a scan rate of 100 mV/s. 92

Figure V. 10. Proposed electrical equivalent circuit. 93

Scheme captions

Chapter I

Scheme I. 1. Typical synthetic pathways for elaborating ionic liquids. 9

Chapter II

Scheme II. 1. Reaction scheme of the 2,4-diamino-6-phenyl-1,3,5-triazinium perchlorate ($C_9H_{10}N_5^+.ClO_4^-$). 22

Scheme II. 2. Reaction scheme of the 2,4,6-triamino-1,3,5-triazin-1,3-dium bisperchlorate monohydrate ($C_3H_8N_6^{2+}.2ClO_4^-.H_2O$). 23

Scheme II. 3. Scheme of ionic liquids developed formulas. 23

Scheme II. 4. Reaction scheme of DH4MPMP and H4MPMPA. 24

Scheme II. 5. Explicative scheme of the work electrode's preparation. 28

Table captions

Chapter I

Table I. 1. Theoretical values for dipole moment (μ), polarizability (α) and its anisotropy polarizability (Δα), and first hyperpolarizability (β) for the ILs. 13

Chapter III

Table III. 1. Crystal data structure and the parameters of the refinement.....39
Table III. 2. Geometric parameters (Å, °). 40
Table III. 3. Geometric properties of the hydrogen bonds (Å, °) 41
Table III. 4. FT-IR vibrational wavenumbers and their assignments. 43
Table III. 5. Crystal data structure and the parameters of the refinement.....47
Table III. 6. Geometric parameters (Å, °) characteristic of the second hybrid compound. 48
Table III. 7. Geometric properties of the hydrogen bonds (Å, °). 48
Table III. 8. FT-IR vibrational wavenumbers and their assignments. 52

Chapter IV

Table IV. 1. Common theoretical bond lengths and angles of $VBmim^+$ cation, [$VBmim^+$, PF_6^-], [$VBmim^+$, Cl^-], and [$VBmim^+$, NTF_2^-].....59
Table IV. 2: Theoretical and experimental infrared frequencies, with their [$VBmim^+$, Cl^-], [$VBmim^+$, PF_6^-], and [$VBmim^+$, NTF_2^-] assignments.....61
Table IV. 3. Computed dipolar moments, HOMO and LUMO energies as well as associated global quantum chemical descriptors (GQCDs) for [$VBmim^+$, PF_6^-], [$VBmim^+$, Cl^-], and [$VBmim^+$, NTF_2^-].....68
Table IV. 4. Thermal parameters of [$VBmim^+$, Cl^-], [$VBmim^+$, NTF_2^-] and [$VBmim^+$, PF_6^-]. ...69
Table IV. 5. Calculated components of polarizability anisotropy (Δα), polarizability (α), and the first order hyper-polarizability (β) of [$VBmim^+$, Cl^-], [$VBmim^+$, PF_6^-] and [$VBmim^+$, NTF_2^-]. ..71
Table IV. 6. Electronic transition assignments, their corresponding energies, gap energy and oscillator strength values characteristic of the [$VBmim^+$, Cl^-], [$VBmim^+$, PF_6^-] and [$VBmim^+$, NTF_2^-].....73

Chapter V

Table V. 1. Corrosion rate and inhibition efficiency of DH4MPM and H4MPMPA vs concentrations in acidic medium. 80

Table V. 2. Corrosion rate and inhibition efficiency of 2,4,6-triamino-1,3,5-triazin-1,3-dium bisperchlorate monohydrate vs concentrations in acidic medium. 80

Table V. 3. Corrosion rate and inhibition efficiency of [VBmim^{+}, Cl^{-}] vs concentrations in acidic medium. 81

Table V. 4. Surface roughness of XC48 steel in the presence and absence of DH4MPMP and H4MPMPA. 82

Table V. 5. Electrochemical parameters derived from Tafel curves. 85

Table V. 6. Electrochemical parameters derived from impedances diagrams. 86

Table V. 7. Adsorption energies (kJ.mol^{-1}) of DH4MPMP or H4MPMPA and water molecules on the Fe (110) surface. 89

Table V. 8. Fit results of the experimental EIS data. 93

List of abbreviations

2D and 3D: Two dimensions and three dimensions

AA: Ascorbic acid

A: Electron affinity

AC: Ante Christum

AFM: Atomic force microscopy

as/*s:* Asymmetric/symmetric

B3LYP: Beck's three parameter hybrid exchange functional, the Lee-Yang-Parr correlation functional

β_{tot}: First order hyper-polarizability

$C_3H_8N_6^{2+}.2Cl\ O_4^-.H_2O$: 2,4,6-triamino-1,3,5-triazin-1,3-dium bisperchlorate monohydrate

$C_9H_{10}N_5^+.ClO_4^-$: 2,4-diamino-6-phenyl-1,3,5-triazinium perchlorate

CCDC: Cambridge Crystallographic Data Centre

C_{dl}: Double layer capacitance

CE: Counter electrode

$[Cl^-]$: Chloride anions

CR: Corrosion rate

CPE/IL: Ionic liquid modified carbon paste electrodes

CPEs: Carbon paste electrodes

CV: Cyclic voltammetry

DA: Dopamine

δ: Out of plane bending vibration

DF: Density functional

DFT: Density functional theory

DH4MPMP: Diethyl [hydroxy (4-methoxyphenyl) methyl] phosphonate

DSC: Differential scanning calorimetry

DTG: Differential thermal gravimetry

E_{corr}: Corrosion potential

EIS: Electrochemical impedance spectroscopy

E_{tot}: Total energy of the system

FMOs: Frontier molecular orbitals

GQCDs: Global quantum chemical descriptors

H4MPMPA: [Hydroxy (4-methoxyphenyl) Methyl] phosphonate acid

$\hat{H}_{tot}$: Total Hamiltonian

η: Hardness

HOMO: High occupied molecular orbitals

I: Ionization potential

i_{corr}: Corrosion current

IE_{EIS}: Inhibition efficiency

IE_p: Inhibition efficiency

IE_W: Inhibition efficiency

IL: Ionic liquid

ILs: Ionic liquids

ImILs: Imidazolium-based ionic liquids

IR: Infra-red

I-V: Current-voltage curve

LUMO: Low unoccupied molecular orbitals

MD: Molecular dynamics

MDS: Molecular dynamic simulation

MOFs: Metal organic frameworks

NBO: Natural bonding orbitals

NLO: Non-linear optic

[$N(CN)_2^-$]: Dicyanamide anion

[NTF_2^-]: Bis (trifluoromethylsulfonyl) imide anion

OCP: Open circuit potential

ω: Electrophilicity index

ω: Wagging

PILs: Protic ionic liquids

[$PC_6C_6C_6C_{14}$]: Trihexyltetradecylphosphonium cation

ρ: Rocking

RE: Reference electrode

S: Softness

SCE: Saturated Calomel Electrode

SCCs: Supramolecular coordination complexes

SXRD: Single crystal X-rays diffraction

T_b: Boiling point

TD-DFT: Time dependent density functional theory

TGA: Thermal gravimetric analysis

$\hat{T}_e$: Kinetic energy

T_g: Glass transition temperature

$\hat{T}_N$: Kinetic energy operator of nuclei

T_m: Melting point

UV: Ultra-violet

$<\alpha>$: Average polarisability

$\Delta\alpha$: Polarisability anisotropy

$<\Delta W>$: Average weight loss

$\hat{V}_{e\text{-}e}$: Potential energy operator of electron-electron interaction

$\hat{V}_{e\text{-}N}$: Potential energy operator of electron-nucleus interaction

VdW: Van der Waals

VSEPR: Valence shell electron pair repulsion

[$VBmim^+$, NTF_2^-]: 1-methyl-3-(4-vinylbenzyl) imidazole-3-ium bis (trifluoromethylsulfonyl) imide

[$VBmim^+$, Cl^-]: 1-methyl-3-(4-vinylbenzyl) imidazole-3-ium chloride

[$VBmim^+$, PF_6^-]: 1-methyl-3-(4-vinylbenzyl) imidazole-3-ium hexafluorophosphate

WE: Work electrode

w/w: Weight to weight

χ: Electronegativity

Ψ_{tot}: Total wave function of the system

ΔE: Gap energy

θ: Surface coverage

ν: Stretching vibration

μ: Dipole moment

General introduction

General introduction

Ionic materials' intriguing chemical and physical properties have garnered a lot of curiosity. characteristic, which are related to the state of matter as electric conductivity, which is low in the case of the ionic solids and high in the case of the ionic liquid.

A very powerful and promising family of materials is developing: organic-inorganic hybrids. The complementarity results in a complete synergy of the desired material's properties and ultimately an end-product. In order to create new materials with enhanced or new properties, hybrid material designers aim to combine the best aspects of two distinct chemical worlds, often with complementary strengths. Those materials exhibiting a good thermal stability, mechanical and optical properties...etc [1]. Moreover, 1,3,5-triazine ring-containing organic-inorganic hybrid materials offer enhanced or unique properties that enable the creation of novel industrial applications. They are frequently utilised as a fire retardant addition for polymeric materials because of their great thermal stability. These hybrids are used for the synthesis of the supramolecular structures and high molecular architectures. They have been frequently used to build one-, two-, and three-dimensional patterns in combination with different acids because they are efficient H-atom donors and acceptors, Furthermore, their derivatives have the ability to generate hydrogen-bonded self-assemblies with particular surface structures; in supramolecular chemical science, these structures are employed as surface models.

Melamine (2,4,6-triamino-1,3,5-triazine) is the best-known, since the development of melamine-formaldehyde resins in the 1930s [2]. Benzoguanamine (2,4-diamino-6-phenyl-1,3,5-triazinium) is a white crystalline solid, it has been shown to be chemically stable and structurally stable. Melamine and Benzoguanamine are planar compounds nitrogen-rich, with the ability to form both mono- and diprotonated cations. They create hydrogen-linked self-assemblies with specific surface characteristics, which have served as models in supramolecular chemistry research [3].

The liquid state of ionic materials is represented by ionic liquids, which are formed just by ions, with an uneven structure and smaller anion concentrations. Which can be biological or inorganic. ILs characterized by low melting point (below 100 °C in general), low vapor pressure and high ionic conductivity [4]. Ionic liquids' unique physicochemical properties have led to increased application in domains such as chemistry, chemical engineering, and materials science, resulting 68,057 scientific publications from November 2010 to 2020 [5].

Imidazolium-based ionic liquids (ILs) are a popular type of ionic liquid which has an imidazolium cation (a five-membered ring with two nitrogen atoms) combined with a wide range of anions. Their unique characteristics, structural tunability, and environmental benefits make them perfect for a variety of uses.

Powdered carbon (graphite) and a binder (pasting liquid) combine to form carbon paste. In the production of different electrodes, detectors, and sensors in laboratories, it has emerged as one of the most often utilised electrode materials. [6]. Because of their many benefits, including low ohmic resistance, chemical inertness, renewability, resilience, stable response, no need for an internal solution, and suitability for a range of detection and sensing applications, carbon paste electrodes, or CPEs, have drawn interest as electrodes. Modifiers improve Kinetics of electron transport and signal strength. These are easy to incorporated into composites made of carbon paste. Ionic liquids are frequently used to replace traditional binders, either completely or partially [7].

This work have been divided into five chapter

- The first chapter is devoted to the general presentation of ionic materials including hybrid materials and ionic liquids. Definitions, properties, classification and applications are mentioned in this chapter
- The second chapter is devoted to the description of the synthesis, analysis techniques, and methods were used and a description of theoretical approaches.
- The focus of the third chapter is the experimental study of ionic hybrid organic-inorganic materials, the results obtained by the diffraction of X-rays, spectroscopic methods (UV-Vis and IR) and Thermo-gravimetric studies TGA
- The fourth chapter is devoted to the experimental study of ionic liquids which include spectroscopic methods and Thermo-gravimetric studies (TGA and DSC), as well as a theoretical study by quantum calculation (optimized molecular structure, MEP, partial charges, molecular orbitals, thermal, thermodynamic as well as nonlinear optical characteristics).
- The fifth chapter is devoted to the study of the corrosion efficiency of organic molecules (phosphoric molecules) and ionic materials (ionic organic-inorganic hybrid materials and ionic liquids), as well as the study of the electronic-transport property of the ionic liquids adopting the method of the carbon past electrode (CPE)
- We will end with a conclusion and propose perspectives.

References

[1] M. R. B. M. Rejab, M. H. B. M. Hamdan, M. Quanjin, J. P. Siregar, D. Bachtiar, and Y. Muchlis, "Historical Development of Hybrid Materials," in *Encyclopedia of Renewable and Sustainable Materials*, Elsevier, 2020, pp. 445–455. doi: 10.1016/B978-0-12-803581-8.10546-6.

[2] H. R. Allcock and F. W. Lampe, *Contemporary polymer chemistry*, 2. ed. Englewood Cliffs, NJ: Prentice Hall, 1990.

[3] R. Bourzami, H. C. AitYoucef, N. Hamdouni, and M. Sebais, "Synthesis, crystal structure, vibrational spectra and thermal properties of novel ionic organic-inorganic hybrid material," *Chemical Physics Letters*, vol. 711, pp. 220–226, Nov. 2018, doi: 10.1016/j.cplett.2018.08.002.

[4] Peter Wasserscheid and T. Welton, Eds., *Ionic liquids in synthesis*, 2. reprint. Weinheim: Wiley-VCH, 2004.

[5] G. A. O. Tiago, I. A. S. Matias, A. P. C. Ribeiro, and L. M. D. R. S. Martins, "Application of Ionic Liquids in Electrochemistry—Recent Advances," *Molecules*, vol. 25, no. 24, p. 5812, Dec. 2020, doi: 10.3390/molecules25245812.

[6] I. Švancara, K. Vytřas, K. Kalcher, A. Walcarius, and J. Wang, "Carbon Paste Electrodes in Facts, Numbers, and Notes: A Review on the Occasion of the 50-Years Jubilee of Carbon Paste in Electrochemistry and Electroanalysis," *Electroanalysis*, vol. 21, no. 1, pp. 7–28, Jan. 2009, doi: 10.1002/elan.200804340.

[7] S. G. Hernández-Vargas, C. Alberto Cevallos-Morillo, and J. C. Aguilar-Cordero, "Effect of Ionic Liquid Structure on the Electrochemical Response of Dopamine at Room Temperature Ionic Liquid-modified Carbon Paste Electrodes (IL–CPE)," *Electroanalysis*, vol. 32, no. 9, pp. 1938–1948, Sep. 2020, doi: 10.1002/elan.201900701.

Bibliography

I. Bibliography

I.1 Ionic materials

Ionic materials are compounds made up of ions linked together by ion-covalent bonds and/or electrostatic interactions. These materials are often generated when atom or collection of atoms exchange charges (electrons or H^+), generating cations that are positively charged and negatively anions moieties. The electrostatic interaction of these oppositely charged ions results in a strong and stable structure, the table salt (sodium chloride, [Na^+, Cl^-]) is a common example [1]. My PhD work concentrate on the investigation of two types of ionic materials, the first one is the ionic solid hybrid (organic–inorganic) materials, and the second is ionic liquid materials.

I.1.1 Hybrid organic-inorganic materials

I.1.1.1 Definition

Composites consisting of both organic and inorganic elements at length scales varying from a few angstroms to a few tens of nanometres are known as hybrid organic–inorganic materials [2]. In order to create new materials with enhanced or novel features, hybrid nanocomposites are designed to combine the best aspects of two distinct chemical worlds, often with complementary strengths [3]. The primary difficulty lies in creating hybrid combinations that preserve or improve upon each component's best qualities while removing or lessening its specific drawbacks. Taking on this issue offers the chance to create novel materials with synergistic behaviour that will enhance performance or yield new beneficial qualities [3]. While the organic elements add flexibility to the framework and alter the solid's optical characteristics, the inorganic components offer structural, mechanical, thermal, and stability [4]. It was discovered that the hybrid materials were used for the first time in the prehistoric painting, however, their potential use as industrial agent have seen the day by the Chinese civilization around 900 to 600 AC. Actually, the hybrid materials are used in all areas of industry as well as the fields of academic researches [5] [6]. The figure I. 1 enumerates the growth and multidisciplinary development of organic-inorganic hybrid materials.

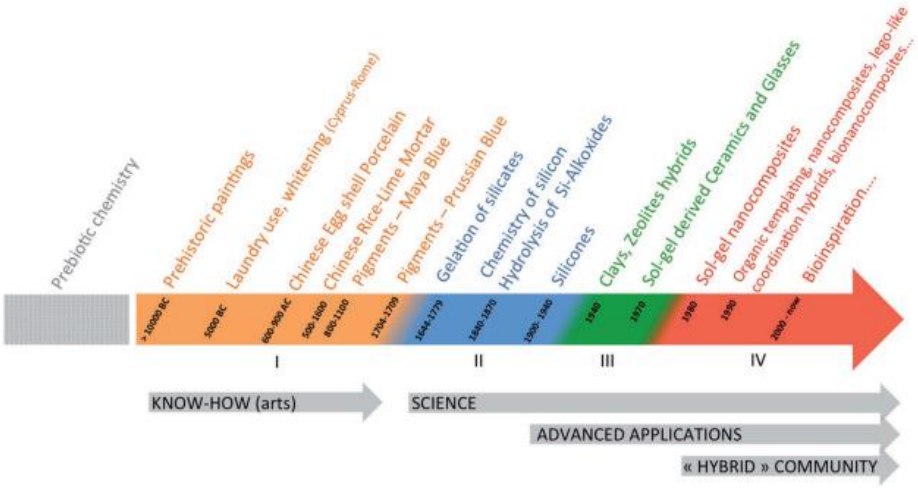

Figure I. 1. Timeline of the creation and multidisciplinary progress of hybrid materials made of organic and inorganic [5].

When organic and inorganic ions match, an ionic hybrid organic-inorganic material builds up [7], there are several examples of this materials in the literature as 2,6-diaminopyridinium perchlorate salt [8].

I.1.1.2 Classification

Based on how the organic and inorganic components interact, hybrid materials can be divided into two categories [9]

Type I: Van der Waals, weak electrostatic interactions, and hydrogen bonds, are the only physical interactions that occur between organic and inorganic materials in these kinds of hybrid materials.

Type II: The interaction between organic and inorganic material linked to gather through covalent or iono-covalent chemical bonding.

I.1.1.3 Approaches of elaboration

Actually, there are four main ways of elaboration of hybrid materials:

1. By dispersing pre-formed nano mineral components in a matrix of organic polymer or by building the organic host network around the mineral component.
2. By simultaneous growth of both organic and mineral components. The degree of homogeneity of these materials is controlled by adjusting the growth kinetics of the different components.
3. By optimizing supramolecular interactions (Van der Waals bonds, electrostatic or hydrogen) or by creating powerful chemical bonds of a covalent or iono-covalent nature between mineral and organic entities.

4. By insertion, or intercalation of organic molecules in a preformed, lamellar or porous mineral host network.

In this work, the development of hybrid materials is based on the second approaches (simultaneous growth of both organic and mineral components).

I.1.1.4 Common hybrids families

I.1.1.4.1 Hybrid porous materials

Porous materials are substances characterized by the presence of voids spaces within their structure (Figure I. 2), which allows them to absorb or contain gases, liquids, or solids. These voids can range in size from nanometres to millimetres and can be interconnected or isolated. Unlike supramolecular chemistry, hybrid porous solids are created when organic and inorganic species combine to form three-dimensional structures whose skeletons solely comprise covalently bonded organic and inorganic moieties, such as metal organic frameworks (MOFs) [10], [11].

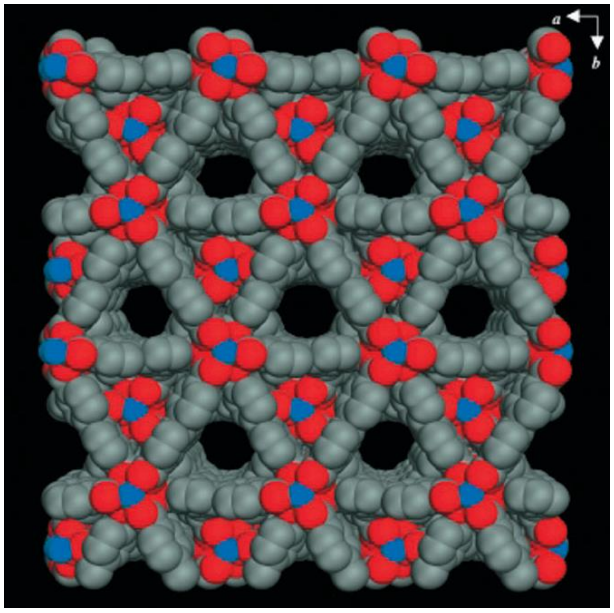

Figure I. 2. Top view (001) of the channels in the 3D Co-based organic-inorganic hybrid framework, Co (light blue) O (red), N (blue), C (gray) [12].

I.1.1.4.2 Hybrid lamellar materials

Hybrid lamellar material refers to composite structures composed of lamellar phases derived from different materials or systems (Figure I. 3). These hybrid lamellar materials might combine layers or lamellae from disparate sources, resulting in materials with unique properties or functionalities. A well-defined mesostructure of the M41S family is the MCM-50 having an unstable lamellar structure. A way to obtain a directly functionalized lamellar structure is the sol-

gel process which has been used to prepare many layered magnesium, nickel, aluminum and Mg-Al silsesquioxane hybrids [4].

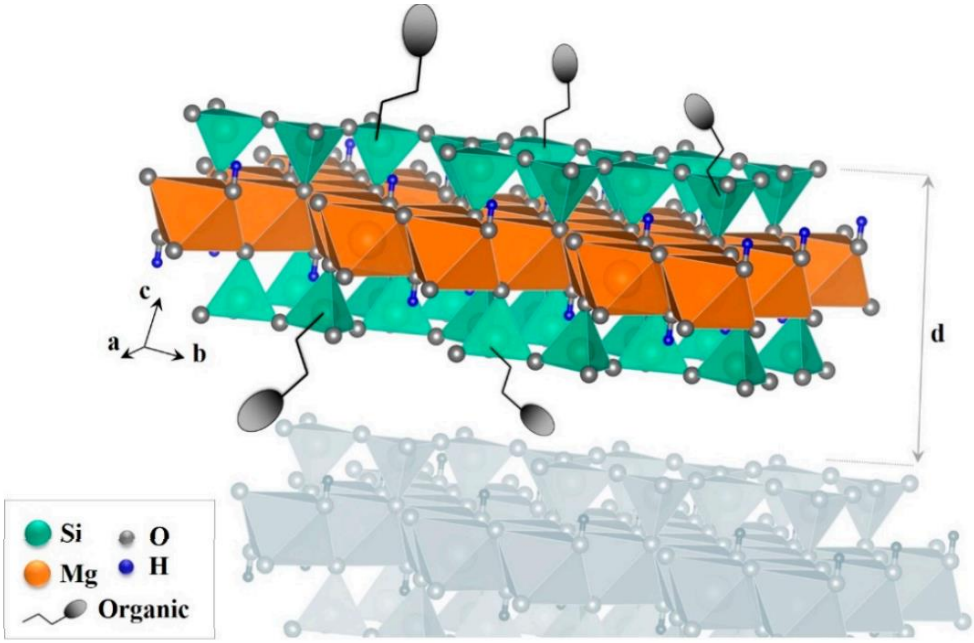

Figure I. 3. Structure of a typical organic-inorganic phyllosilicate produced via the sol-gel process: d refers to the thickness of the layer and its interlayers [13].

I.1.1.4.3 Supramolecular hybrid materials

Supramolecular hybrid materials are materials that integrate supramolecular chemistry concepts with hybrid material structures, often involving the assembly of organic and inorganic components (Figure I. 4). These hybrids are designed to exhibit emergent properties or functionalities resulting from the synergistic interactions between the supramolecular motifs and the diverse components of the hybrid system. Molecular self-assembly is the process by which molecules spontaneously group together in stable aggregates with a well-defined composition and structure when they are in equilibrium and connected by noncovalent bonds [14]. The well-defined, distinct 2D or 3D molecular entities known as supramolecular coordination complexes (SCCs) have appropriate metal centres and perform coordination-driven self-assembly with ligands that have numerous binding sites. One of the main characteristics of supramolecular complexes is undoubtedly their host-guest characteristics, which make them appealing for a variety of possible uses in catalysis, fluorescence probe design, and the creation of innovative treatments in addition to being very interesting architectures [15].

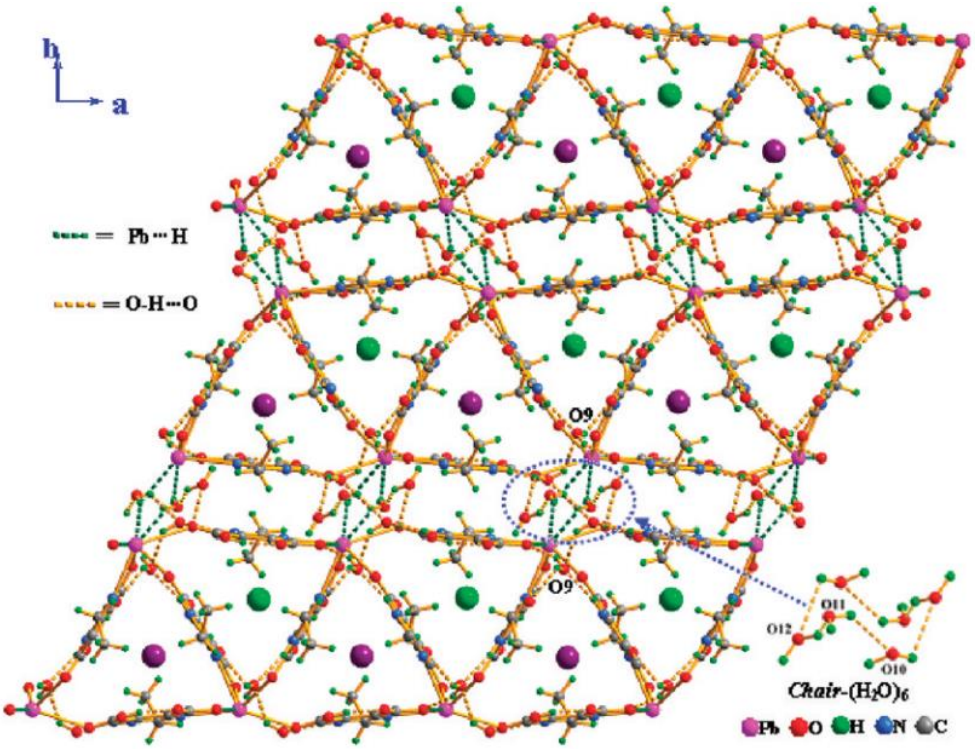

Figure I. 4. 3D supramolecular network of {[Pb(H_2IEDC)$_2$)]·3H_2O}n building by hydrogen bonding O−H···O and Pb···H interactions [16].

The hybrid materials studied and elaborated during my PhD belong to this last family (Supramolecular hybrid materials), which my research team developed and studied the properties of many supramolecular hybrid ionic materials [17] [18], and my work was the development of new ones, and study their properties as well as their efficiency as corrosion inhibitors in acidic medium [19].

I.1.2 Ionic liquids

I.1.2.1 Definition

The second type of materials studied during my PhD, are ionic liquid materials. Ionic liquid materials are liquids made up entirely or nearly entirely of ions. As a result, they have ionic conductivity. Liquids with high melting points that are commonly referred to as molten salts or fused salts are included in this definition. [20].

I.1.2.2 Elaboration

The history of ionic liquids dates back to 1914, when ethylammonium nitrate was first reported [21]. This species was created by adding concentrated nitric acid to ethylamine, then distilling the water to get the pure salt, which was liquid at room temperature. Ionic liquid synthesis involves two steps [22]. The first step consists on the formation of the desired cation by protonation

with a free acid or by quaternizing an amine or a phosphine, most often with a haloalkane. The second step consists on the exchange of the anion(s) to produce the desired product, which includes two types: direct treatment of halide salts with Lewis acids and anion metathesis. Both approaches require distinct experimental procedures, as shown in scheme I. 1.

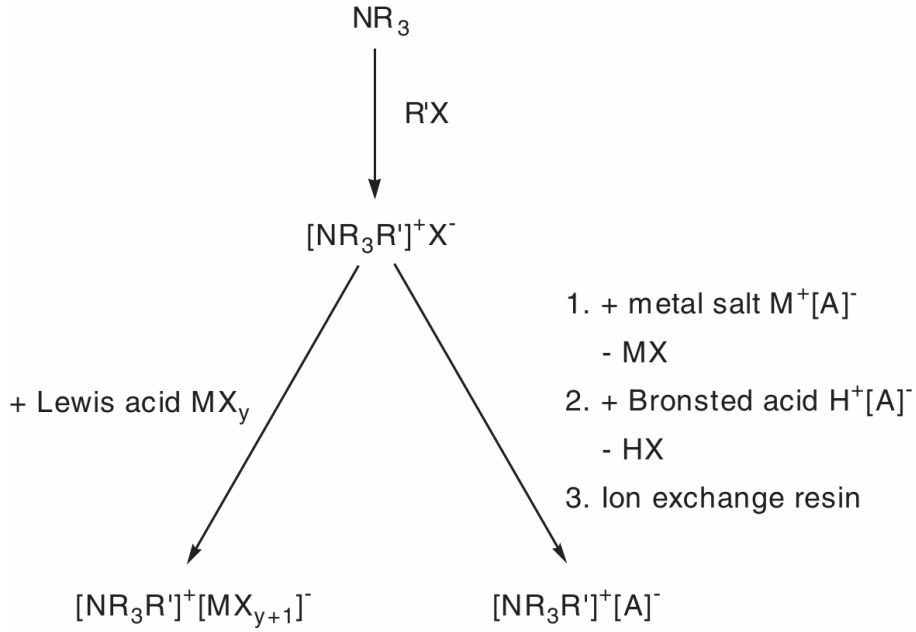

Scheme I. 1. Typical synthetic pathways for elaborating ionic liquids.

In some cases, only the first step is required, as with the formation of ethylam monium nitrate. Commercially available cations, such as halide salts, can often be obtained at a reasonable cost, making the anion exchange process all that is needed. Examples of these include symmetrical tetraalkylammonium salts and trialkylsulfonium iodide [22].

The synthesis of the ionic liquid materials was performed before my PhD, by the member of my research team in collaboration with the Laboratory of Synthesis and Catalysis, Ibn-Khaldoun University, Tiaret, Algeria, and my work focalises on the study of the molecular structure, the physical-chemical properties, and proposition of potential applications.

I.1.2.3 Classes of ILs

I.1.2.3.1 Aprotic ionic liquids

Aprotic ionic liquids are a subset of ILs that lack acidic protons. In other words, they do not readily donate protons (H^+ ions). Instead, they consist of cations and anions that do not participate in Brønsted acid-base reactions are liquids in which the cations are organic molecular ions [23].

I.1.2.3.2 Protic ionic liquids PILs

PILs are created when a proton is simply transferred between pure Brønsted acid and pure Brønsted base. The proton movement from the acid to the base, which results in the presence of proton-donor and -acceptor sites that can be utilised to create a hydrogen-bonded network, is one of the primary characteristics that set PILs apart from other ILs [24].

I.1.2.3.3 Inorganic ionic liquids

These can be created in both aprotic and protic forms by using the similar packing issues as low-melting organic cation ILs. There are several types of salts, comprising low-melting ammonium salt mixtures, salts containing inorganic molecular cations such as PBr_3Cl^+, SCl_3^+, $ClSO_2NH_3^+$, etc., with suitable weak base anions, aprotic examples such as lithium chlorate (melting point 115 °C) and its glass-forming eutectic with lithium perchlorate, and protic examples such as hydrazinium nitrate (T_m = 80 °C) [25].

I.1.2.3.4 Solvate (chelate) ionic liquids

One may suggest a fourth class; however, it would contain non-ionic things. This is the state of several ionic solvates in liquid form. Typical solvent molecules do not act as solvents in these situations because they are firmly bound to high field cations. Molten solvates only boil at temperatures close to 200 °C and have modest vapour pressures. For instance, $LiZnBr_4$ $3H_2O$ has a glass transition temperature (T_g) of 120 °C and a boiling temperature (T_b) of 190 °C. [26]

I.1.2.4 Key characteristics and techniques for understanding ILs

I.1.2.4.1 Low melting point

The main interaction forces in crystalline salts are electrostatic, and they are substantially stronger than other secondary binding forces. Electrostatic forces significantly affect the physical and thermal properties of salts. To suppression crystallization, some characteristics of their structure must be examined. Most important are the size and the shape of the ions as well as the distribution of charge on the respective ions [27].

I.1.2.4.2 Non-volatility

Ionic liquids require significant energy to evaporate because they only contain ions. The energy required to form ion pairs exceeds electrostatic forces. A pseudo-lattice stabilizes ions and reduces their lattice energy, analogous to ionic crystals. The vaporization force is significantly greater than the electrostatic force between cations and anions. Ionic liquids are thermally stable due to their exceptionally high stabilization. This explains why it is non-flammable and has no

vapor pressure at temperatures up to 400°C. Ionic liquids are flammable after decomposition; hence the term non-flammability does not accurately describe their properties. It is best to use flameretardancy or "high flame resistance. Ionic liquids have low vapor pressure and are stable across a large temperature range [27].

I.1.2.4.3 Viscosity

ILs have a high viscosity, at least ten times that of comparable solvents that of water and typically much more (similar to oil or honey). Powerful interactions between molecules, such as hydrogen bonds, van der Waals bonds, and Coulombic forces, are responsible for this. [28].

I.1.2.4.4 Ionic conductivity

The conductivity of ionic liquids is proportional to the amount of ions and their mobility. Ionic liquids have a higher concentration of ions per volume compared to regular salt solutions. The number of ionic liquids is lower than expected due to their relatively high formula weight and lack of solvent molecules. Ionic liquids have strong ionic conductivity due to the mobility of component ions and their viscosity. Several ionic liquids have conductivity more than 10^{-2} $S.cm^{-1}$ [27].

I.1.2.4.5 Computational techniques for structure elucidation

Many theoretical approaches can be used to understand the physical and chemical properties of ILs. Ever since the first computer analyses of ILs [29], the subject has greatly profited from advances in computer power and program sophistication, which are essential for studying huge systems. There are five categories of approaches for comprehending and forecasting ILs' physical characteristics [30], each with increasing complexity:

- Those that relate an IL's molecular density or volume to its physical characteristics.
- Researchers use molecular descriptors (electronic, geometric, etc.) to establish a relationship between the properties of ILs and their structure as molecules. Molecular dynamics (MD) simulations [31] investigate the structure and interactions of molecules and ions in an IL, as well as their dynamics (transport).
- Ab initio theory [32] uses electronic wave functions to study the energetics and structure of ions and clusters employing notions from quantum mechanics.
- Ab initio MD, a blend of the third and fourth processes [33].

I.1.2.5 Comparable ILs to the used ones, their properties and some examples of applications

I.1.2.5.1 Thermal properties

Several thermal properties are important for IL applications. Thermal stability is the most significant and often mentioned feature. Commonly, thermal gravimetric analysis (TGA) is used to measure the reduction in mass of a sample. K. K Thasneema *et al* [34] studied the thermal response of three ILs which have the same catoin [$PC_6C_6C_6C_{14}$] trihexyltetradecylphosphonium and three distinct anions dicyanamide [$N(CN)_2^-$], chloride [Cl^-], and bis(trifluoromethylsulfonyl) imide [NTF_2^-]. TGA plots (Figure I. 5) shows a good thermal stability for the studied ILs up to 573 K. However, the stability of IL against heat degradation depends on the chemical interactions between its ions, which vary depending on the anion-cation combinations.

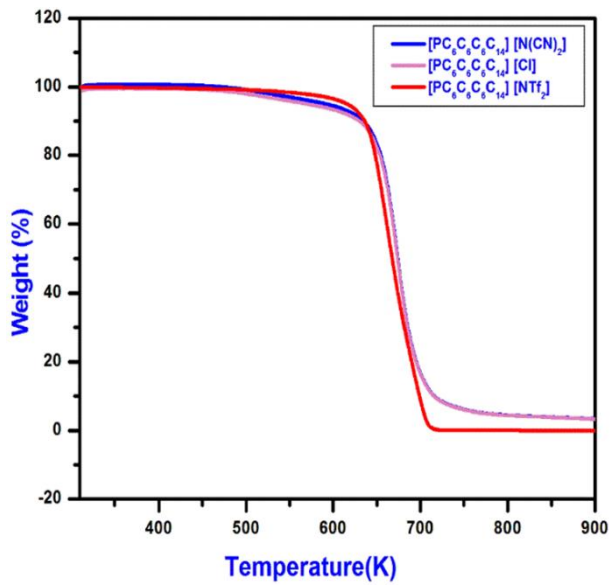

Figure I. 5. TGA response of [$PC_6C_6C_6C_{14}$][$N(CN)_2$], [$PC_6C_6C_6C_{14}$][Cl] and [$PC_6C_6C_6C_{14}$][NTF_2] ILs.

I.1.2.5.2 Nonlinear optical response (NLO)

It is known that ionic polarisation has a significant role in ionic materials, having proper frequency below the infrared. In molten ionic materials, where the ions are tiny and mobile, these ion displacements only result in conductive motions. Ionic liquids may allow for small relative ion or partial ion displacements, but they prevent longer-range motions that are necessary for conduction. Hence, "ionic polarization" may contribute to the overall polarization ionic liquids can occasionally show an additional component of ionic polarisation due to the presence of nearby ions distorting the ion's electron density, which results in a slight charge displacement. This charge shift might increase the ion's overall dipole moment, which contributes to the dielectric constant.

Therefore, at frequencies higher than those where ion conductions predominate, one may anticipate that ionic polarisation would contribute to the polarisability of ionic liquids [35]. Vinícius Castro Ferreira et al [36] investigate the nonlinear optical characteristics of ionic liquids based on imidazolium cations, both experimentally and theoretically. Theoretical simulations of nonlinear optical response using density functional theory (DFT) are described with regard to polarization (α) and first hyperpolarization (β). The Table I. 1 shows the theoretical values of the dipole moment μ, polarizability (α) and its anisotropy polarizability (Δα) and first hyperpolarizability β for ILs that are studded. Table I-1 compares the μ values of protic ILs ($BImH.HSO_4$ and $MImH.HSO_4$), indicating that increasing the alkyl chain of ($BImH.HSO_4$) causes a rise in dipole moments. The presence of a methyl group in the imidazole ring, rather than a proton, reduces the dipole moment. The $BMI.CF_3SO_3$ and $BMI.HSO_4$ have the highest first hyperpolarizability values (β). The addition of the imidazole ring's methyl group causes a shift in the molecule's symmetry, leading to an increase in β values, as this attribute depends on the dipole moment.

Table I. 1. Theoretical values for dipole moment (μ), polarizability (α) and its anisotropy polarizability (Δα), and first hyperpolarizability (β) for the ILs.

IL	μ (Debye)	Δα (x 10^{-24} esu)	α (x 10^{-24} esu)	β(x 10^{-31} esu)
$BMI.HSO_4$	12.55	6.95	21.29	28.51
$MImH.HSO_4$	12.47	14.08	14.08	18.37
$BImH.HSO_4$	12.96	7.96	19.64	16.42
$BMI.CF_3SO_3$	13.78	7.00	22.92	31.87

I.1.2.5.3 Electrode modification

Ionic liquids are utilized for electrode modification since 2000 [37]. Ionic liquids' features, including low volatility, hydrophobicity, ionic structure, high viscosity, conductivity, and biocompatibility, make them ideal for electrode modification. Ionic liquid-modified electrodes can be as simple as electrode substrates covered in ionic liquid film or droplets, or as complex as a film with a few components including ionic liquid. Two types of electrodes under investigation are electrodes that have been bulk changed (carbon paste with ionic liquid binder) and carbon nanotube-gel electrodes [37].

Electrodes made of carbon paste and ionic liquid as a binder shows an improvement in electric properties of the electrodes can be seen in voltammetric signal as a decrease in the overpotential, separation of peak to peak potential and an increase in peak current [37].

Modified carbon paste electrode with ILs can be used as detectors G. K. Jayaprakash et al [38] employed a modified carbon paste electrode with benzethonium chloride (BzTCMCPE) to detect dopamine (DA) and ascorbic acid (AA) at physical conditions (pH 7.4). The electrode demonstrated high electrocatalytic activity for redox activity of AA and DA (Figure I. 6).

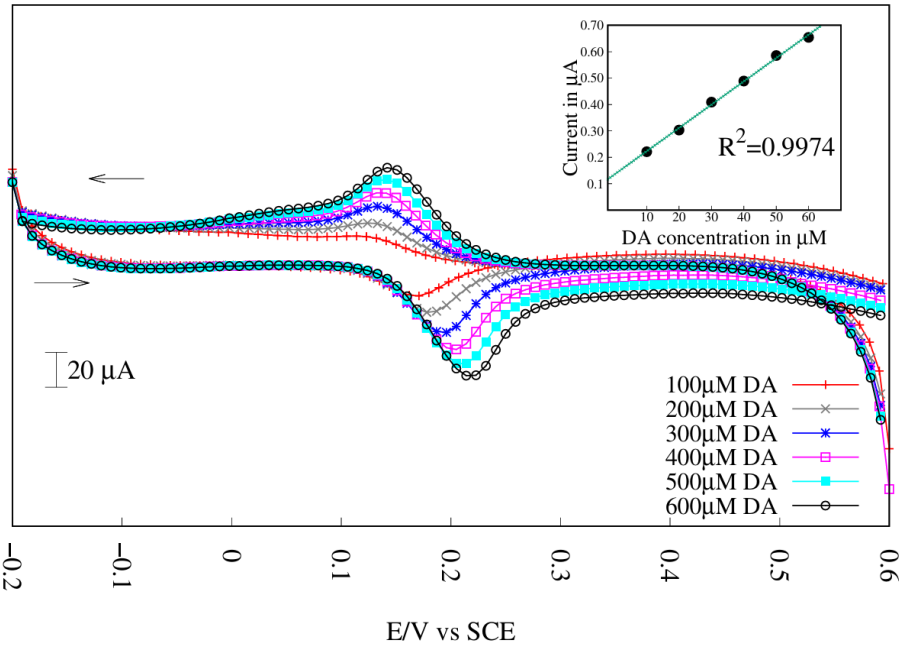

Figure I. 6. Background current subtracted CV of different concentrated dopamine at 0.1 V in phosphate buffer solution.

I.1.2.5.4 Ionic liquids as corrosion inhibitors

Corrosion is the spontaneous oxidation of metal in a corrosive (aggressive) medium. Inhibition is a protective strategy against the corrosive attack on metallic materials. Corrosion inhibitors have been intensively studied because they provide a simple way to protect metals from corrosion in an aqueous environment [39]. Corrosion inhibitors can be organic, inorganic, or hybrid (organic/inorganic) materials. S. Gurjar et al. review the use of imidazolium-based ionic liquids (ImILs) as efficient corrosion inhibitors for metals and alloys in acidic environments [40]. Experimental and theoretical investigations demonstrate that ImILs prevent corrosion by combining physical and chemical adsorption mechanisms at both anodic and cathodic sites (Figure I. 7). Initially, at the anodic site anionic species (from the acidic medium or ImILs) adsorb on the metal, forming an intermediate layer that attracts the positively charged ImILs cation then a multilayer protective barrier is formed due to Van der Waals forces and hydrophobic interactions, reducing metal dissolution. At the cathodic site imidazolium cations replace water molecules on the metal surface, reducing hydrogen evolution. The cation undergoes electron transfer, creating a

neutral molecule that donates electrons back to the metal, forming a donor-acceptor complex. This process prevents the cathodic reduction of hydrogen ions. As an example 1-Butyl -3-methyl imidazolium chloride and 1-Butyl -3- methyl imidazolium hydrogen sulfate achieved 87.50 % and 93.70 % inhibition efficiency respectively at 10 mM in 1 M HCl at 303 K [41].

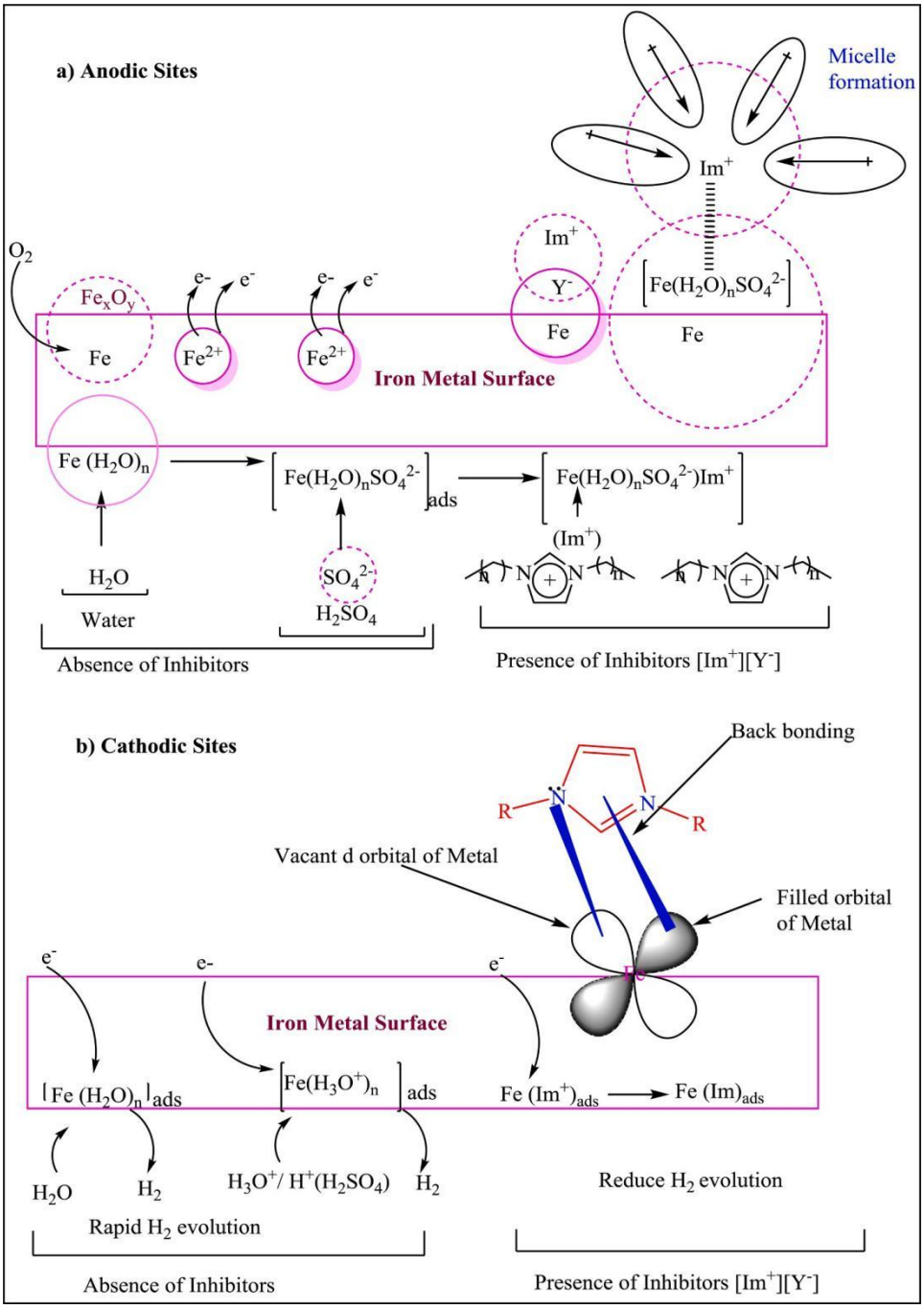

Figure I. 7. Mechanism of mild steel corrosion inhibition with ImILs in sulphuric acid at (a) Anodic and (b) Cathodic sites [40].

Three imidazolium ionic liquids are used in this work called 1-methyl-3-(4-vinylbenzyl) imidazol-3-ium chloride ([VBmim$^+$, Cl$^-$]), 1-methyl-3-(4-vinylbenzyl) imidazol-3-ium bis(trifluoromethylsulfonyl) Imide ([VBmim$^+$, NTF$_2^-$]) and 1-methyl-3-(4-vinylbenzyl) imidazol-3-ium hexafluorophosphate ([VBmim$^+$, PF$_6^-$]).

I.2 Aims of this work

The principal aim of my PhD is the elaboration of new ionic materials and study mainly of the conductivity process by and within the ionic materials, the work focus on the study of two types of ionic materials, ionic liquids (ILs) and ionic solid crystals, for achieving this aim, many steps were followed as sub-aims:

- Synthesis of new ionic hybrid (organic-inorganic) materials crystals, adopting a modified elaboration protocol developed previously by our research team.
- Affine the molecular and cell structures of the hybrid crystals using X-ray diffraction, then characterizing their electronic, optoelectronic, thermodynamic and thermal properties, using combined experimental en theoretical approaches.
- Ionic liquid materials were synthetized before my PhD, my work in this field consists on the study of the structure, vibrational, optoelectronic and thermal properties via experimental methods, and then, some DFT calculations were used to elucidate mainly the deep electronic properties, as well as to discuss and explain the experimental finding, and the reactivity/stability of the ILs.
- Test two different applications: the first is corrosion inhibition, this application was tested firstly on phosphoric organic materials and then the protocol was adapted on the ionic materials, this last sub-aim is always in progress and the second is the elaboration of modified carbon paste electrodes with ionic liquids for the study of the electronic properties.

I.3 References

[1] A. W. Wisudawati, H.-D. Barke, A. Lemma, and S. Agung, "Students' and teachers' perceptions for composition of ionic compounds," *Chemistry Teacher International*, vol. 4, no. 3, pp. 221–230, Oct. 2022, doi: 10.1515/cti-2021-0032.

[2] F. Mammeri, E. L. Bourhis, L. Rozes, and C. Sanchez, "Mechanical properties of hybrid organic–inorganic materials," *J. Mater. Chem.*, vol. 15, no. 35–36, p. 3787, 2005, doi: 10.1039/b507309j.

[3] P. Gomez-Romero, "Hybrid Organic-Inorganic Materials—In Search of Synergic Activity," *Adv. Mater.*, vol. 13, no. 3, pp. 163–174, Feb. 2001, doi: 10.1002/1521-4095(200102)13:3<163::AID-ADMA163>3.0.CO;2-U.

[4] M. Jaber, J. Miehe-Brendle, and R. L. Dred, "New lamellar Si-Al inorganic-organic hybrid material," *Journal of Materials Science*, vol. 39, no. 4, pp. 1489–1490, Feb. 2004, doi: 10.1023/B:JMSC.0000013925.73153.eb.

[5] M. Faustini, L. Nicole, E. Ruiz-Hitzky, and C. Sanchez, "History of Organic–Inorganic Hybrid Materials: Prehistory, Art, Science, and Advanced Applications," *Adv Funct Materials*, vol. 28, no. 27, p. 1704158, Jul. 2018, doi: 10.1002/adfm.201704158.

[6] J. D. Mackenzie and E. P. Bescher, "Properties and Potential Applications of Ormosils," *Journal of Sol-Gel Science and Technology*, vol. 13, no. 1/3, pp. 371–377, 1998, doi: 10.1023/A:1008600723220.

[7] J. Gebhardt and A. M. Rappe, "Mix and Match: Organic and Inorganic Ions in the Perovskite Lattice," *Advanced Materials*, vol. 31, no. 47, p. 1802697, Nov. 2019, doi: 10.1002/adma.201802697.

[8] E. Bouaziz, O. Kammoun, A. Slassi, D. Cornil, J. Lhoste, S. Auguste and M. Boujelbene, "A supramolecular non centrosymmetric 2,6-diaminopyridinium perchlorate salt: Crystal structure and optoelectronic DFT study," *Journal of Molecular Structure*, vol. 1267, p. 133561, Nov. 2022, doi: 10.1016/j.molstruc.2022.133561.

[9] P. Gómez-Romero and C. Sanchez, *Functional Hybrid Materials*. John Wiley & Sons, 2006.

[10] S. Chuhadiya, Himanshu, D. Suthar, S. L. Patel, and M. S. Dhaka, "Metal organic frameworks as hybrid porous materials for energy storage and conversion devices: A review," *Coordination Chemistry Reviews*, vol. 446, p. 214115, Nov. 2021, doi: 10.1016/j.ccr.2021.214115.

[11] G. Férey, "Hybrid porous solids: past, present, future," *Chem. Soc. Rev.*, vol. 37, no. 1, pp. 191–214, 2008, doi: 10.1039/B618320B.

[12] H.-L. Jiang and Q. Xu, "Porous metal–organic frameworks as platforms for functional applications," *Chem. Commun.*, vol. 47, no. 12, p. 3351, 2011, doi: 10.1039/c0cc05419d.

[13] M. Claverie, J. Garcia, T. Prevost, J. Brendlé, and L. Limousy, "Inorganic and Hybrid (Organic–Inorganic) Lamellar Materials for Heavy Metals and Radionuclides Capture in Energy Wastes Management—A Review," *Materials*, vol. 12, no. 9, p. 1399, Apr. 2019, doi: 10.3390/ma12091399.

[14] C. T. Seto and G. M. Whitesides, "Molecular self-assembly through hydrogen bonding: supramolecular aggregates based on the cyanuric acid-melamine lattice," *J. Am. Chem. Soc.*, vol. 115, no. 3, pp. 905–916, Feb. 1993, doi: 10.1021/ja00056a014.

[15] A. Casini, B. Woods, and M. Wenzel, "The Promise of Self-Assembled 3D Supramolecular Coordination Complexes for Biomedical Applications," *Inorg. Chem.*, vol. 56, no. 24, pp. 14715–14729, Dec. 2017, doi: 10.1021/acs.inorgchem.7b02599.

[16] Z.-G. Gu, Y.-T. Liu, X.-J. Hong, Q.-G. Zhan, Z.-P. Zheng, S.-R. Zheng, W.-S. Li, S.-J. Hu, Y.-P.Cai, "Construction of Metal-Imidazole-Based Dicarboxylate Networks with Topological Diversity: Thermal Stability, Gas Adsorption, and Fluorescent Emission Properties," *Crystal Growth & Design*, vol. 12, no. 5, pp. 2178–2186, May 2012, doi: 10.1021/cg2002095.

[17] R. Bourzami, H. C. AitYoucef, N. Hamdouni, and M. Sebais, "Synthesis, crystal structure, vibrational spectra and thermal properties of novel ionic organic-inorganic hybrid material," *Chemical Physics Letters*, vol. 711, pp. 220–226, Nov. 2018, doi: 10.1016/j.cplett.2018.08.002.

[18] H. Chenefa AitYoucef and R. Bourzami, "Synthesis, single crystal X-ray structure and vibrational spectroscopic characterization study of a new hybrid material crystal: Bis(2,4,6-trihydroxy-1,3,5-triazin-1-ium) bischloride monohydrate," *Journal of Molecular Structure*, vol. 1191, pp. 218–224, Sep. 2019, doi: 10.1016/j.molstruc.2019.03.039.

[19] H. E. Aadad, M. Galai, M. Ouakki, A. Elgendy, M. E. Touhami, and A. Chahine, "Improvement of the corrosion resistance of mild steel in sulfuric acid by new organic-inorganic hybrids of Benzimidazole-Pyrophosphate: Facile synthesis, characterization, experimental and theoretical calculations (DFT and MC)," *Surfaces and Interfaces*, vol. 24, p. 101084, Jun. 2021, doi: 10.1016/j.surfin.2021.101084.

[20] M. Freemantle, T. Welton, and R. D. Rogers, *An Introduction to Ionic Liquids*. The Royal Society of Chemistry, 2009. doi: 10.1039/9781839168604.

[21] S. K. Singh and A. W. Savoy, "Ionic liquids synthesis and applications: An overview," *Journal of Molecular Liquids*, vol. 297, p. 112038, Jan. 2020, doi: 10.1016/j.molliq.2019.112038.

[22] Peter Wasserscheid and T. Welton, Eds., *Ionic liquids in synthesis*, 2. reprint. Weinheim: Wiley-VCH, 2004.

[23] H. Ohno, Ed., *Electrochemical aspects of ionic liquids*. Hoboken, NJ: Wiley-Interscience, 2005.

[24] M. Yoshizawa, W. Xu, and C. A. Angell, "Ionic Liquids by Proton Transfer: Vapor Pressure, Conductivity, and the Relevance of $\Delta p\, K_a$ from Aqueous Solutions," *J. Am. Chem. Soc.*, vol. 125, no. 50, pp. 15411–15419, Dec. 2003, doi: 10.1021/ja035783d.

[25] C. Austen Angell, Y. Ansari, and Z. Zhao, "Ionic Liquids: Past, present and future," *Faraday Discuss.*, vol. 154, pp. 9–27, 2012, doi: 10.1039/C1FD00112D.

[26] A. Sivaraman, H. Senapati, and C. A. Angell, "Competitive Interactions and Glassy State Extension in Lithium Salt Solutions," *J. Phys. Chem. B*, vol. 103, no. 20, pp. 4159–4163, May 1999, doi: 10.1021/jp9841440.

[27] H. Ohno, "Functional Design of Ionic Liquids," *Bulletin of the Chemical Society of Japan*, vol. 79, no. 11, pp. 1665–1680, Nov. 2006, doi: 10.1246/bcsj.79.1665.

[28] D. R. MacFarlane, M. Kar, and J. M. Pringle, *Fundamentals of ionic liquids: from chemistry to applications*. Weinheim: Wiley-VCH, 2017.

[29] C. G. Hanke, S. L. Price, and R. M. Lynden-Bell, "Intermolecular potentials for simulations of liquid imidazolium salts," *Molecular Physics*, vol. 99, no. 10, pp. 801–809, May 2001, doi: 10.1080/00268970010018981.

[30] E. I. Izgorodina, “Theoretical Approaches to Ionic Liquids: From Past History to Future Directions,” in *Ionic Liquids Uncoiled*, 1st ed., N. V. Plechkova and K. R. Seddon, Eds., Wiley, 2012, pp. 181–230. doi: 10.1002/9781118434987.ch6.

[31] E. J. Maginn, “Molecular simulation of ionic liquids: current status and future opportunities,” *J. Phys.: Condens. Matter*, vol. 21, no. 37, p. 373101, Sep. 2009, doi: 10.1088/0953-8984/21/37/373101.

[32] E. I. Izgorodina, “Towards large-scale, fully ab initio calculations of ionic liquids,” *Phys. Chem. Chem. Phys.*, vol. 13, no. 10, p. 4189, 2011, doi: 10.1039/c0cp02315a.

[33] P. A. Hunt, “The simulation of imidazolium-based ionic liquids†,” *Molecular Simulation*, vol. 32, no. 1, pp. 1–10, Jan. 2006, doi: 10.1080/08927020500486627.

[34] T. K. K., M. S. Thayyil, T. Rosalin, K. K. Elyas, T. Dipin, P. K. Sahu, N. S. Krishna Kumar, V. C. Shaheer, M. Messali and T. B. Hadda, “Thermal and spectroscopic investigations on three phosphonium based ionic liquids for industrial and biological applications,” *Journal of Molecular Liquids*, vol. 307, p. 112960, Jun. 2020, doi: 10.1016/j.molliq.2020.112960.

[35] F. Wilkins, Ed., *Nonlinear optics: fundamentals, applications and technological advances*. New York: Nova Publishers, 2014.

[36] V. C. Ferreira, L. Zanchet, W. F. Monteiro, L. G. Da Trindade, M. O. De Souza, and R. R. B. Correia, “Theoretical and experimental comparative study of nonlinear properties of imidazolium cation based ionic liquids,” *Journal of Molecular Liquids*, vol. 328, p. 115391, Apr. 2021, doi: 10.1016/j.molliq.2021.115391.

[37] M. Opallo and A. Lesniewski, “A review on electrodes modified with ionic liquids,” *Journal of Electroanalytical Chemistry*, vol. 656, no. 1–2, pp. 2–16, Jun. 2011, doi: 10.1016/j.jelechem.2011.01.008.

[38] G. K. Jayaprakash, B. E. K. Swamy, B. N. Chandrashekar, and R. Flores-Moreno, “Theoretical and cyclic voltammetric studies on electrocatalysis of benzethonium chloride at carbon paste electrode for detection of dopamine in presence of ascorbic acid,” *Journal of Molecular Liquids*, vol. 240, pp. 395–401, Aug. 2017, doi: 10.1016/j.molliq.2017.05.093.

[39] E. McCafferty, *Introduction to corrosion science*. New York: Springer, 2010.

[40] S. Gurjar, S. K. Sharma, A. Sharma, and S. Ratnani, “Performance of imidazolium based ionic liquids as corrosion inhibitors in acidic medium: A review,” *Applied Surface Science Advances*, vol. 6, p. 100170, Dec. 2021, doi: 10.1016/j.apsadv.2021.100170.

[41] Q. B. Zhang and Y. X. Hua, “Corrosion inhibition of mild steel by alkylimidazolium ionic liquids in hydrochloric acid,” *Electrochimica Acta*, vol. 54, no. 6, pp. 1881–1887, Feb. 2009, doi: 10.1016/j.electacta.2008.10.025.

Experimental and methods

II. Experimental and methods

II.1 Synthesis

II.1.1.1 Ionic organic-inorganic hybrid materials

II.1.1.1.1 Synthesis of the first ionic hybrid crystal

The starting compounds are benzoguanamine and perchloric acid, which were used as supplied with a molar ratio 1:3. 10 mmol of benzoguanamine was dissolved in 30 ml of water. The mixture was maintained at 80 °C and a continuous stirring. 30 mmol of the perchloric acid was diluted in 15ml of water, and added drop wise to the first solution, and then the reaction mixture was brought to reflux. After 6 h, the solution was allowed to cool to room temperature, white solid material precipitated. The formed material was filtered and washed with ethanol several times. Finally, it was recrystallized in water adopting slow evaporation process; colourless and transparent crystals appeared. The developed empirical formula of the final compound is given in the scheme II. 1, named 2,4-diamino-6-phenyl-1,3,5-triazinium perchlorate ($C_9H_{10}N_5^+.ClO_4^-$).

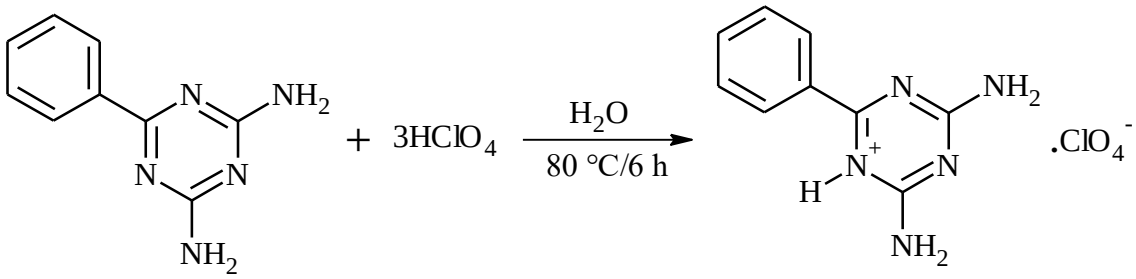

Scheme II. 1. Reaction scheme of the 2,4-diamino-6-phenyl-1,3,5-triazinium perchlorate ($C_9H_{10}N_5^+.ClO_4^-$).

II.1.1.1.2 Synthesis of the second ionic hybrid crystal

The dissolved perchloric acid was added drop wise to the melamine in hot distilled water, the mixture is brought to reflux with stirring for 6 hours. After returning to room temperature, no precipitate was observed. However, the single crystals of the synthesized hybrid material (Scheme II. 2) were harvested after a growth period of a few days. Then, they were filtered and washed by ethanol several times to obtain highly purified material, and dried in air. The developed empirical formula of the second compound named 2,4,6-triamino-1,3,5-triazin-1,3-dium bisperchlorate monohydrate ($C_3H_8N_6^{2+}.2ClO_4^-.H_2O$) is shown in the Scheme II. 2. The X-ray crystallographic data have been deposited at the “Cambridge Crystallographic Data Centre” (CCDC) with the reference number 2236683.

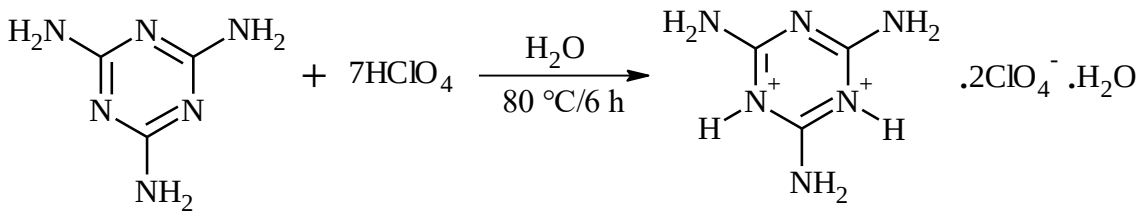

Scheme II. 2. Reaction scheme of the 2,4,6-triamino-1,3,5-triazin-1,3-dium bisperchlorate monohydrate ($C_3H_8N_6^{2+}.2ClO_4^-.H_2O$).

- ✓ The two synthesised ionic organic-inorganic hybrid materials are soluble in distilled water.

II.1.2 Ionic materials

II.1.2.1 Ionic liquids

The synthesis of [VBmim$^+$, Cl$^-$] was performed by mixing 1-methylimidazole and chloromethyl styrene with a same molar ratio in 30 ml of acetonitrile under stirring for 24 h and at 50 °C. The [VBmim$^+$, PF$_6^-$] and [VBmim$^+$, NTF$_2^-$] were synthesis by anion exchange starting from [VBmim$^+$, Cl$^-$]. The synthesis of ionic liquids were performed previously in collaboration with laboratory of Synthesis and Catalysis, Ibn-Khaldoun University, Tiaret, Algeria. It found as a results of solubility test that [VBmim$^+$, Cl$^-$] is soluble in hot distilled water, while, [VBmim$^+$, PF$_6^-$] and [VBmim$^+$, NTF$_2^-$] are soluble in acetonitrile.

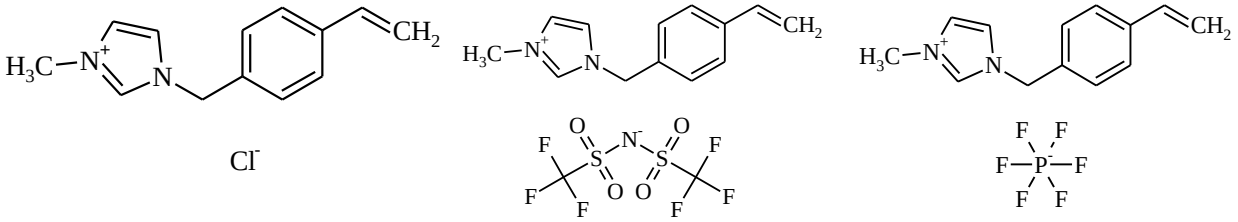

[VBmim$^+$, Cl$^-$] [VBmim$^+$, NTF$_2^-$] [VBmim$^+$, PF$_6^-$]

Scheme II. 3. Scheme of ionic liquids developed formulas.

II.1.3 Organic molecules

Two organic molecular materials were elaborated in the aim to obtain optimized experimental parameters for the corrosion inhibition experiments, which will be then used for the ionic materials. The first organic molecular material named diethyl [hydroxy (4-methoxyphenyl) methyl] phosphonate (DH4MPMP) was synthetized by chemical reaction of 4-Methoxybenzaldehyde and, triethyl phosphite in the presence of a catalyst $CoCl_2.6H_2O$ at room temperature and under a reflux and with the presence of N_2. While, the second is acid, called[Hydroxy (4-methoxyphenyl) Methyl] phosphonate acid (H4MPMPA), was produced by hydrolysis of DH4MPMP in HCl 6N at 100 °C for 24 hours as shown in scheme II. 4. The synthesis

of the organic molecules were performed previously by our research team [1]. I then reworked the synthesis protocol. The obtained DH4MPMP organic molecule is soluble in N, N-Dimethylformamide, while, the H4MPMPA is soluble in distilled water.

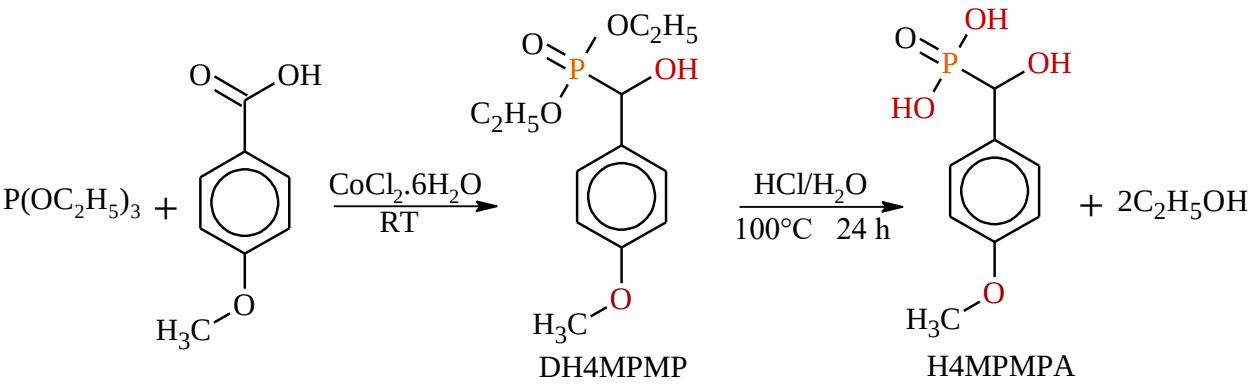

Scheme II. 4. Reaction scheme of DH4MPMP and H4MPMPA.

II.2 Analysis techniques

II.2.1 Single crystal X-ray diffraction (SXRD)

The SXRD was carried out at 150 K, utilizing Bruker D8 Venture photon diffractometer, equipped with Mo ($K\alpha_1$) anticathode and a graphite mono-chromator giving an incident wavelength of $\lambda = 0.71073$ Å. All hydrogen atoms were located in difference maps and treated as riding atoms. The refinements were performed by the method of the full-matrix least square utilizing SHELXL-2017 software [2]. All observed reflections and data reduction were used to refine of the unit cell, by the mean of the CrysAlisRed software [3]. Finally, the structures plotted in this work were performed using Mercury software [4].

II.2.2 UV–Visible and FT-IR spectroscopies

The UV-Vis spectral analysis was carried out in distilled water between 200 and 800 nm using a JASCO V-650 spectrophotometer with quartz cells of 1 cm path length. Fourier transform infrared (FT-IR) spectrum was taken on Perkin Elmer Spectrum one FT-IR spectrometer with the diffuse reflectance attachment (Miracle Attenuated Total Reflectance Attachment). Resolution was set up to 4 cm^{-1} resolution in the region 4000-400 cm^{-1}.

II.2.3 Thermo-gravimetric analysis

For the ionic organic-inorganic hybrid materials, thermal behaviours were studied from the room temperature to 1200 °C utilizing a simultaneous: Thermo-gravimetric analysis and

differential thermal analysis (TGA/DTG) techniques under nitrogen atmosphere with a heating rate of 20 °C/min, using a Perkin Elmer TGA 4000 apparatus.

For ionic liquid TGA and DSC tests were conducted utilizing TA-Q analyzers (TGA Q50 and DSC Q500) to assess degradation. TGA measurements were performed on [$VBmim^+$, Cl^-], [$VBmim^+$, NTF_2^-], and [$VBmim^+$, PF_6^-] at temperatures ranging from 25 to 1000 °C, with a scan rate of 10 °C/min under N_2. DSC used N_2 at a scan rate of 10 °C/min throughout a temperature range from -90 to 1000 °C. A heating cycle was employed to remove the water traces found in the sample's TGA data.

II.2.4 Atomic force microscopy (AFM)

The surface morphology was analyzed by AFM using an Asylum Research MFP-3D Classic AFM instrument.

II.3 Applications

II.3.1 Corrosion inhibition

II.3.1.1 Weight loss measurements

II.3.1.1.1 Organic molecules

Gravimetric analysis is a chemical way to determine the corrosion rate and inhibition efficiency. The cleaned specimens with an external surface S were immersed by triplicate, for t = 6 h, in 1M HCl solution varying the concentrations of DH4MPMP or H4MPMPA from C = 0 to 0.4 mM and for two temperatures T_1 = 298 and T_2 = 328K.

The average weight loss ΔW was calculated using the formula (II. 1) [5]:

$$< \Delta W > = \frac{\sum_1^3 (W_{before} - W_{after})}{3} \qquad \text{(II. 1)}$$

Where: W_{before} and W_{after} are the weight of the specimen before and after immersion respectively.

The corrosion rates CR, the surface coverage θ and the corresponding inhibition efficiency IE_W (%) obtained from gravimetric method were calculated using the formula (II. 2, 2II. 3 and II. 4) respectively [6] [7]:

$$CR = < \Delta W > / St \qquad \text{(II. 2)}$$

$$\theta = (CR° - CR)/CR° \qquad \text{(II. 3)}$$

$$IE_W(\%) = [((CR° - CR)/CR°] \times 100 \qquad \text{(II. 4)}$$

CR° and CR are corrosion rates in the absence and presence of inhibitors, respectively.

The carbon steel XC48 having the chemical composition: Fe (around 98-98.5 %), C(0.40-0.45%), Mn(0.50-0.80 %), Si(0.40 % max), S(≤0.035 %), P(≤0.035 %) was cut into cylindrical shape of dimensions (2 cm diameter and 0.6 high), with the external surface S=10.05 cm^2. After that, three cleaning steps were followed, abrading with Emery paper 800, 1200, 1500 and 2400, washing with distilled water and rinsed with acetone. All the chemical and electrochemical experiments were performed in HCl 1N solution prepared by dilution of analytical solution HCl 37% with distilled water. The concentration range of DH4MPMP and H4MPMPA employed was 0.1 to 0.4 mM.

II.3.1.1.2 Ionic materials

The anti-corrosion experiments were performed with the XC48 carbon steel. All specimens were polished mechanically by using the Emery papers with different sizes: 100, 600, 1500 and 2000 , then cleaned with distilled water and acetone [8].

XC48 carbon steel	XC48 carbon steel specimens	Emery paper	Polished specimens
Step 1	Step 2	Step 3	Step 4

Figure II. 1. Specimens protocol preparation.

The cleaned specimens were immersed for 6 h, in 1 M HCl solution with various concentrations of 2,4,6-triamino-1,3,5-triazin-1,3-dium bisperchlorate and [$VBmim^+$, Cl^-] ionic materials at room temperature [8].

Figure II. 2. Weight loss measurements protocol.

Corrosion rate and inhibition efficiency were obtained from weight loss measurements and calculated using the formula (II. 5, II. 6, and II. 7):

$$\Delta m = m_1 - m_2 \quad \text{(II. 5)}$$

$$CR = (\Delta m \times K)/(\rho \times S \times t) \quad \text{(II. 6)}$$

$$IE_w(\%) = [(CR^0 - CR)/CR^0] \times 100 \quad \text{(II. 7)}$$

Where m_1 and m_2 are the weight of specimens before and after immersion respectively, ρ is the alloy density (7.77 g/cm^3), K-factor (8.75×104), S is the exposed surface ($2\pi rh+2\pi r^2$), and t is the immersion time (h). The CR^0 and CR are the corrosion rates in the absence and presence of the inhibitor respectively in millimeters/year (mm/y), S is the surface area of the specimen (cm^2), and IE_w (%) is the inhibition efficiency [8].

II.3.1.2 Electrochemical method

Electrochemical measurements were carried out using a PGZ 301 volta lab 40, and the data were analyzed with Volta Master IV software, the experiments were carried out using three electrode glass cell (Saturated Calomel Electrode (SCE) as a reference, platinum plaque as Counter Electrode (CE) and XC48 steel as a Working Electrode (WE) with working surface of S=0.18 cm^2. The open circuit potential value (OCP) was stabilized up to 30 min for each electrochemical measurement with a scan rate of 0.5 mV/s.

Corrosion potential E_{corr} and current densities i_{corr} were evaluated from Tafel extrapolation, the corresponding inhibition efficiency IE_P can be deduced using the formula (II. 8) [9]:

$$IE_p(\%) = [(i^0_{corr} - i_{corr})/i^0_{corr}] \times 100 \quad \text{(II. 8)}$$

Where: i^0_{corr} and i_{corr} are the corrosion current density in the absence and presence of inhibitors, respectively.

The Electrochemical Impedance Spectroscopy (EIS) experiments were performed at the frequency range from 100 kHz to 30 mHz, with an amplitude of 10 mV using alternating current (AC) at open circuit potential. The corresponding inhibition efficiency (IE_{EIS}) of inhibitors was calculated from the charge transfer resistance values employing the formula (II. 9):

$$IE_{EIS}\ (\%) = [(R_{ct}\text{-}R^0_{ct})/R_{ct}] \times 100 \quad \text{(II. 9)}$$

Where: R^0_{ct} and R_{ct} are the resistance in the absence and presence of the inhibitor respectively.

In addition, the double layer capacitance values were attained at maximum frequency (f_{max}) and calculated using the following formula (II. 10):

$$C_{dl} = (1/2\pi f_{max}) \times (1/R_p) \quad \text{(II. 10)}$$

II.3.2 Carbon paste electrodes elaboration

II.3.2.1 Preparation of carbon paste electrodes (CPEs)

II.3.2.1.1 Chemicals

Graphite powder and paraffin oil were used for preparing carbon paste electrodes (CPE). [$VBmim^+$, Cl^-], [$VBmim^+$, PF_6^-], and [$VBmim^+$, NTF_2^-] were used to prepare the modified carbon paste electrodes (CPE/IL). Potassium ferrocyanide was used as a redox probe and potassium chloride was used as an electrolyte.

II.3.2.1.2 Electrode preparation

In order to prepare the carbon paste electrode (CPE), paraffin oil and graphite powder (75/25) (w/w) were manually mixed for at least 30 minutes until a paste-like consistency was achieved. The paste was put on a container, after this, it was stored in the fridge at 3 °C for 24 hours. Then a syringe body was filled (2 mm diameter) with the paste. An electrical connection was made via a copper handle as shown in the scheme II. 5. Finally, the surface of the electrode was polished on a glass. A mixture of IL and the previously made carbon paste with a ratio of (2.5/97.5) (w/w) was manually mixed for at least 10 minutes to create the modified carbon paste electrode [10]. Then the previous steps was repeated for each IL.

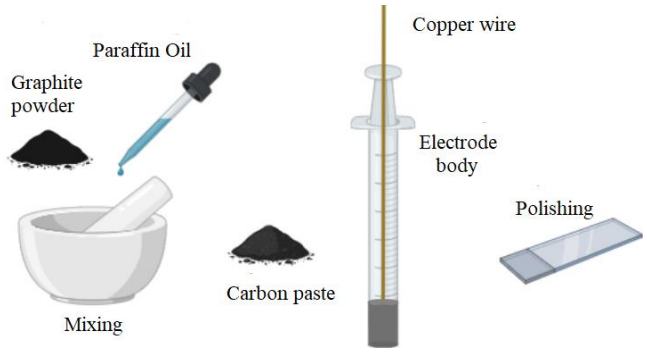

Scheme II. 5. Explicative scheme of the work electrode's preparation.

II.3.2.1.3 Apparatus

An Autolab electrochemical equipment was used to conduct the electrochemistry measurements, equipped with NOVA 1.10.1.9 software, and a standard three-electrode system were used to create the electrochemical cell (Figure II. 3). An Ag/AgCl reference electrode (RE) and a carbon electrode for the counter electrode (CE). Various kinds of carbon paste electrodes (CPE) were employed as working electrodes (WE) in this investigation: unmodified CPE acts as a baseline and modified CPE with the studied ionic liquids (CPE/IL). The cell had just one

compartment with a 20 ml internal volume. Every experiment was usually carried out at room temperature. To deaerate the liquids, pure nitrogen was utilised.

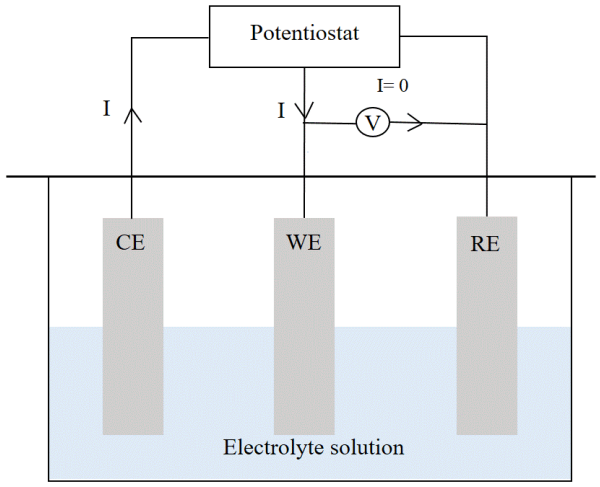

Figure II. 3. A descriptive scheme of the three-electrode cell.

II.3.2.1.4 Methods

II.3.2.1.4.1 Current-voltage characteristic (I-V)

The study was performed by linear sweep voltammetry potentiostatic in 0.1 M of KCl solution at scan rate 100 mV/s and an applied potential ranging from -1.5 to 1.5 V.

II.3.2.1.4.2 Cyclic voltammetry analysis (CV)

The study was performed by cyclic voltammetry in 0.1 M of $Fe(CN)_6^{3-/4-}$ and 0.1 M of KCl solution at a scan rate of 100 mV/s and an applied potential ranging from -0.6 to 0.8 V.

II.3.2.1.4.3 Electrochemical impedance spectroscopy (EIS)

The study was performed in 0.1 M of $Fe(CN)_6^{3-/4-}$ and 0.1 M of KCl solution. The amplitude of the imposed perturbation was 10 mV, and frequencies ranging from 10^5 to 10^{-2} Hz. The measured current values are given for an area of 1 cm^2.

II.4 Quantum calculation methods

The physical and chemical properties of a complex system: atoms, molecules, and solids (system with N electrons) depend on the behavior of its electronic structure. Quantum calculations is the ideal method for this study. In principle, this can be obtained from the time-independent Schrödinger equation. Which is written as follows:

$$\hat{H}_{tot}\Psi_{tot} = E_{tot}\Psi_{tot} \qquad \text{(II. 11)}$$

E_{tot} representing the total energy of the system and Ψ_{tot} is the total wave function of the system, which depends on the coordinates of all the particles constituting the system.

$\hat{H}_{tot}$ is the total Hamiltonian operator of the system.

The total Hamiltonian $\hat{H}_{tot}$ summarizes all kinetic and electrostatic interactions between all particles that form the system. $\hat{H}_{tot}$ therefore states:

$$\hat{H}_{tot} = \hat{T}_e + \hat{T}_N + \hat{V}_{e-e} + \hat{V}_{e-N} + \hat{V}_{N-N} \qquad \text{(II. 12)}$$

$\hat{T}_e$ represents the kinetic energy operator of electrons, $\hat{T}_N$ is the kinetic energy operator of nuclei, $\hat{V}_{e\text{-}e}$ is the potential energy operator of electron-electron interaction, $\hat{V}_{e\text{-}N}$ is the potential energy operator of electron-nucleus interaction and $\hat{V}_{N\text{-}N}$ is the potential energy operator of nucleus-nucleus interaction. The detailed expression of the Hamiltonian operator is given by:

$$\hat{H}_{tot} = \left\{\sum_{i=1}^{N_e} \frac{-\hbar^2}{2m}\nabla_i^2 + \sum_{\alpha=1}^{N^n} \frac{-\hbar^2}{2M_\alpha}\nabla_\alpha^2 + \frac{1}{2}\sum\sum_{i,i\neq j} \frac{Ke^2}{|\vec{r_i}-\vec{r_j}|} + \frac{1}{2}\sum\sum_{\alpha\neq\beta} \frac{Z_\alpha Z_\beta Ke^2}{|\vec{R_\alpha}-\vec{R_\beta}|} - \sum_{i=1}^{N_e}\sum_{\alpha=1}^{N_n} \frac{Z_\alpha ke^2}{|\vec{r_i}-\vec{R_\alpha}|}\right\} \qquad \text{(II. 13)}$$

Where m and M_α are the masses of electrons and nuclei respectively. Z_α and Z_β are the atomic numbers of the nuclei α and β, K is a constant, $\vec{r_i}$ represents the vector position of the electron (i), $\vec{R_\alpha}$ represents the vector of the position of the nucleus (α).

Or the Schrödinger equation is written:

$$\left\{\sum_{i=1}^{N_e} \frac{-\hbar^2}{2m}\nabla_i^2 + \sum_{\alpha=1}^{N^n} \frac{-\hbar^2}{2M_\alpha}\nabla_\alpha^2 + \frac{1}{2}\sum\sum_{i,i\neq j} \frac{Ke^2}{|\vec{r_i}-\vec{r_j}|} + \frac{1}{2}\sum\sum_{\alpha\neq\beta} \frac{Z_\alpha Z_\beta Ke^2}{|\vec{R_\alpha}-\vec{R_\beta}|} - \sum_{i=1}^{N_e}\sum_{\alpha=1}^{N_n} \frac{Z_\alpha ke^2}{|\vec{r_i}-\vec{R_\alpha}|}\right\}\Psi_{tot} = E_{tot}\Psi_{tot} \qquad \text{(II. 14)}$$

For example 1 cm^3 of a solid near 10^{22} atoms, implies 3(Z+1) Nα variables can be found, then it is more than obvious that one can not get a solution of this equation because it is a problem with N body which is solved only by using a certain number of approximations. These approximations include: the Born-Oppenheimer approximation (adiabatic approximation), the Hartree approximation, the Hartree-Fock approximation and density functional theory (DFT).

II.4.1 Born-Oppenheimer approximation

This approximation is based on the idea that nuclei move much more slowly than electrons because they are much heavier. Because of this, it is proposed that the electrons quickly modify their locations as the nuclei do. As a result, the nuclei are treated as fixed, with their kinetic energy neglected and their potential energy (nucleus–nucleus repulsion) considered constant during the electronic motion [11].

$$\Psi_{\text{tot}}=\Psi_{electr}(\boldsymbol{r},\boldsymbol{R})\Psi_{nuclei}(\boldsymbol{R}) \qquad \text{(II.15)}$$

Thus, the Hamiltonian operator is written as:

$$\widehat{\mathrm{H}}_{\text{tot}} = \widehat{\mathrm{T}}_{\mathrm{e}} + \widehat{\mathrm{V}}_{\mathrm{e-e}} + \widehat{\mathrm{V}}_{\text{ext}} \qquad \text{(II.16)}$$

Where, $\widehat{\mathrm{V}}_{\text{ext}}$ represents the external potential.

It is still impossible to solve the Schrödinger equation (II.11) for complex systems, even when the nuclei are fixed in their positions. Therefore, it is necessary to employ additional approximations.

II.4.2 Hartree approximation

This approximation is based on the assumption that the electrons in a system do not interact directly, which implies that their motions are considered uncorrelated. Thus the total electronic wavefunction $\Psi_{electrons}$ is approximated as a simple product of N single-electron wavefunctions [12].

$$\Psi_{electrons}(\mathbf{x}_1, \mathbf{x}_2, \ldots, \mathbf{x}_\mathrm{N}) = \Psi_1(\mathbf{x}_1)\, \Psi_2(\mathbf{x}_2)\ldots\, \Psi_N(\mathbf{x}_\mathrm{N}) \qquad \text{(II.17)}$$

A more reasonable wave function must be antisymmetric when making an exchange of two electrons. This latter consequence being more serious, the approximation of «Hartree- Fock» takes spin into account for solving the Schrödinger equation.

II.4.3 Hartree –Fock approximation

The electronic system in the Hartree approximation is not completely described. In 1930, Fock showed that the Hartree wave function (II.17) violates the exclusion principle of Pauli because it is not antisymmetric with respect to the exchange of two electrons. It has replaced the wave function $\Psi_{electrons}$ with a Slater determinant [12].

$$\Psi_{\mathrm{HF}}(\mathbf{x}_1, \mathbf{x}_2, \ldots, \mathbf{x}_\mathrm{N}) = \frac{1}{\sqrt{N!}}\begin{vmatrix} \phi_1(\mathbf{x}_1) & \phi_1(\mathbf{x}_2) & .. & \phi_1(\mathbf{x}_N) \\ \phi_2(\mathbf{x}_1) & \phi_2(\mathbf{x}_2) & .. & \phi_2(\mathbf{x}_N) \\ \phi_N(\mathbf{x}_1) & \phi_N(\mathbf{x}_2) & .. & \phi_N(\mathbf{x}_N) \end{vmatrix} \qquad \text{(II.18)}$$

Where, $\phi_i(\mathbf{x}_i) = \phi(\mathbf{r}_s) = \begin{pmatrix} \phi_\uparrow(\mathbf{r}) \\ \phi_\downarrow(\mathbf{r}) \end{pmatrix}$, $\phi_\uparrow(\mathbf{r})$ spin up and $\phi_\downarrow(\mathbf{r})$ spin down.

Therefore, this approximation allows to approach the many-body problem as a single-body problem, in which each electron is exposed to an effective potential that is partly generated by the other electrons. This method is not particularly exact, considering its complex nature. Indeed, the ground state corresponds to a global minimum over a set of functions much larger than that covered by a Slater determinant. We show nevertheless that we gradually approach the ground state by

writing Ψ as a sum of Slater determinants. This would make the calculation very heavy from a numerical point of view. That is why the density functional method is often used because it considerably and surprisingly simplifies calculations.

II.4.4 Density functional theory (DFT)

The fundamental idea of DFT is that the exact properties of the ground state of a system formed by nuclei and electrons are functionals (function of a function) of the electron density ρ(r), which is a function of 3 spatial coordinate (x, y, z) [13].

II.4.4.1 Hohenberg–Kohn theorems

In 1964, Hohenberg and Walter Kohn establish the theoretical foundation of DFT, which allows the properties of a many-electron system to be determined from the electron density instead of the complex many-body wavefunction [14]. There are two key theorems:

Theorem 1: The external potential (and thus the total energy and all ground state properties of a many-electron system) are completely determined by its ground state electron density.

Theorem 2: There exists a universal energy functional of the electron density E[ρ], and the true ground-state density ρ_0 minimizes this functional.

$$E[\rho_0] = min E[\rho] \qquad \text{(II. 19)}$$

The formulation of Hohenberg and Kohen theorems requires that the external potential is a unique functional of the ground state electron density, and hence all ground state properties. The total energy is written as:

$$E[\rho(\boldsymbol{r})] = F_{HK}[\rho(\boldsymbol{r})] + \int V_{ext}(\boldsymbol{r})\rho(\boldsymbol{r})d\boldsymbol{r} \qquad \text{(II.20)}$$

$F_{HK}[\rho(\mathbf{r})]$ is the universal Hohenberg-Kohn functional, existing for any type of system and expressed by:

$$F_{HK}[\rho(\boldsymbol{r})] = T[\rho(\boldsymbol{r})] + V[\rho(\boldsymbol{r})] \qquad \text{(II.21)}$$

$T[\rho(\mathbf{r})]$ is the total kinetic energy and $V[\rho(\mathbf{r})]$ is the electron-electron interaction energy.

However, it is remains impossible to determine the ground state of energy of a system because we don't know the exact term of $F_{HK}[\rho(\mathbf{r})]$.

II.4.4.2 Kohn-Sham approach

Hohenburg and Kohn's study paved the way for Kohn and Sham's groundbreaking discovery that N interacting electrons in an effective potential can be mapped to N non-interacting electrons. The Kohn and Sham (KS) equation is written as:

$$[-\frac{1}{2}\nabla^2 + V_{ef}(\boldsymbol{r})]\varphi(\boldsymbol{r}) = \varepsilon_i\varphi_i(\boldsymbol{r}) \qquad \text{(II.22)}$$

$$V_{ef}(\boldsymbol{r}) = V_{ext} + V_H + V_{xc}(\boldsymbol{r}) \qquad \text{(II.23)}$$

V_{ext} is the sum of nuclear potentials centred at the atomic positions, V_H is the Hartree potential due to electron density ρ(**r**') given by the expression: E

$$V_H = \frac{\partial E_H[\rho(\mathbf{r})]}{\partial \rho(\mathbf{r})} \qquad \text{(II.24)}$$

V_{xc} is the exchange correlation potential defined by equation (II.25) :

$$V_{xc} = \frac{\partial E_{xc}}{\partial \rho(\mathbf{r})} \qquad \text{(II.25)}$$

These discoveries led to the development of exchange and correlation functions, which can connect energy with electron density [13].

II.4.4.3 Exchange-correlation functional

Currently, no universal density functional (DF) exists to adequately characterise electron density in any algorithm [15] [16]. DFs can be classified into six principle types: LDA, GGA, meta-GGA, hybrid, double-hybrid, and range-separated.

II.4.4.3.1 Local density approximation (LDA)

Functional of only electron density ρ, based on the known exchange-correlation energy of the uniform electron gas. The LDA assumes that the charge density varies slowly on an atomic scale (that is, each region of a molecule actually looks like a uniform electron gas) [12].

II.4.4.3.2 Generalized gradient approximation (LDA)

Take into account the inhomogeneity of the electron gas, which naturally occurs, in any molecular system. Functional correcting LDA functional with the density gradient (first-derivative) [12].

II.4.4.3.3 Hybrid functional

Incorporate a portion of exact exchange from Hartree-Fock theory along with exchange and correlation contribution from other functional. Hybrid functional is adept at calculating

molecule structures, energies, and properties. There are numerous hybrid functional in use nowadays [12]. We choose the Beck's three parameter hybrid exchange functional, the Lee-Yang-Parr correlation functional (B3LYP) in our work.

II.5 Gaussian

Ab-initio calculations based on DFT were performed using Gaussian software package, its name is derived from the use of Gaussian functions as basis set in the describe of atomic orbitals. The theoretical calculations in this work aims to optimize molecular structure, and then investigate the electronic, vibrational, thermal and thermodynamic, and nonlinear optical properties. For the UV-Visible spectra, the time dependent density functional theory (TD-DFT) was used. All calculations were performed using (B3LYP) density functional and 6-311G++ (d, p) basis set [17].

II.5.1 Molecular Dynamic Simulation

Molecular dynamic simulations (MDS) were carried out employing adsorption locator software in Materials Studio 17.0 package, based on Monte Carlo theory. The simulation of adsorption configurations of the synthetized organic phosphonates and water molecules previously optimized by DFT, was performed on the Fe (110) surface, utilising a simulation box of (17.20×22.93×22.93 $Å^3$), considering NVT ensemble, with a time step of 0.1fs and simulation period of 50 ps. These parameters are well adapted to adsorb small molecular structures [25]. The universal force field was chosen considering bond stretching, angle bending, and torsions and inversions. The van der Waals interactions are described in the universal force field by the Lennard-Jones potential. While, the electrostatic interactions are described by atomic monopoles and a screened (distance-dependent) Coulombic term. For the atomic charges, They were chosen to be the same as the charges of the input atoms [18]. The Ewald and group summation was used for simulating the electrostatic interactions with a cut-off distance of 15.5 Å, and the atom based summation method was used for simulating the van der Waals terms with a cut-off distance of 15.5 .Å.

II.6 References

[1] L. Ouksel, R. Bourzami, N. Hamdouni, and A. Boudjada, "Synthesis, supramolecular structure, spectral properties and correlation between nonlinear optic, thermochemistry and thermal behavior of an α-Hydroxyphosphonate acid ester, dual experimental and DFT approaches," *Journal of Molecular Structure*, vol. 1229, p. 129792, Apr. 2021, doi: 10.1016/j.molstruc.2020.129792.

[2] A. V. Nemtarev, V. F. Mironov, R. R. Fayzullin, I. A. Litvinov, and R. Z. Musin, "Reactions of Arylenedioxytrihalophosphoranes with Acetylenes: XV.1 Reaction of 2,2,2-Tribromo-4,6-di-tert-butylbenzo-1,3,2λ5-dioxaphospholedioxaphosphole with Pent-1-yne," *Russ J Gen Chem*, vol. 88, no. 11, pp. 2290–2295, Nov. 2018, doi: 10.1134/S1070363218110075.

[3] "Chrysalis," Chrysalis. Accessed: Dec. 30, 2024. [Online]. Available: https://www.chrysalis.co/cart

[4] C. F. Macrae *et al.*, "*Mercury CSD 2.0* – new features for the visualization and investigation of crystal structures," *J Appl Crystallogr*, vol. 41, no. 2, pp. 466–470, Apr. 2008, doi: 10.1107/S0021889807067908.

[5] H. Amar *et al.*, "Synergistic corrosion inhibition study of Armco iron in sodium chloride by piperidin-1-yl-phosphonic acid–Zn2+ system," *Corrosion Science*, vol. 50, no. 1, pp. 124–130, Jan. 2008, doi: 10.1016/j.corsci.2007.06.010.

[6] Y. Gonzalez, M. C. Lafont, N. Pebere, and F. Moran, "A synergistic effect between zinc salt and phosphonic acid for corrosion inhibition of a carbon steel," *J Appl Electrochem*, vol. 26, no. 12, Dec. 1996, doi: 10.1007/BF00249928.

[7] J. L. Fang, Y. Li, X. R. Ye, Z. W. Wang, and Q. Liu, "Passive Films and Corrosion Protection Due to Phosphonic Acid Inhibitors," *CORROSION*, vol. 49, no. 4, pp. 266–271, Apr. 1993, doi: 10.5006/1.3316048.

[8] S. Abbout *et al.*, "Anticorrosion propriety of new resin epoxy derived from phosphorus as inhibitor of steel corrosion in 0.5 M H2SO4," *Journal of Molecular Structure*, vol. 1294, p. 136491, Dec. 2023, doi: 10.1016/j.molstruc.2023.136491.

[9] J. Telegdi *et al.*, "Influence of cations on the corrosion inhibition efficiency of aminophosphonic acid," *Electrochimica Acta*, vol. 46, no. 24–25, pp. 3791–3799, Aug. 2001, doi: 10.1016/S0013-4686(01)00666-1.

[10] N. Maleki, A. Safavi, and F. Tajabadi, “Investigation of the Role of Ionic Liquids in Imparting Electrocatalytic Behavior to Carbon Paste Electrode,” *Electroanalysis*, vol. 19, no. 21, pp. 2247–2250, Nov. 2007, doi: 10.1002/elan.200703952.

[11] D. C. Thompson and J. I. Rodríguez, “An introduction to quantum chemistry,” in *Advances in Quantum Chemical Topology Beyond QTAIM*, Elsevier, 2023, pp. 21–36. doi: 10.1016/B978-0-323-90891-7.00012-8.

[12] W. Koch and M. C. Holthausen, *A chemist’s guide to density functional theory*, Second edition. Weinheim: Wiley-VCH, 2015.

[13] T. Tsuneda, *Density functional theory in quantum chemistry*. Tokyo ; New York: Springer, 2014.

[14] K. Y. Park, “Semiconductor Interfaces and Solid Solutions for Enhanced Photocatalysis,” UNSW Sydney, 2020. doi: 10.26190/UNSWORKS/22182.

[15] W. Kohn, A. D. Becke, and R. G. Parr, “Density Functional Theory of Electronic Structure,” *J. Phys. Chem.*, vol. 100, no. 31, pp. 12974–12980, Jan. 1996, doi: 10.1021/jp960669l.

[16] R. G. Parr and W. Yang, *Density-functional theory of atoms and molecules*. in The international series of monographs on chemistry, no. 16. New York Oxford: Oxford university press Clarendon press, 1989.

[17] C. Lee, W. Yang, and R. G. Parr, “Development of the Colle-Salvetti correlation-energy formula into a functional of the electron density,” *Phys. Rev. B*, vol. 37, no. 2, pp. 785–789, Jan. 1988, doi: 10.1103/PhysRevB.37.785.

[18] R. Kiche, R. Bourzami, L. Ouksel, M. Belhocine, L. Boudjema, and F. Dergal, “A comprehensive exploration of structural, vibrational, optical, thermal and corrosion inhibition properties of trihexyl(tetradecyl)phosphonium dicyanamide ionic liquid: Experimental and theoretical methods,” *Journal of Molecular Liquids*, vol. 417, p. 126659, Jan. 2025, doi: 10.1016/j.molliq.2024.126659.

Structural, spectroscopy and thermal properties of ionic organic-inorganic crystal materials

III. Structural, spectroscopy and thermal properties of ionic organic-inorganic crystal materials

III.1 Introduction

The combination of organic compounds, more particularly azotic compounds with mineral acids give rise to new hybrid ionic crystals [1]. During our investigations and in continuation of the research work of our team on the hybrid ionic materials [2][3], we conclude that it is possible to isolate ionic compounds starting from the perchloric acid and different amines (melamine and benzoguanamine), giving two new hybrid ionic compounds.

III.2 First material

III.2.1 SXRD study

The single crystal X-ray analysis of $C_9H_{10}N_5^+.ClO_4^-$ indicates that the asymmetric unit is formed by one ClO_4^- anion, and one $C_9H_{10}N_5^+$ cation, as depicted in the figure III. 1(a). The table III. 1 summarizes crystal data and the parameters of the refinement, while the table III. 2 collects the some geometric parameters (bond lengths, angle and torsion measurements) characteristic of the studied material, any extraordinary value was found, and they are all in general order [4][5]. In addition, the material crystallizes in a monoclinic system (Figure III. 1(b)), characterized by the cell parameters a = 13.7975 (6), b = 13.7975 (6), c = 16.6471 (9) Å, β = 91.869 (2) ° and $P2_1/c$ symmetry group. The unit cell presents twenty-seven inversions, six screw axis along (Ob) and two perpendicular c-glide planes as illustrated in the figures III. 1(c to e) respectively. Furthermore, the XRD analysis reveals that weak interactions, particularly hydrogen bonds, maintain the crystal structure, twelve extra-molecular hydrogen bonds per one unit cell were predicted, considering 3.0 Å as maximum donor-acceptor distance, creating a type I hybrid material. The table III. 3 lists the geometrical parameters of the hydrogen bonds (distances and angle measurements).

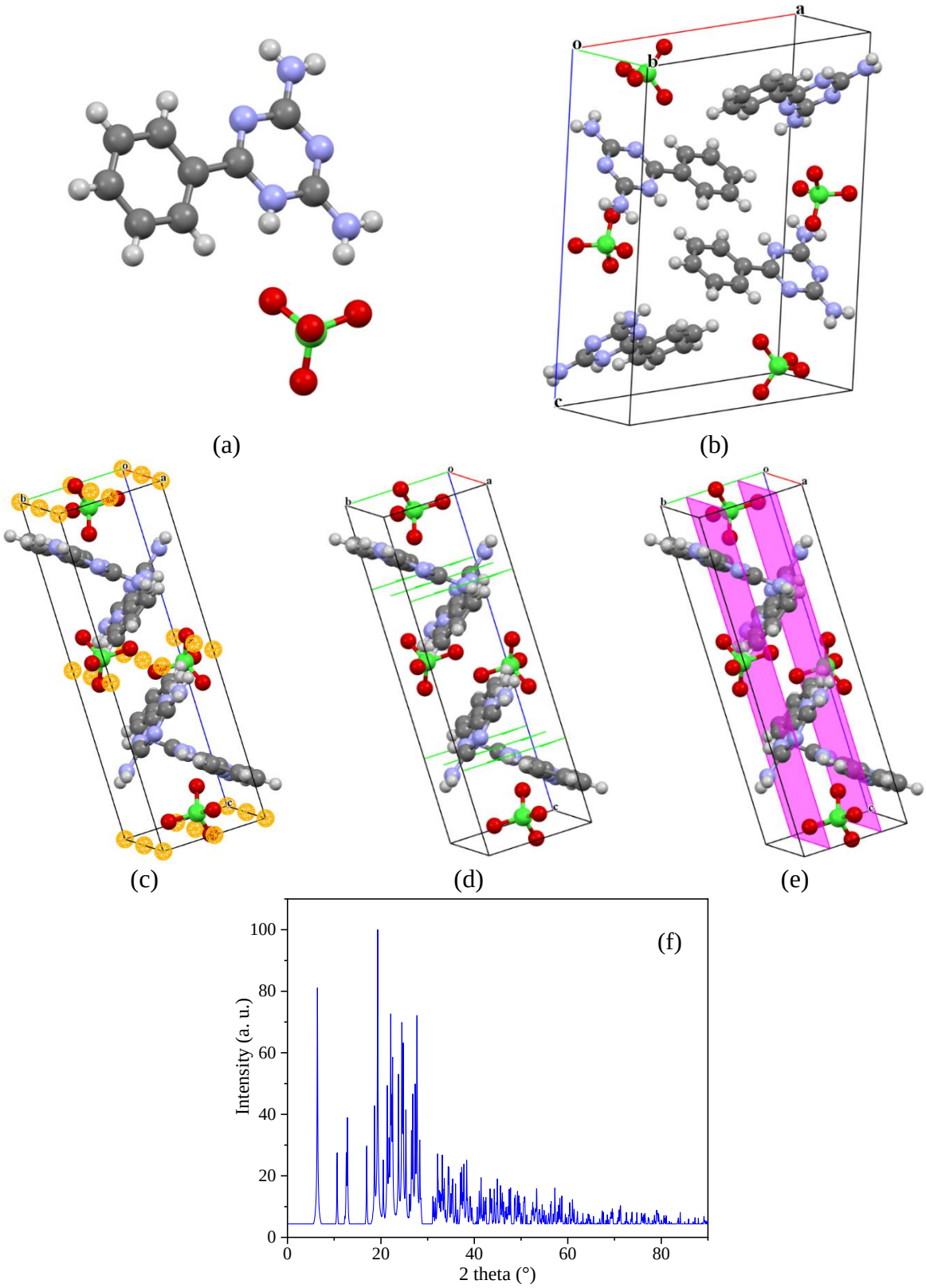

Figure III. 1. (a) Asymmetric unit, (b) unit cell. Unit cell provided by (c) inversion centers, (d) screw axes, and (e) glide planes for the 2,4-diamino-6-phenyl-1,3,5-triazinium perchlorate, (f) powder XRD pattern.

Table III. 1. Crystal data structure and the parameters of the refinement.

Empirical formula	$C_9H_{10}ClN_5O_4$
Molecular weight (g/mol)	244.61
Crystal system	Monoclinic
Crystal color/habit	Colourless/Prism
Space group	$P2_1/c$
a (Å)	13.7975 (6)
b (Å)	5.0711 (2)
c (Å)	16.6471 (9)
β (°)	91.869 (2)
V (Å^3)	1164.15 (9)
Z	4
Crystal size (mm^3)	0.60*0.40*0.35
D_{calc} (Mg/m^3)	1.641
$\lambda_{MoK\alpha 1}$ (Å)	0.7107
T (K)	150
μ (mm^{-1})	0.35
θ Range (°)	2.5→ 27.3
F(000)	592
$\Delta\rho_{min}$ (eÅ^{-3})	-0.42
$\Delta\rho_{max}$ (eÅ^{-3})	0.36
H	-17 → 17
K	-6 → +6
L	-21→ 21
Independent reflections	2681
Measured reflections	9047
reflections with I>2σ(I)	2094
No. of parameters	187
R_{int}	0.027
$wR(F^2)$	0.127
R [$F^2>2\sigma(F2)$]	0.042
S	1.03

Table III. 2. Geometric parameters (Å, °).

Distances			
C1—N4	1.309 (3)	C4—C9	1.385 (3)
C1—N2	1.327 (3)	C6—C5	1.380 (3)
C1—N1	1.365 (2)	C6—C7	1.362 (4)
C2—N5	1.313 (3)	C8—C7	1.369 (4)
C2—N2	1.347 (3)	C9—C8	1.385 (3)
C2—N3	1.366 (2)	Cl1—O1	1.4309 (17)
C3—N3	1.303 (2)	Cl1—O2	1.4154 (18)
C3—N1	1.356 (2)	Cl1—O4	1.4261 (15)
C4—C3	1.479 (3)	Cl1—O3	1.4331 (18)
C4—C5	1.385 (3)		
Angles			
N4—C1—N2	120.73 (18)	N3—C3—C4	119.59 (17)
N1—C1—N4	118.49 (19)	N1—C3—C4	119.22 (17)
N1—C1—N2	120.76 (17)	C5—C4—C9	118.7 (2)
N5—C2—N2	118.35 (17)	C8—C9—C4	120.0 (2)
N5—C2—N3	116.42 (18)	C3—N1—C1	120.19 (17)
N2—C2—N3	125.23 (17)	C1—N2—C2	115.93 (15)
N3—C3—N1	121.19 (17)	C2—N3—C3	116.54 (16)
C5—C4—C3	118.11 (19)	O2—Cl1—O1	108.66 (12)
C9—C4—C3	123.21 (19)	O2—Cl1—O4	110.18 (11)
C6—C5—C4	120.4 (2)	O2—Cl1—O3	110.27 (14)
C7—C6—C5	120.7 (2)	O4—Cl1—O1	110.37 (11)
C6—C7—C8	119.6 (2)	O4—Cl1—O3	108.80 (11)
C7—C8—C9	120.7 (2)	O1—Cl1—O3	108.54 (13)
Torsions			
N1—C3—C4—C5	174.53 (19)	N3—C3—N1—C1	−1.6 (3)
N3—C3—C4—C5	−5.4 (3)	C4—C3—N1—C1	178.54 (17)
N3—C3—C4—C9	173.9 (2)	N4—C1—N1—C3	179.98 (18)
N2—C1—N1—C3	−1.7 (3)	N1—C3—C4—C9	−6.1 (3)
C9—C4—C5—C6	1.4 (4)	N4—C1—N2—C2	−177.39 (19)
C3—C4—C5—C6	−179.3 (2)	N1—C1—N2—C2	4.3 (3)
C5—C6—C7—C8	0.5 (4)	N5—C2—N2—C1	174.78 (18)
C4—C5—C6—C7	−1.2 (4)	N3—C2—N2—C1	−4.3 (3)
C6—C7—C8—C9	0.0 (5)	N1—C3—N3—C2	1.8 (3)
C7—C8—C9—C4	0.2 (5)	C4—C3—N3—C2	−178.33 (16)
C3—C4—C9—C8	179.8 (2)	N5—C2—N3—C3	−177.84 (18)
C5—C4—C9—C8	−0.8 (4)	N2—C2—N3—C3	1.2 (3)

Table III. 3. Geometric properties of the hydrogen bonds (Å, °)

D—H···A	*D*—H	H···A	*D···A*	*D*—H···*A*
N1—H1N···O3	0.751	2.189	2.923	165.46
N4—H4O···O1	0.828	2.270	3.051	157.40
N4—H4O···O3	0.828	2.725	2.752	135.17
N4—H4N···O1	0.817	2.703	3.248	125.66
N4—H4N···O4	0.817	2.407	3.114	145.47
N4—H4N···N5	0.817	2.892	3.479	130.56
N5—H5N···N2	0.804	2.295	3.091	170.56
N5—H5N···N4	0.804	2.949	3.479	125.57
N5—H5O···O2	0.790	2.325	3.088	162.49
C7—H7···O4	0.950	2.718	3.658	170.05
C6—H6···O2	0.950	2.632	3.317	129.39
C9—H9···O3	0.950	2.417	3.352	167.87

III.2.1.1 3D supra-molecular network

The figure III. 2 presents the 3D supramolecular network of the title material. It shows that the network is formed by supramolecular chains along the (Oa) direction (Figure III. 2 (a)), these chains consist of an alternation of $C_9H_{10}N_5^+$ cations and ClO_4^- anions moieties, the anions moiety links two cations by hydrogen bonds C7—H7···O4 and N4—H4N···O4. In addition, two largest supramolecular rings having the path sets $R_4^4(18)$ and $R_4^4(12)$ were formed; each ring possesses a symmetry center, keeping the two each successive chains almost parallel and in opposite manner (Figure III. 2 (b)).

Otherwise, along the perpendicular direction (Ob), the 3D supra-molecular network shows a parallel-displaced π-stacking (Figure III. 2 (c)), with a separation distance between the benzene rings 3.472Å, noting the presence of two hydrogen bonds N4—H4O···O1 and N4—H4N···O1 between two stacked molecules. The stacked molecules form two supramolecular organic layers as shown in the figure III. 2 (d) these layers are related by N5—H5N···N2, N5—H5N···N4, N5—H5N···N4 and N4—H4N···N5 hydrogen bonds, an angle of 69.86° between two successive organic layers, in which, the anions are located between each two organic supramolecular layers (Figure III. 2 (d)). In conclusion, the synthetized compound is a hybrid type I material, formed by self-assembled supramolecular layer by supramolecular layer.

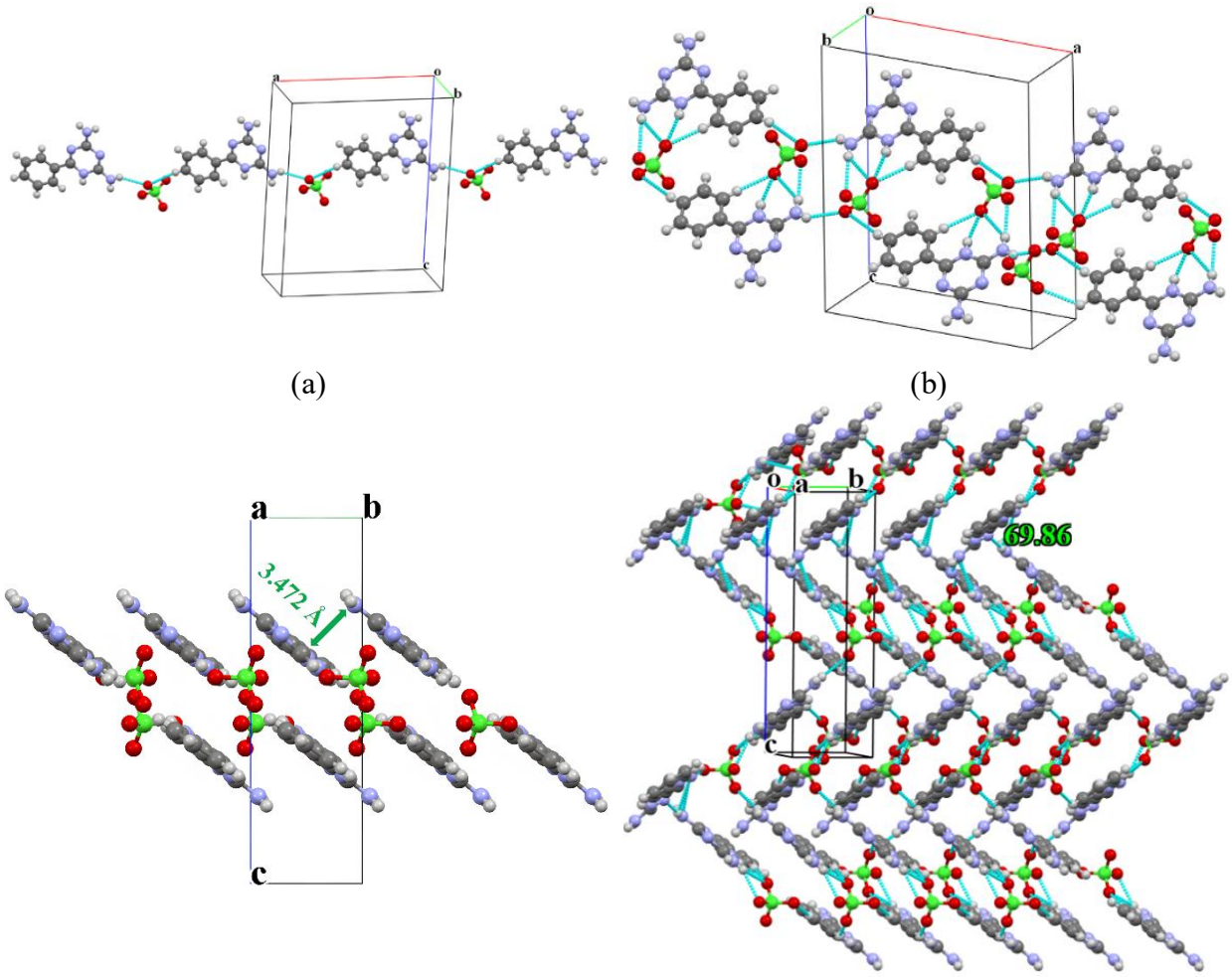

Figure III. 2. (a) and (b) Supra-molecular chains along (Oa) direction, (c) Supra-molecular parallel-displaced π-stacking formed along (Ob) direction, (d) Supra-molecular network along (Ob) direction.

III.2.2 Spectroscopy studies

III.2.2.1 FT-IR spectroscopy

FT-IR spectrum of crystal $C_9H_{10}N_5^+.ClO_4^-$ is illustrated in the figure III. 3. The topical significant infrared adsorption wavenumbers arise from internal vibrations of 2,4-diamino-6-phenyl-1,3,5-triazinium cation, perchlorate anion and from the vibrations of hydrogen bonds. The wavenumbers are tabulated and assigned in the table III. 4.

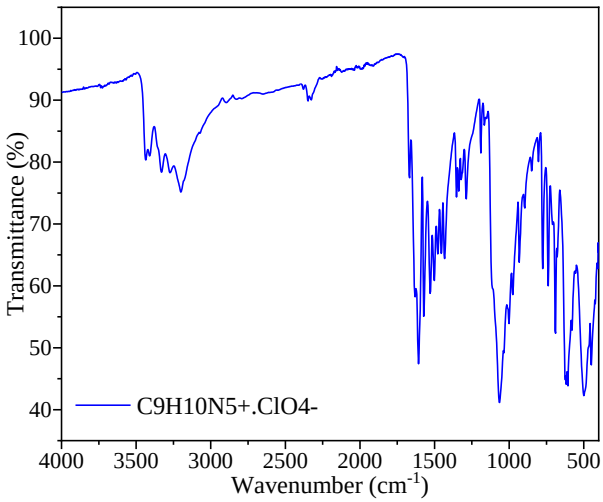

Figure III. 3. FT-IR spectrum of 2,4-diamino-6-phenyl-1,3,5-triazinium perchlorate.

Bands appeared in the range 3430-3050 cm^{-1} were assigned to stretching vibrations mode of NH_2 groups, vibrations of hydrogen bonds and C–H aromatic [6]. The NH bending vibrations was appeared at 1669 cm^{-1} [7] while, the bands related to the triazine ring stretching vibrations are located in the range 1630-1420 cm^{-1} [8]. Whereas, IR bands corresponding to the ClO_4^- stretching vibration of was observed at 1064 cm^{-1} [9].

Table III. 4. FT-IR vibrational wavenumbers and their assignments.

Wavenumber (cm^{-1})	Assignment
3434	NH_2 asymmetric stretching
3408	NH_2 symmetric stretching
3327	NH_2 symmetric stretching
3270 and 3203	N–H Vibrations of the hydrogen bonds
3071	C–H aromatic
2892, 2797	Combination tone: NH_2 symmetric stretch-side chain out of plane C-N bonds
1669	bending vibrations of NH
1629,1606	Benzene ring
1567, 1528	Triazine ring vibration
1502	Side-chain asymmetric stretching of C–N group
1480	triazine ring vibration
1454 and 1429	Ring: semi-circle stretching + exogenous C–N contract
1285	Benzene C–H deformation
1189	ClO_4^- asymmetric stretching vibration
1064	ClO_4^- symmetric stretching vibration
978	Triazine ring N, in phase radial vibration
774	out of plane bending vibration of triazing
691	Symmetric type triazine ring
613	ClO_4^- asymmetric bending type of vibration
567	C-N bending vibration
421	ClO_4^- torsion mode of vibration

III.2.2.2 UV-Vis. spectroscopy

Electronic absorption spectrum of $C_9H_{10}N_5^+.ClO_4^-$ (Figure III. 4) exhibits two absorption bands in the UV region at a maxima of 204 and 247 nm, that can be related to $\pi \rightarrow \pi^*$and $n \rightarrow \pi^*$electronic transitions respectively. Whereas, the molecule has no absorption bands from 307 to 800 nm.

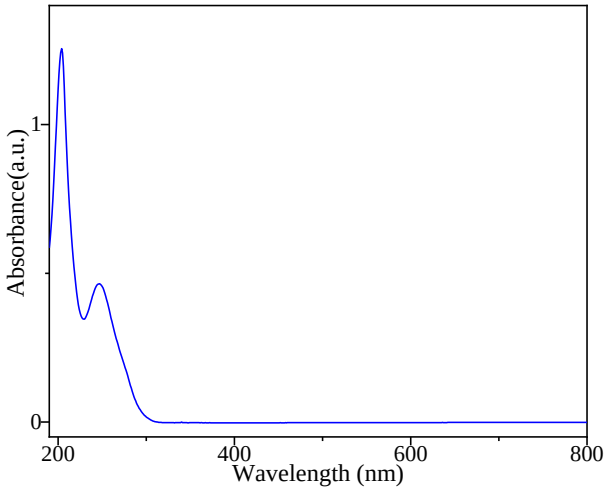

Figure III. 4. UV-Vis. electronic spectrum of 2,4-diamino-6-phenyl-1,3,5-triazinium perchlorate.

III.2.2.3 Thermo-gravimetric studies

TGA/DTG curves characteristic of the starting material and the synthesized hybrid ionic compound are shown in the Figure III. 5 ((a) and (b)) respectively. TGA curve of the started material illustrates that the benzoguanamine is thermally stable until 200 °C, and then the decomposition occurs totally at 324 °C, as shown by the non-asymmetric DTG curve, the benzoguanamine is characterized by a multi-stages decomposition, noting the absence of intermediate stable by-products.

The TGA curve of the hybrid material shows an enhanced thermal stability up to 290 °C, comparatively to benzoguanamine a more gradual decomposition can be seen, occurring in four stages. The first, the second and the third stages take place in the range of temperature from 290 to 640°C with a significant weight-loss of 68.42 %, indicating the elimination of organic moieties, accompanied by a DTG peaks at 327, 362, and 553 °C. Whereas, the last decomposition stage takes place from 640 °C, and is related to the gradual elimination of perchlorate anion moieties, with a related DTG peak seen at 771 °C.

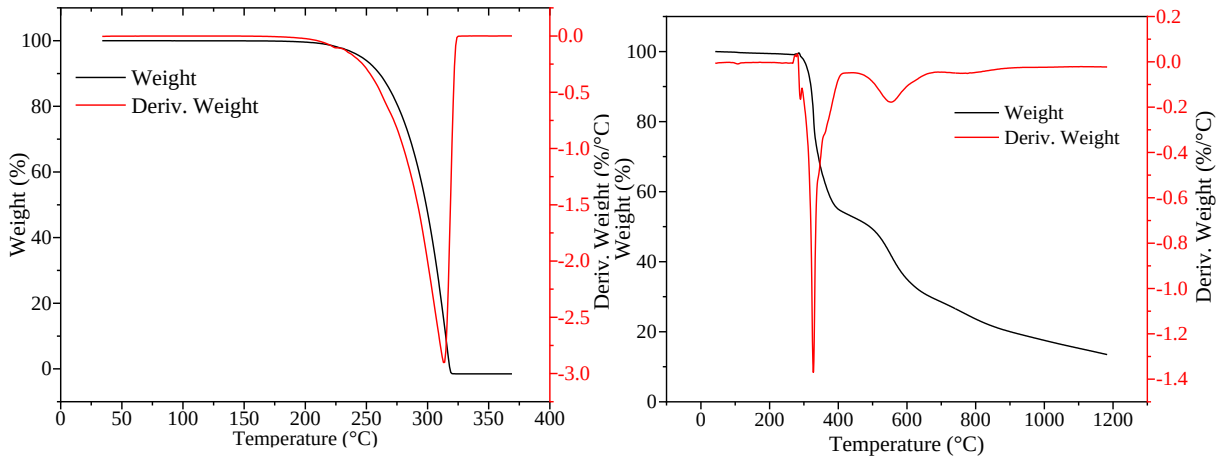

Figure III. 5. TGA/DTG curves of (a) benzoguanamine and (b) 2,4-diamino-6-phenyl-1,3,5-triazinium perchlorite.

III.1 Second material

III.1.1 SXRD study

The asymmetric unit of $C_3H_8N_6^{2+}.2ClO_4^-.H_2O$ is composed of one H_2O molecule, an organic cation $C_3H_8N_6^{2+}$ moiety, and two inorganic anions ClO_4^- moieties, as depicted in the Figure III. 6(a). In addition, the crystal description, experimental crystal data and structural refinement parameters are listed in the table III. 5, and the characteristic geometric parameters (bond lengths and interatomic angles) are listed in the table III. 6. The ionic coumpound crystallizes in the triclinic system (Figure III. 6 (b)) with P^{-}_{1} symmetry group, characterized by the cell parameters a=5.9126 (4), b=9.2661 (6), c = 11.1489 (8) Å, α = 97.719 (2), β = 90.429 (2), and γ = 98.929 (2) °, the unit cell contains twenty-seven inversion centers (Figures III. 6 (c)).

Furthermore, the XRD illustrates that weak contacts, particularly hydrogen bonds, maintain the crystal structure, given also a type I hybrid material. Each unit cell has 12 extra-molecular hydrogen bonds under 3.0 Å as maximum donor-acceptor distance. The table III. 7 provides the types, typical distances, and angle measurements.

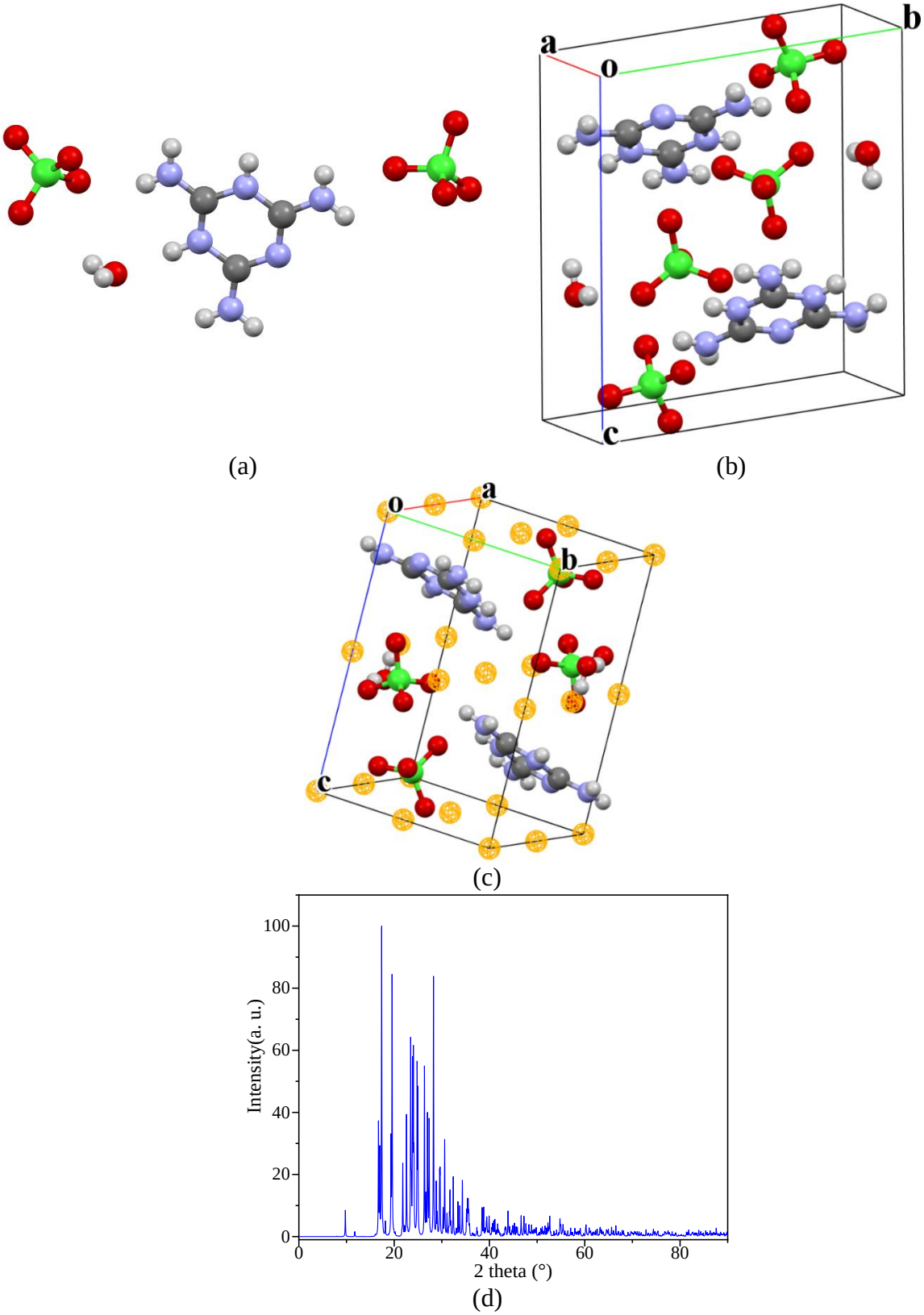

Figure III. 6. (a) Asymmetric unit (b) unit cell (c) unit cell provided by inversion center (yellow color) for the 2,4,6-triamino-1,3,5-triazin-1,3-dium bisperchlorate monohydrate, (d) powder XRD pattern.

Table III. 5. Crystal data structure and the parameters of the refinement.

Empirical formula	$C_3H_{10}Cl_2N_6O_9$
Molecular weight (g/mol)	345.07
Crystal color/habit	Colourless/Prism
Crystal system	Triclinic
Space group	$P\bar{1}$
a (Å)	5.9126 (4)
b (Å)	9.2661 (6)
c (Å)	11.1489 (8)
α (°)	97.719 (2)
β (°)	90.429 (2)
γ (°)	98.929 (2)
V (Å^3)	597.69 (7)
Z	2
Crystal size (mm^3)	0.60*0.55*0.52
D (Mg/m^3)	1.917
$\lambda_{MoK\alpha 1}$ (Å)	0.7107
T (K)	150
F(000)	352
μ (mm^{-1})	0.61
θ Range (°)	3.1→ 27.5
$\Delta\rho_{min}$ (eÅ^{-3})	-0.48
$\Delta\rho_{max}$ (eÅ^{-3})	0.38
H	-7 → 7
K	-12 → +12
L	-14→ 14
Independent reflections	2706
Measured reflections	11231
reflections with I>2σ(I)	2518
No. of parameters	222
R_{int}	0.029
$wR(F^2)$	0.075
R [$F^2>2\sigma(F2)$]	0.029
S	1.05

Table III. 6. Geometric parameters (Å, °) characteristic of the second hybrid compound.

		Distances	
C1—N4	1.301 (2)	Cl1—O1	1.4295 (12)
C1—N1	1.345 (2)	Cl1—O3	1.4332 (12)
C1—N2	1.350 (2)	Cl1—O2	1.4366 (12)
C2—N5	1.3128 (19)	Cl1—O4	1.4565 (12)
C2—N3	1.3231 (19)	Cl2—O5	1.4293 (12)
C2—N2	1.3771 (19)	Cl2—O7	1.4379 (12)
C3—N6	1.306 (2)	Cl2—O6	1.4412 (14)
C3—N3	1.3340 (19)	Cl2—O8	1.4475 (13)
C3—N1	1.3752 (19)		
		Angles	
N4—C1—N1	121.69 (16)	O1—Cl1—O3	109.77 (8)
N4—C1—N2	120.61 (16)	O1—Cl1—O2	110.05 (8)
N1—C1—N2	117.69 (14)	O3—Cl1—O2	110.09 (8)
N5—C2—N3	120.16 (14)	O4—Cl1—O1	109.05 (9)
N5—C2—N2	117.63 (14)	O4—Cl1—O3	109.22 (8)
N3—C2—N2	122.22 (13)	O2—Cl1—O4	108.64 (7)
N6—C3—N3	119.46 (14)	O5—Cl2—O7	110.99 (8)
N6—C3—N1	118.21 (14)	O5—Cl2—O6	109.60 (9)
N3—C3—N1	122.32 (13)	O6—Cl2—O7	109.46 (9)
C3—N1—C1	120.17 (13)	O5—Cl2—O8	109.49 (9)
C1—N2—C2	120.39 (13)	O7—Cl2—O8	108.77 (8)
C2—N3—C3	117.04 (13)	O6—Cl2—O8	108.49 (10)
		Torsions	
N2—C1—N1—C3	1.9 (2)	N5—C2—N2—C1	177.45 (14)
N4—C1—N1—C3	−178.38 (14)	N3—C2—N2—C1	−2.8 (2)
N6—C3—N1—C1	175.99 (14)	N5—C2—N3—C3	−179.95 (13)
N1—C1—N2—C2	1.6 (2)	N2—C2—N3—C3	0.3 (2)
N4—C1—N2—C2	−178.12 (14)	N6—C3—N3—C2	−177.23 (14)
N3—C3—N1—C1	−4.5 (2)	N1—C3—N3—C2	3.3 (2)

Table III. 7. Geometric properties of the hydrogen bonds (Å, °).

D—*H*···*A*	*D*—H	H···A	*D*···*A*	*D*—H···*A*
N2—H2···O4	0.814	2.359	3.030	140.25
N5—H5A···O4	0.802	2.317	2.999	143.45
N6—H6B···O4	0.830	2.265	3.046	157.13
N6—H6A···Cl1	0.863	2.959	3.732	149.95
N6—H6A···O2	0.863	2.156	2.992	163.06
N6—H6A···O1	0.863	2.733	3.288	123.38
N5—H5B···O3	0.851	2.117	2.956	168.45
N4—H4A···O8	0.793	2.119	2.866	157.12
N4—H4B···Cl2	0.881	2.812	3.664	160.65
N4—H4B···O6	0.881	2.023	2.894	170.13
N4—H4B···O7	0.881	2.611	3.252	130.47
O11—H11A···O5	0.813	2.248	3.014	157.33

III.1.1.1 3D supra-molecular network

At 3D, the self-assembly of the $C_3H_8N_6^{2+}$ cations, ClO_4^- anions and H_2O molecules forms an ordered supramolecular network, i. e. the molecules are held together by non-covalent interactions, mainly of the type hydrogen bonds and ionic interactions. The 3D supra-molecular network can be seen as interconnection of various supramolecular chains. Along the (Oa) direction, two types of supramolecular chains can be seen. The first chain is hybrid and made up by an alternating of $C_3H_8N_6^{2+}$ cations and ClO_4^- anions moieties linked together by N6—H6B···O4, N2—H2···O4 and N5—H5A···O4 hydrogen bonds (Figure III. 7 (a)). The second is inorganic made up by ClO_4^- anions and H_2O molecules, linked by O11—H11A···O5 hydrogen bonds (Figure III. 7 (c)). Along the perpendicular plans, the both chains form supramolecular layers (Figure III. 7 (b and d)). In addition, the carrier plans of the supramolecular layers are parallel, and transversal to the (Oc) axis (Figure III. 7 (f)), making the title crystal as layered-like material, in which, an alternation of two hybrid supramolecular layers by one supramolecular inorganic layer can be remarked (Figure III. 7 (f)). Each two hybrid layers are linked by hydrogen bonds via perchlorate anions of the type N6—H6A···Cl1, N6—H6A···O1, N6—H6A···O2 and N5—H5B···O3, while the hybrid and inorganic supramolecular layers are linked by N4—H4A···O8, N4—H4B···Cl2, N4—H4B···O6 and N4—H4B···O7 hydrogen bonds. Furthermore, two large supramolecular rings were formed having the path sets $R_4^4(20)$ and $R_5^5(20)$, each ring has a symmetry center, making each two consecutive hybrid layers in opposite manner (Figure III. 7 (e)).

Otherwise, chains along the direction (10-3) can be seen, linked by hydrogen bonds of the type N2—H2···O4, N5—H5A···O4, N6—H6B···O4, N6—H6A···Cl1, N6—H6A···O1 and N6—H6A···O2 (Figure III. 8 (j)). These cahins are caused by a parallel-displacer stacking of the triazin rings along (Oa) direction (Figure III. 7 (a)), which the distance between two consicutive rings is 3.328 Å (Figure III. 7 (h)).

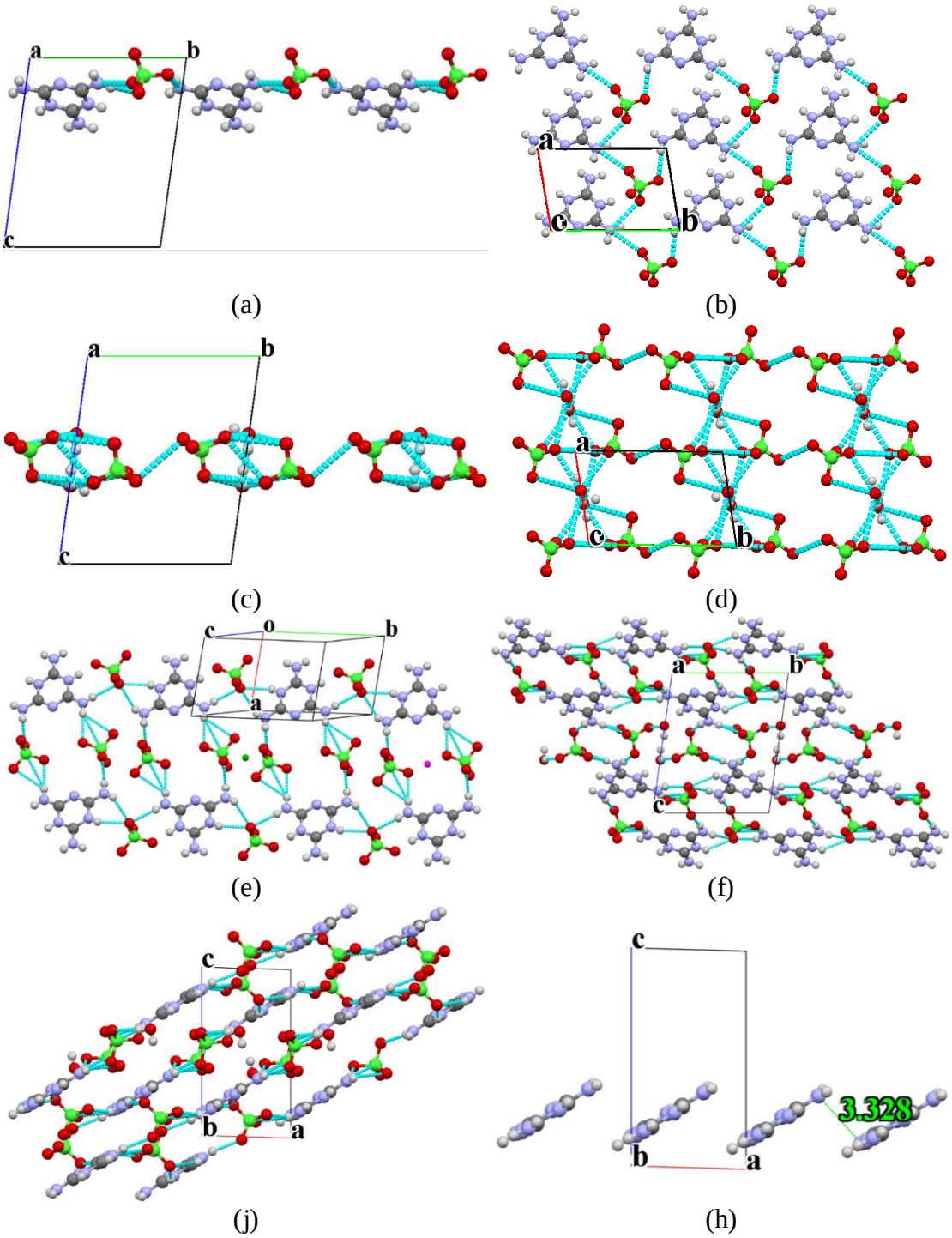

Figure III. 7. (a) Supramolecular hybrid chain along (Oa) direction illustrating the alternation of the anion and cation molecules, (b) supramolecular hybrid layer along the plan (Oab), (c) inorganic supramolecular chain, (d) supramolecular inorganic layer along the plan (Oab), (e) illustration of the junction between the two hybrid supramolecular chains, provide by the symmetry centers, (f) 3D supramolecular network illustrating lamellar-like structure, (g) remarked supramolecular chains along the direction (1, 0, -3), (h) parallel-displacer stacking of the triazin rings along (Oa) direction.

III.1.2 Spectroscopy studies

III.1.2.1 FT-IR spectroscopy

The figure III. 8 shows FT-IR spectrum of $C_3H_8N_6^{2+}.2ClO_4^-.H_2O$ crystal. The characteristic significant infrared adsorption wavenumbers arise from, perchlorate anions, internal vibrations of double protonated melamine cation, the vibrations of water molecule and vibrations characteristic of hydrogen bonds are collected and assigned in table III. 8.

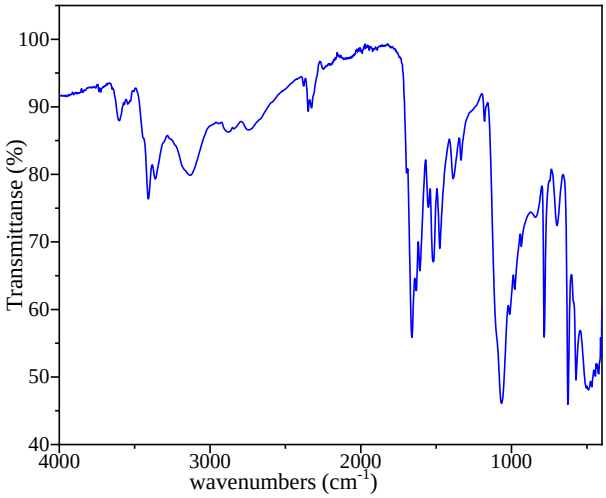

Figure III. 8. FT-IR spectrum of the 2,4,6-triamino-1,3,5-triazin-1,3-dium bisperchlorate monohydrate ($C_3H_8\ N_6^{2+}.2Cl\ O_4^-.H_2O$).

The bands observed in the region 3600-3100 cm^{-1} were related to water molecules' vibration [10], NH_2 groups stretching. Whereas, the bands related to the bending vibrations of NH and OH are appeared at 1660 and 1633 cm^{-1} respectively [7]. The IR bands corresponding to the stretching vibrations of the triazine-ring are located in 1600-1480 cm^{-1} range [8]. In addition, a new bands observed at 1071cm^{-1} is due to the stretching vibration of ClO_4^- [9]. All this assignments are conform to XRD-affined structure.

Table III. 8. FT-IR vibrational wavenumbers and their assignments.

	Assignments
3604	O–H asymmetric stretching of water
3541	O–H symmetric stretching of water
3408	NH_2 asymmetric stretching
3361	NH_2 symmetric stretching
3135	N–H of the hydrogen bonds
2875, 2739	Combination tone: NH_2 symmetric stretch-side chain out of plane C-N bonds
2344, 2327	Vibrations in hydrogen bonds formed by the molecules of water
1660	bending vibrations of NH
1633	bending vibrations of OH
1606,1552	Triazine ring vibration
1475	Side-chain asym C-N stretch
1071	ClO_4^- symmetric stretching vibration
779	out of plane bending of sextant ring
698	Symmetric type triazine ring
621	ClO_4^- asymmetric bending type
567	C-N bending vibration
494	ClO_4^- torsion mode of vibration

III.1.2.2 UV-Visible spectroscopy

The figure III. 9 shows the electronic absorption spectrum of $C_3H_8N_6^{2+}.2ClO_4^-.H_2O$, it illustrates two adsorption bands in UV region at 207 and 235 nm related respectively to $\pi \rightarrow \pi^*$and $n \rightarrow \pi^*$electronic transition. Whereas, the material is transparent in the visible and UV-near visible regions.

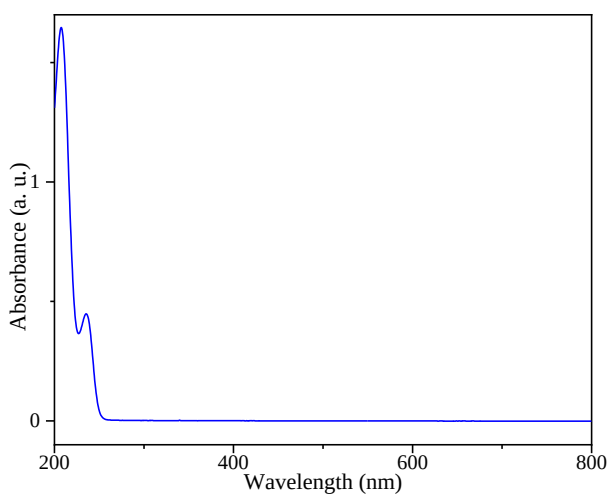

Figure III. 9. UV–Visible absorption electronic spectrum of 2,4,6-triamino-1,3,5-triazin-1,3-dium bisperchlorate monohydrate ($C_3H_8\ N_6^{2+}.2Cl\ O_4^-.H_2O$).

III.1.3 Thermo-gravimetric studies

The TGA/DTG curves of $C_3H_8N_6^{2+}.2ClO_4^-.H_2O$ is illustrated in the figure III. 10, it shows that its dehydration and decomposition occurs in five stages up to 800 °C. The first stage takes place from 163 to 219 °C temperature range, indicating that the structural water is eliminated, accompanied by a DTG peak at 186 °C. Moreover, the second, third, and fourth stages of decomposition take place from 256 to 539 °C temperature range and is due to the elimination of melaminium moiety with a corresponding DTG peaks observed at 287 °C, 347 °C and 452 °C respectively. Whereas, the last stage observed from 544 to 728 °C, and is due to the elimination of perchlorate anion moieties, with a related DTG peak is seen at 620 °C. Noting that, TGA curve proves that this hybrid is thermally stable up to 237 °C.

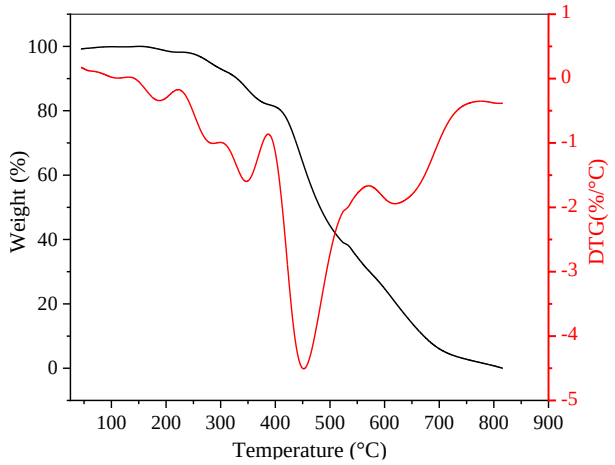

Figure III. 10. TGA-DTG curves of the 2,4,6-triamino-1,3,5-triazin-1,3-dium bisperchlorate monohydrate ($C_3H_8\ N_6^{2+}.2Cl\ O_4^-.H_2O$).

III.2 Conclusions

Two new hybrid ionic crystals: 2,4-diamino-6-phenyl-1,3,5-triazinium perchlorate ($C_9H_{10}N_5^+.ClO_4^-$) and 2,4,6-triamino-1,3,5-triazin-1,3-dium bisperchlorate monohydrate ($C_3H_8\ N_6^{2+}.2Cl\ O_4^-.H_2O$) were synthesized successfully. The structures of the ionic hybrid crystals was studied experimentally by single crystal XRD, showing that 2,4-diamino-6-phenyl-1,3,5-triazinium perchlorate crystalizes in monoclinic system, while 2,4,6-triamino-1,3,5-triazin-1,3-dium bisperchlorate monohydrate crystalizes in triclinic system. The weak interactions maintain the structure's stability, giving a hybrid ionic crystals type I. The optoelectronic properties have been studied experimentally by UV-Visible spectroscopy, illustrating two absorption bands in the UV domain located at the maxima of 204 and 247nm for the 2,4-diamino-6-phenyl-1,3,5-triazinium perchlorate. While for 2,4,6-triamino-1,3,5-triazin-1,3-dium bisperchlorate

monohydrate have two absorbance bands in the UV domain located at the maxima of 207 and 235nm, noting a good transparency in ultraviolet-visible and entire visible domains. Various infrared modes were indicated and assigned, in which various modes confirm the presence of inter molecular hydrogen bonds within the crystals. The 2,4-diamino-6-phenyl-1,3,5-triazinium perchlorate title is stable until 290 °C, while, the 2,4,6-triamino-1,3,5-triazin-1,3-dium bisperchlorate monohydrate is stale until 256 °C, making them suitable for thermal applications.

III.3 References

[1] E. Bouaziz, O. Kammoun, A. Slassi, D. Cornil, J. Lhoste, S. Auguste and M. Boujelbene, "A supramolecular non centrosymmetric 2,6-diaminopyridinium perchlorate salt: Crystal structure and optoelectronic DFT study," *Journal of Molecular Structure*, vol. 1267, p. 133561, Nov. 2022, doi: 10.1016/j.molstruc.2022.133561.

[2] R. Bourzami, H. C. AitYoucef, N. Hamdouni, and M. Sebais, "Synthesis, crystal structure, vibrational spectra and thermal properties of novel ionic organic-inorganic hybrid material," *Chemical Physics Letters*, vol. 711, pp. 220–226, Nov. 2018, doi: 10.1016/j.cplett.2018.08.002.

[3] H. Chenefa AitYoucef and R. Bourzami, "Synthesis, single crystal X-ray structure and vibrational spectroscopic characterization study of a new hybrid material crystal: Bis(2,4,6-trihydroxy-1,3,5-triazin-1-ium) bischloride monohydrate," *Journal of Molecular Structure*, vol. 1191, pp. 218–224, Sep. 2019, doi: 10.1016/j.molstruc.2019.03.039.

[4] L. Ouksel, S. Chafaa, R. Bourzami, N. Hamdouni, M. Sebais, and N. Chafai, "Crystal structure, vibrational, spectral investigation, quantum chemical DFT calculations and thermal behavior of Diethyl [hydroxy (phenyl) methyl] phosphonate," *Journal of Molecular Structure*, vol. 1144, pp. 389–395, Sep. 2017, doi: 10.1016/j.molstruc.2017.05.029.

[5] Y. Bellal, S. Keraghel, F. Benghanem, L. Toukal, G. Sigircik, R. Bourzami and A. Ourari, "A New Inhibitor for Steel Rebar Corrosion in Concrete: Electrochemical and Theoretical Studies," *International Journal of Electrochemical Science*, vol. 13, no. 7, pp. 7218–7245, Jul. 2018, doi: 10.20964/2018.07.91.

[6] S. Selvaraj, A. R. Kumar, T. Ahilan, M. Kesavan, G. Serdaroglu, P. Rajkumar, M. Mani, S. Gunasekaran and S. Kumaresan, "Experimental and Theoretical Spectroscopic Studies of the Electronic Structure of 2-Ethyl-2-phenylmalonamide," vol. 10, no. 3, doi: https://doi.org/10.22036/PCR.2021.304087.1966.

[7] H. A. Youcef, S. Chafaa, R. Doufnoune, and T. Douadi, "Synthesis, characterization and thermal behavior of tetrakis(melamine2+) bis(melamine+) pentakis(monohydrogenphosphate) tetrahydrate," *Journal of Molecular Structure*, vol. 1123, pp. 138–143, Nov. 2016, doi: 10.1016/j.molstruc.2016.05.073.

[8] X. Yuan, K. Luo, K. Zhang, J. He, Y. Zhao, and D. Yu, "Combinatorial Vibration-Mode Assignment for the FTIR Spectrum of Crystalline Melamine: A Strategic Approach toward

Theoretical IR Vibrational Calculations of Triazine-Based Compounds," *J. Phys. Chem. A*, vol. 120, no. 38, pp. 7427–7433, Sep. 2016, doi: 10.1021/acs.jpca.6b06015.

[9] Z. Fellahi, H. C.-Ait Youcef, D. Hannachi, A. Djedouani, L. Ouksel, M. François, S. Fleutot and R. Bourzami, "Synthesis, X-ray crystallography, Hirshfeld surface analysis, thermal properties and DFT/TD-DFT calculations of a new material hybrid ionic (C10H18N2O82+.2ClO4−.4H2O)," *Journal of Molecular Structure*, vol. 1244, p. 130955, Nov. 2021, doi: 10.1016/j.molstruc.2021.130955.

[10] M. Stomp, J. Huisman, L. J. Stal, and H. C. P. Matthijs, "Colorful niches of phototrophic microorganisms shaped by vibrations of the water molecule," *The ISME Journal*, vol. 1, no. 4, pp. 271–282, Aug. 2007, doi: 10.1038/ismej.2007.59.

Structural, spectroscopy, thermal and thermodynamic and NLO properties of three imidazolium based ionic liquids: theoretical and experimental approaches

IV. Structural, spectroscopy, thermal and thermodynamic and NLO properties of three imidazolium based ionic liquids: theoretical and experimental approaches

IV.1 Introduction

A quantum chemical calculation method is a technique for computing observables directly related to experiments, such as structural, thermal, thermodynamic, optical, and spectroscopic properties, using quantum-chemical methodologies such as density functional theory (DFT). This later was performed to study in depth various physical and chemical properties of three imidazolium based ionic liquids, as well as experimental methods. Quantum chemical computations were used to detrmine in depth the optimized molecular structure, mapping electrostatic potential (MEP), partial charges, molecular orbitals (MOs) and their related energies. The vibrational spectra were obtained through both theoretical and experimental methods, during which the vibrational and the electronic adsorption bands were all assigned. In addition, some thermodynamic parameters were calculated as a function of temperature. Optical and the nonlinear optical properties were also computed.

IV.2 Optimized geometries

DFT simulations were used to theoretically optimize the molecular structures of the $VBmim^+$ cation, [$VBmim^+$, Cl^-], [$VBmim^+$, PF_6^-], and [$VBmim^+$, NTF_2^-] ILs. The figures IV. 1 (a, c, e and g) shows their optimized structures. They effectively demonstrate how all molecule configurations deviate greatly from a planar geometry. For all molecular structure, the imidazole and aromatic ring are part of two distinct plans, the angles between the carrier plans are 92.60, 112.86, 107.99 and 101.27° with distortion values of -66.53, 47.55, 56.15 and 40.05° for $VBmim^+$ cation, [$VBmim^+$, Cl^-], [$VBmim^+$, PF_6^-] and [$VBmim^+$, NTF_2^-], respectively. It can be concluded that the weak-bonded anion type influences the distortion of cationic parts of ILs, noting that all ionic liquids are distorted relative to the $VBmim^+$ cation. These results are in good agreement with previous research on related molecular materials [1] [2]. Additionally, the table IV. 1 compiles a few distinctive bond lengths and angles. It is noticeable that, comparing the cationic-nitrogen's tetrahedral geometry to the ideal tetrahedral shape for all ILs materials under study reveals a skew. (Table IV. 1).

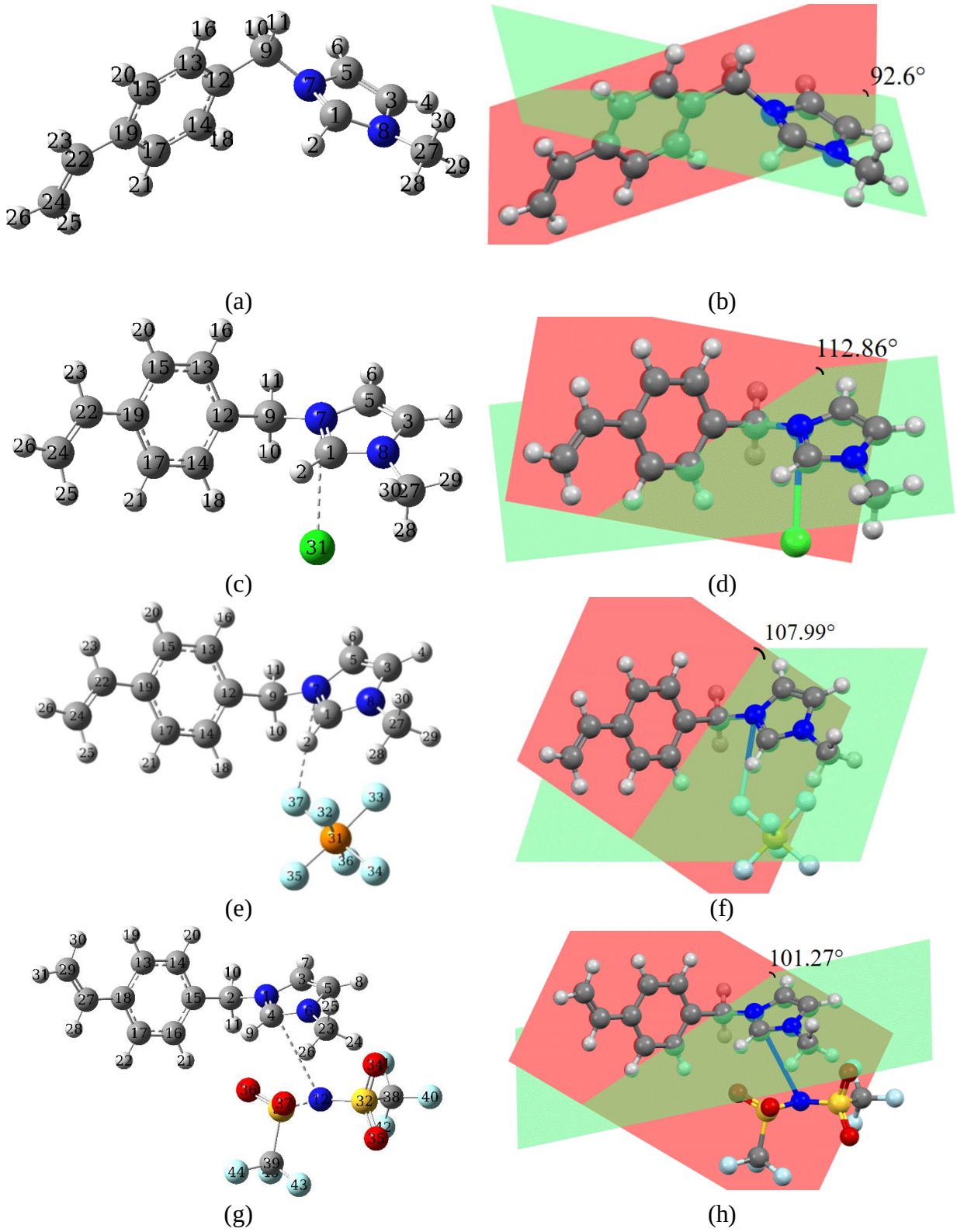

Figure IV. 1. Optimized molecular structures and angles between the carrying plans for $VBmim^+$ cation (a and b), [$VBmim^+$, Cl^-] (c and d), [$VBmim^+$, PF_6^-] (e and f) and [$VBmim^+$, NTF_2^-] (g and h).

Table IV. 1. Common theoretical bond lengths and angles of $VBmim^+$ cation, [$VBmim^+$, PF_6^-], [$VBmim^+$, Cl^-], and [$VBmim^+$, NTF_2^-].

$VBmim^+$			
Lengths of bonds (Å)		Angles of bonds (°)	
C1—N7	1.419	C1—N7—C5	107.616
C1—N8	1.416	C1—N7—C9	121.050
C3—C5	1.351	C5—N7—C9	122.809
C3—N8	1.393		
C5—N7	1.396		
[$VBmim^+$, Cl^-]			
Lengths of bonds (Å)		Angles of bonds (°)	
C1—N7	1.341	C1—N7—C5	108.216
C1—N8	1.341	C1—N7—C9	123.692
C3—C5	1.356	C1—N7—Cl31	054.504
C3—N8	1.387	C5—N7—C9	125.115
C5—N7	1.387	C5—N7—Cl31	109.645
N7---Cl31	3.253	C9—N7—Cl31	088.912
		N7—C9—C12	113.171
[$VBmim^+$, PF_6^-]			
Lengths of bonds (Å)		Angles of bonds (°)	
C1—N7	1.334	C1—N7—C5	108.457
C1—N8	1.333	C1—N7—C9	124.827
C3—C5	1.360	C1—N7—F37	063.992
C3—N8	1.382	C5—N7—C9	126.368
C5—N7	1.382	C5—N7—F37	136.036
N7---F37	3.265	C9—N7—F37	71.969
		N7—C9—C12	112.925
[$VBmim^+$, NTF_2^-]			
Lengths of bonds (Å)		Angles of bonds (°)	
N1—C3	1.383	C2—N1—C3	125.474
N1—C4	1.335	C2—N1—C4	125.659
N1---N12	4.076	C2—N1—N12	101.474
C3—C5	1.360	C3—N1—C4	108.307
C4—N6	1.335	C3—N1—N12	084.887
C5—N6	1.380	C4—N1—N12	074.056
		N1—C2—C15	112.722

The theory known as valence shell electron pair repulsion (VSEPR) is in agreement with the distortion caused by the presence of anions [3], [4], and other nitrogen-cationic molecular compounds [5], [6]. On another hand, the reported comparison of the $VBmim^+$ cation and the studied geometries of ionic liquids demonstrate that the anions deform significantly the molecular shape, mainly around the charge transfer sites. For example, the C1—N7 bond length is 1.419, 1.341 and 1.334 Å for the $VBmim^+$ cation, [$VBmim^+$, Cl^-] and [$VBmim^+$, PF_6^-] respectively and the N1—C4 bond length is 1.335 Å for the [$VBmim^+$, NTF_2^-]. The angle measurements

C1—N7—C5 are 107.62, 108.22 and 108.46° for the $VBmim^+$ cation, [$VBmim^+$, Cl^-] and [$VBmim^+$, PF_6^-] respectively and The C3—N1—C4 angle is 108.31° for the [$VBmim^+$, NTF_2^-], the values of the imidazole ring's internal angles likewise show this relative distortion [1].

IV.3 Vibrational analysis

The FTIR/ATR spectra for the [$VBmim^+$, PF_6^-], [$VBmim^+$, Cl^-], and [$VBmim^+$, NTF_2^-] ILs are shown in the figure IV. 2. The vibrational frequencies and their assignments are listed in the table IV. 2, which also shows how well the experimental and theoretical frequencies agree. The spectra show three distinct spectral regions: 3500-2700, 1700-1000, and 1000-400 cm^{-1}.

- Region 3500-2700 cm^{-1}

The weak bands between 3500 and 2700 cm^{-1} are associated with stretching modes of ν(C-H). For [$VBmim^+$, Cl^-], [$VBmim^+$, PF_6^-], and [$VBmim^+$, NTF_2^-], the C-H stretching vibrations of the imidazole ring are observed at 3135, 3164, and 3152 cm^{-1}, respectively [1]. The phenyl ring's ν(C-H) vibration bands are situated at 3047, 3074, and 3090 cm^{-1} for [$VBmim^+$, Cl^-], [$VBmim^+$, PF_6^-], and [$VBmim^+$, NTF_2^-], respectively [7] [8]. The vinyl group's ν(C-H) is observed at 3038 cm^{-1} for the [$VBmim^+$, Cl^-], 3036 cm^{-1} for the [$VBmim^+$, PF_6^-], and 3011 cm^{-1} for the [$VBmim^+$, NTF_2^-]. Furthermore, the bands that appear in the 2855–2977 cm^{-1} range result from the methyl and methylene groups' symmetric and asymmetric stretching [9] [10].

- Region 1700-1000 cm^{-1}

The phenyl ring's ν(C=C) is found in this area between 1500 and 1611 cm^{-1} [10], whereas the vinyl group's ν(C=C) is in charge of the band at 1628 cm^{-1} [1]. For [$VBmim^+$, Cl^-], [$VBmim^+$, NTF_2^-], and [$VBmim^+$, PF_6^-], the bending vibrations of the CH_2 and CH_3 groups are detected in the range of 1454-1382, 1451-1387, and 1455-1378 cm^{-1}, respectively [11]. The imidazolium ring's (C-C) and (C=C)/(C=N) stretching vibrations are detected at 1422, 1363, 1331, and 1211 cm^{-1} for [$VBmim^+$, Cl^-], at 1426, 1348, 1327, and 1224 cm^{-1} for [$VBmim^+$, NTF_2^-], and at 1430, 1340, 1324, and 1212 cm^{-1} for [$VBmim^+$, PF_6^-] [1] [12]. The phenyl ring's (C-C) stretching vibration appear at 1285, 1084 and 1017 cm^{-1} for the [$VBmim^+$, Cl^-], at 1283, 1085 and 1026cm^{-1} for the [$VBmim^+$, PF_6^-] [1]. Furthermore, the, S-N-S, C-F, and O=S=O stretching modes are represented by the distinctive bands of the NTF_2^- anion, which are seen in the range from 1348 to 1052 cm^{-1} [13].

- Region 1000-400 cm^{-1}

Phenyl, imidazolium, and vinyl groups' C-H bending vibration bands are seen in the 700–1000 cm^{-1} range [1] [12]. Likewise, the bands of bending vibration of the NTF_2^- anion and the PF_6^- anion's stretching vibrations are situated within 800-400 cm^{-1}. The bands in the NTF_2^- anion that correspond to the CF_3 symmetric bending are situated between 755 and 735 cm^{-1} [13]. In the 619–510 cm^{-1} range, bending vibrations of δ_{as}(CF3), δ(SO2), and δ(S-N) are detected. The ν(PF_6) stretching vibration modes are detected at 751, 618, 485, and 471 cm^{-1} (weak intensities) and 818 and 551 cm^{-1} (medium and strong intensities) [13].

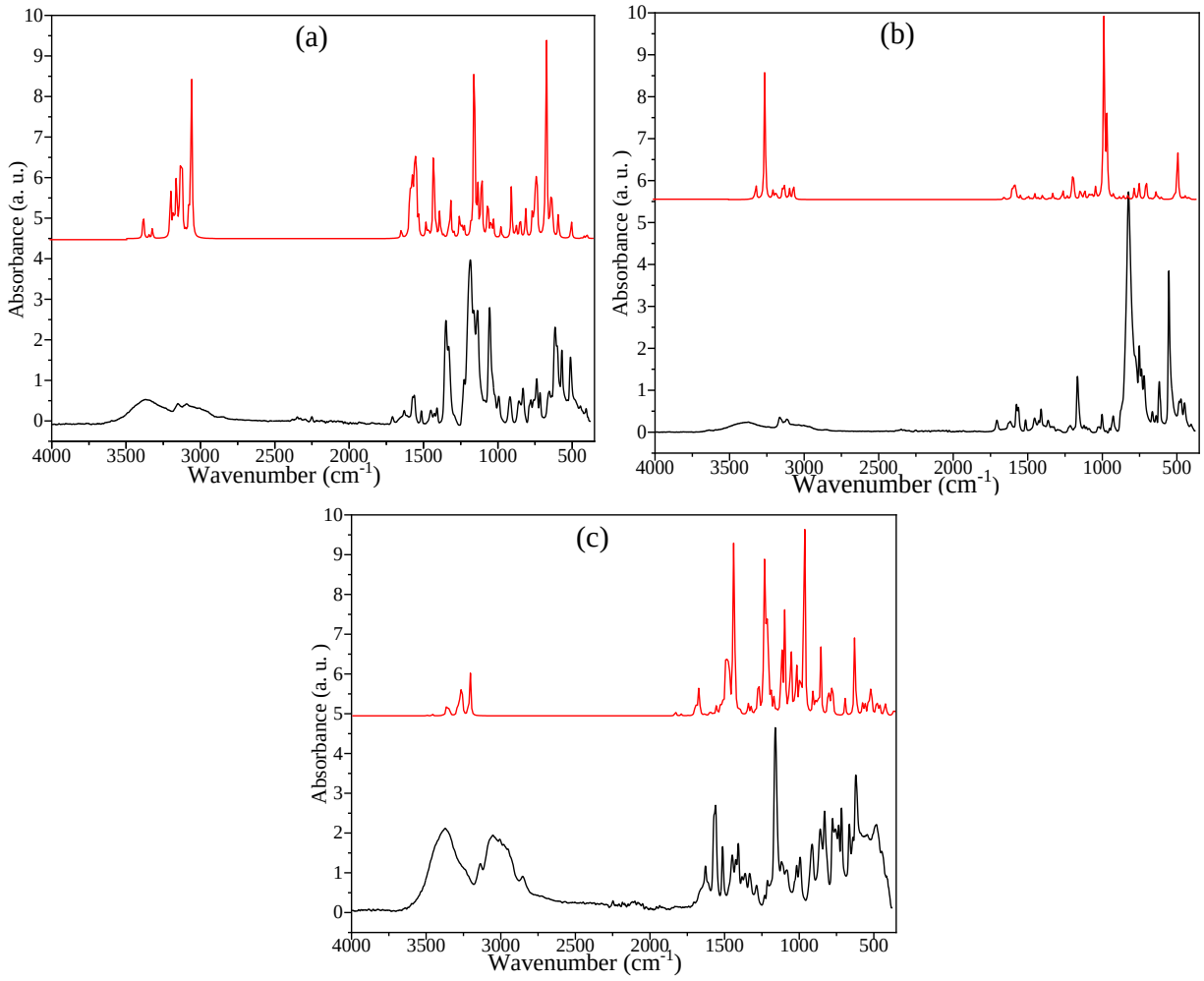

Figure IV. 2. Experimental (black) and theoretical (red) FTIR spectra of the following ILs: (a) [$VBmim^+$, Cl^-], (b) [$VBmim^+$, NTF_2^-], and (c) [$VBmim^+$, PF_6^-].

Table IV. 2: Theoretical and experimental infrared frequencies, with their [$VBmim^+$, Cl^-], [$VBmim^+$, PF_6^-], and [$VBmim^+$, NTF_2^-] assignments.

[$VBmim^+$, Cl^-]		[$VBmim^+$, NTF_2^-]		[$VBmim^+$, PF_6^-]		Assignments	References
Exper	Theor	Exper	Theor	Exper	Theorl		
3368	-	-	-	-	-	adsorbed water' ν (O-H)	[1] [9] [7]
3135	3208	3152	3174	3164	3314	ν (C-H) of imidazole	[1] [9] [7] [8] [10]
3047	3036	3090	3140	3074	3212	ν (C-H) of phenyl	[7] [8]
3038	2970	3011	3083	3036	3185	ν (C-H) of vinyl	[1] [9] [10]

2977	2917	2986	3030	2993	3196	$\nu_{as}(CH_2)$	[1] [10]
2946	2904	2966	3012	2964	3179	ν_s (CH_2)	[1] [9]
2855	2899	2848	2971	2849	3096	ν (C-H) of (CH_3)	[1] [7]
1628	1505	1629	-	1628	1733	ν (C=C) of vinyl	[1] [11] [10]
1610	1559	1610	1559	1616	1653	phenyl ring' ν (C=C)	[1] [11] [10]
-	-	1573	1526	1576	1605	phenyl ring' ν (C=C)	[1]
1560	1523	1562	-	1563	1512	phenyl ring' ν (C=C)	[1]
1514	1505	1515	1501	1513	1471	phenyl ring' ν (C=C), ν (N–C)	[1] [9]
1454	1491	1451	1491	1455	1446	δ (CH_2), $\delta_s CH_3$	[1] [12]
1422	1397	1426	1486	1430	1427	$\delta_s(CH_2)$ν (C=N)/ ν (C=C)/ of imidazole ring	[1] [12]
1407	1387	1410	1481	1411	1399	$\delta_{as}CH_3$, ρ (C-H) of vinyl group	[1] [9] [10]
1382	1339	1387	1484	1378	1343	δ (CH_2) [op]/ P (CH_2), ρ (CH)/ ω (CH), ω (NCH_3)	[13]
1363	1315	1348	1364	1340	1324	Ring imidazol' ν (N=C) / ν (C–C), ν (C=C)/$\nu_{as}(SO_2)$ of trans $[NTF_2]^-$	[1] [12]
1331	1315	1327	1314	1324	1324	N (C–C), ν(C=C)/ν(N=C) of imidazol ring, $\nu_{as}(SO_2)$	[1] [12]
1285	1246	-	1273	1283	1270	phenyl ring' ν(C–C)	[1] [12] [10]
1211	1244	1224	1194	1212	1264	ν (C–C), ν_s(C–F), ν (N–C).	[1] [12] [10]
1154	1188	1180	1184	1167	1207	δ (C-H)	[1] [12] [10]
-	-	1133	1125	-	-	$\nu_s(SO_2)$ of trans $[NTF_2]$	[13]
1106	1117	-	-	1116	1137	δ (C-H), ν (C–C)	[1] [12]
1084	1094	-	-	1085	1123	phenyl'ν (C–C), ρ (C-H).	[1] [12] [10]
-	-	1052	1068	-	-	ν_{as} of (S-N-S)	[13]
1017	1011	-	-	1026	1085	phenyl' ν (C–C)	[1] [12] [10]
990	971	991	1008	1002	1007	vinyl group' ω (C-H)	[1] [12]
913	924	918	913	926	952	vinyl' ω(C-C), δ(C-H) of vinyl out-of-plan,	[1] [5]
858	835	859	903	877	940	imidazol ring' δ (C-H) (in plan)	[1] [11]
829	825	829	862	818	843	C-C bend (ring), $\nu_{as}(PF_6)$, phenyl' ω(C-H)	[13]
777	722	-	-	790	828	ν (C-S), ω (C-H)	[13]
755	706	759	774	751	737	Trans $[NTF_2]$: $\delta_s(CF_3)$, $\nu(PF_6)$, δ (C-H).	[13]
735	706	738	769	737	731	ν (C-N), $\delta_s(CF_3)$,	[13]
715	694	714	729	719	730	imidazol ring' ω (C-H)	[1]
663	646	654	702	664	652	δ(C-H), δ (C-C)	[13]
619	607	613	659	618	591	ν (C–C), ν (PF_6), δ (S-N-S) of trans $[NTF_2]$ phenyl' ν (C–C),)	[13]
-	-	598	653	-	-	δ_{as} (CF_3) of Trans $[NTF_2]$, δ_s (NSO_2), δ ip as(SO_2).	[13]
-	-	570	589	551	542	$\delta_s(NSO_2)$, ν (PF_6), $\delta_{as}(CF_3)$ of Trans $[NTF_2]$, δ ipas(SO_2)	[13]
-	-	510	577	-	-	$\delta_{as}(CF_3)$ of trans $[NTF_2]$, $\delta_s(SO_2)$	[13]
481	556	-	-	485	487	ν (PF_6), ν (C-N),	[13]
-	-	-	-	471	453	ν (PF_6)	[11] [13]
409	474	405	474	403	399	ω (SO_2) of trans-$[NTF_2]$, ν (C–C)	[13]

(ν: asymmetric/symmetric (*as*/*s*) stretching vibration, δ: out of plan bending vibration, ρ: rocking, ω: wagging.)

IV.4 Thermal analysis

The figure IV. 3 (a and b) provides valuable visuals resulting from the application of two independent analysis methods (DSC and ATG), It provides in-depth comprehending of the thermal

properties of the ionic liquids examined in this chapter: [VBmim$^+$, PF_6^-], [VBmim$^+$, Cl^-], and [VBmim$^+$, NTF_2^-]. For all ionic liquids, the dehydration stage is followed by two degradation stages, and the thermograms show a mass loss between 25 and 180 °C as a result of water liberation. The second breakdown stage for [VBmim$^+$, Cl^-] takes place between 200 and 410 °C, whereas the third one takes place between 410 and 600 °C. For the other substances, these decomposition mechanisms are improved. The temperature at which each stage of the decomposition is completed increases in [VBmim$^+$, PF_6^-] and [VBmim$^+$, NTF_2^-], going from 410 to 425°C for the [VBmim$^+$, PF_6^-], and it reaches 470 °C for [VBmim$^+$, NTF_2^-]. This indicates that the anion's nature influences the compound's breakdown. The anion effect on decomposition temperatures and the thermogram shapes show that the three ionic liquids have a tendency to decompose instead of evaporate. All three ionic liquids' glass transition temperature (Tg) was established for the DSC measurements to be close to -15°C for [VBmim$^+$, NTF_2^-], -22°C for [VBmim$^+$, PF_6^-] and -34°C for [VBmim$^+$, Cl^-] [7] [14].

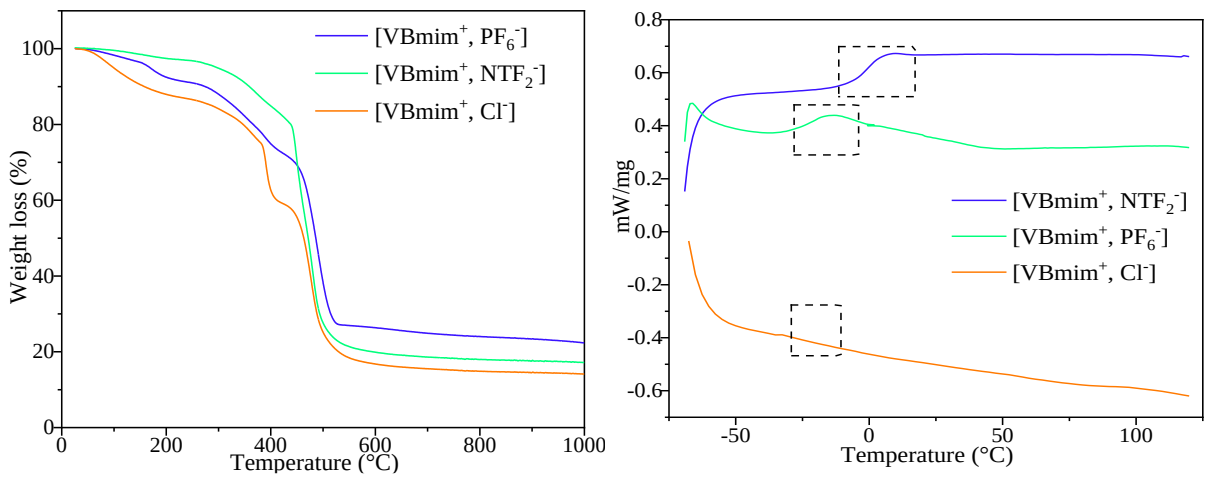

(a) (b)

Figure IV.3. TGA (a) and DSC (b) curves of [VBmim$^+$, PF_6^-] [VBmim$^+$, Cl^-], and [VBmim$^+$, NTF_2^-].

IV.5 Quantum Chemistry results (DFT)

IV.5.1 Molecular orbitals (MOs)

The figure IV. 4 shows the molecular orbitals plots of [VBmim$^+$, Cl^-], [VBmim$^+$, NTF_2^-] and [VBmim$^+$, PF_6^-]. For [VBmim$^+$, Cl^-], it is observed that the electronic density of HOMO is distributed on the imidazole and chlorine moieties, and those of HOMO-1 and HOMO-2 are both distributed on chlorine moiety, for HOMO-3 the electronic density is distributed on aromatic ring and on the vinyl group. While the electronic density of LUMO, LUMO+1, LUMO+2 and LUMO+3 are distributed through the molecule. For [VBmim$^+$, PF_6^-], the HOMO and LUMO are

typically found on the aromatic ring and the vinyl group. The electronic density is distributed on aromatic ring for HOMO-1, imidazole ring, vinyl group and anion moiety for HOMO-2, on other hand the electronic density of LUMO+1, LUMO+2, LUMO+3 and HOMO-3 are almost distributed on cation moiety. For [VBmim$^+$, NTF$_2^-$], the anionic portion NTF$_2^-$ is where the HOMO-1 is primarily found, whereas, the HOMO and HOMO are distributed on the aromatic ring and the vinyl group, while HOMO-2 and HOMO-3 are distributed on the aromatic ring and the anionic part. Furthermore, the LUMO+1 is distributed on imidazole ring, in addition, LUMO+2 and LUMO+3 dispersed across the cationic portion. The process of charge transfer with the external medium involves the coated moieties.

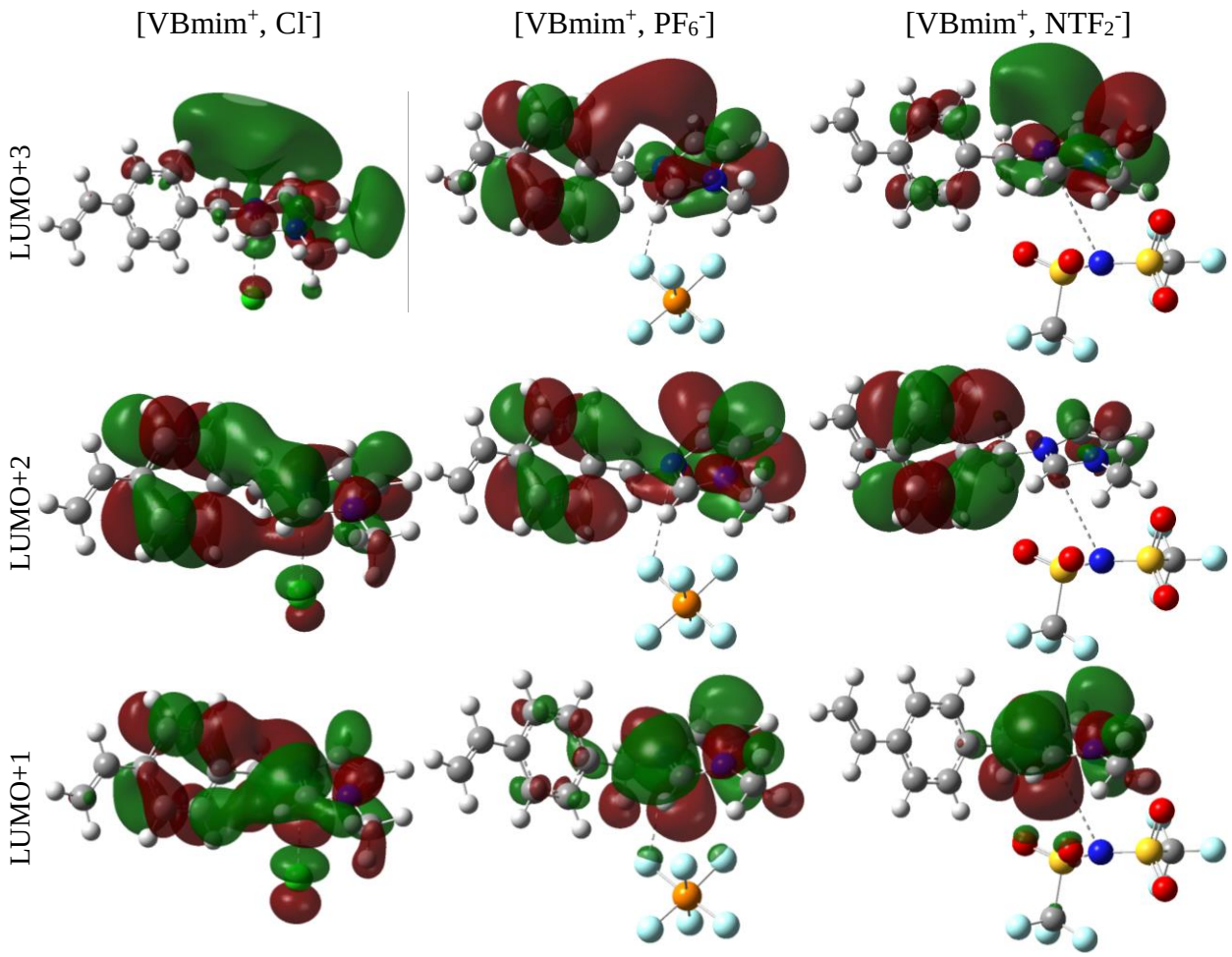

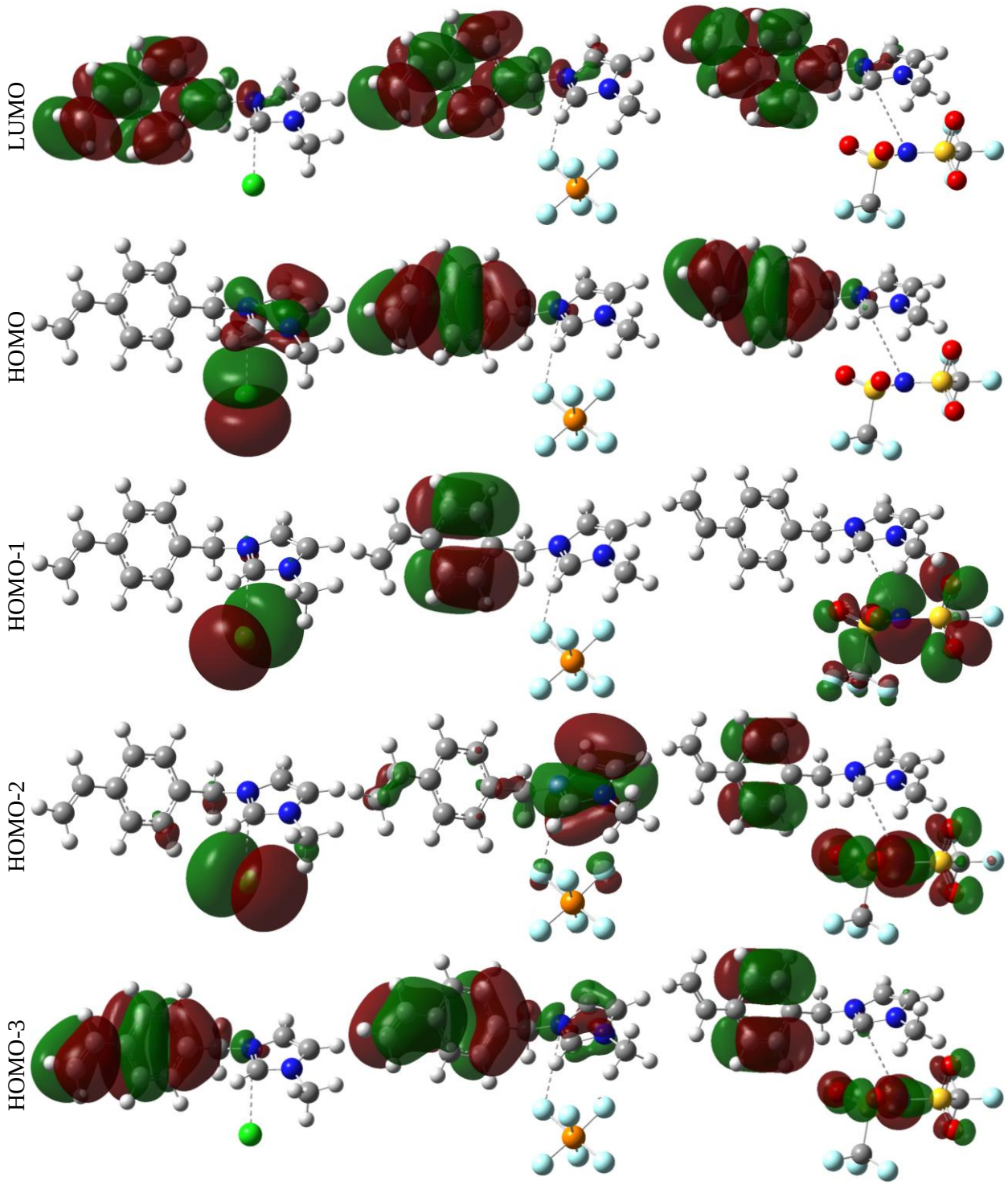

Figure IV. 4. Plots of MOs for [VBmim$^+$, Cl$^-$], [VBmim$^+$, NTF$_2^-$] and [VBmim$^+$, PF$_6^-$].

IV.5.2 Mapping Electrostatic Potential (MEP), partial charges and dipolar moments

Figure IV. 5 (a) shows the surfaces of total electron density plotted with the electrostatic potentials of [VBmim$^+$, PF$_6^-$], [VBmim$^+$, Cl$^-$], and [VBmim$^+$, NTF$_2^-$]. The most geometric zones of the MEP of [VBmim$^+$, Cl$^-$] and [VBmim$^+$, PF$_6^-$] show a positive potential, whereas the anionic

moieties are surrounded by a red-colored negative potential. These sites may receive nucleophilic ions like ions of transition metal [1] [2]. While for the [VBmim$^+$, NTF$_2^-$], the negative potential is centred surrounding the oxygen atoms as well as extends across a vast geometrical zone. [VBmim$^+$, Cl$^-$] has a greater nucleophile potential (-8.01×10^{-2} V) in comparison to [VBmim$^+$, PF$_6^-$] and [VBmim$^+$, NTF$_2^-$], which have -7.36×10^{-2} and -6.36×10^{-2} V, respectively.

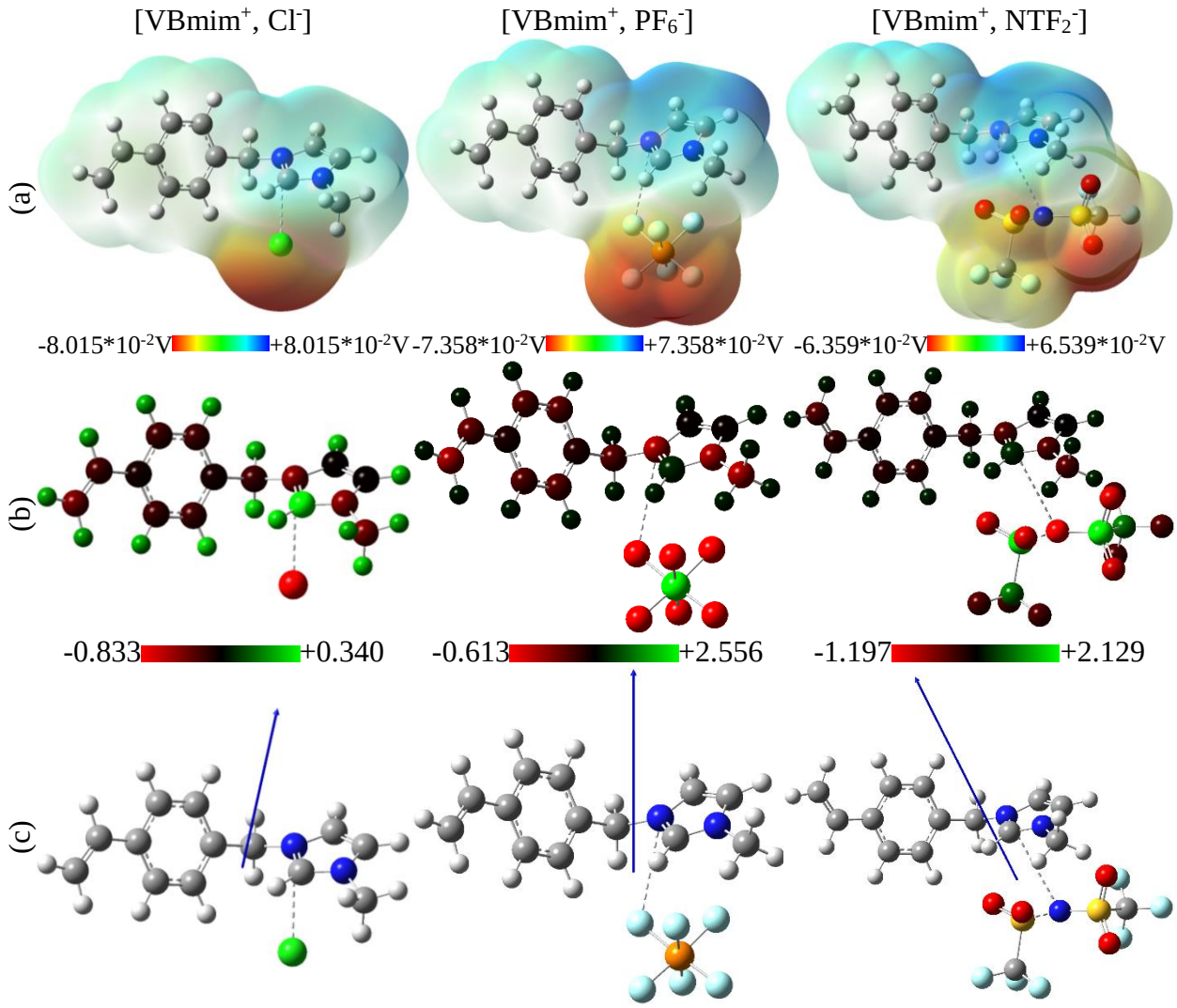

Figure IV. 5. (a): Total electron density surfaces mapped with electrostatic potential, (b): partial charges, and (c) dipolar moments of [VBmim$^+$, PF$_6^-$], [VBmim$^+$, Cl$^-$], and [VBmim$^+$,NTF$_2^-$].

The natural bonding orbitals (NBO) are applied to calculate the partial atomic charge distribution over the structure of molecules: [VBmim$^+$, Cl$^-$], [VBmim$^+$, PF$_6^-$] and [VBmim$^+$, NTF$_2^-$] (Figure IV. 5 (b)). For the [VBmim$^+$, PF$_6^-$] and [VBmim$^+$, NTF$_2^-$] Typically, every hydrogen atom exhibit a net positive charge while the negative charges were found to be located on fluorine, oxygen and azote atoms of cationic parts, in return, the phosphorus and sulphur atoms carry the most positive

partial charge. Furthermore, for [VBmim$^+$, Cl$^-$] the most positive charge is located on C1 atom and the moste negative charge is located on Cl31. Besides, the inhomogeneous distribution of atomic partial charges and the large domain of the electrostatic potential corroborate with high polarity attributed to the high value of dipolar moment, and its Cartesian components. The dipolar moment (Figure IV. 5 (c)) was found to be 8.575, 12.523 and 13.928 Debye for the [VBmim$^+$, Cl$^-$], [VBmim$^+$, NTF$_2^-$] and [VBmim$^+$, PF$_6^-$], respectively. These elevated values align with the non-uniformity of the three ILs' electrostatic potential.

IV.5.3 Reactivity and stability

Electronic HOMO and LUMO energies, along with other quantum chemical descriptors (GQCDs) including gap energy (ΔE), the ionization potential (I), which is the minimum energy required for removing an electron from an atom or molecule. However, the electron affinity (A) describes the change in energy when an electron is added to a neutral atom or molecule. The global hardness (η) refers to the electron cloud polarization or deformation resistance, the opposite is the global softness (σ). The electronegativity (χ) represents an atom's ability to attract electrons in a molecule. The tendency of electrons to escape from an equilibrium system is indicated by the value of chemical potential (μ). The global electrophilicity index(ω) defined as the drop in energy caused by the movement of electrons from the donor HOMO to the acceptor LUMO in the molecule, are all intimately associated with chemical reactivity [15]. These descriptors were computed and the output values are listed in the table IV. 3.

It is clear that changing the anion component has a significant impact on the electrical characteristics of the ILs under study. The energy of the gap for the [VBmim$^+$, Cl$^-$] is 3.83 eV, 4.93 eV for the [VBmim$^+$, PF$_6^-$], while that of the [VBmim$^+$, NTF$_2^-$] is 4.96 eV. The rise of the gap energy indicates stronger relative stability and less reactivity [16]. Additionally, $E_{LUMO's}$ absolute values are low for all ILs under study, these values attribute a receiving character [17], this is once more evident in the high ionization potential (I) and low electron affinity (A) values. However, all ILs have a significant electrophile property, according to the global electrophilicity (ω). Furthermore, the high overall hardness (η) and low softness (σ) values suggest that the molecules are moderately reactive [17].

Table IV. 3. Computed dipolar moments, HOMO and LUMO energies as well as associated global quantum chemical descriptors (GQCDs) for [VBmim$^+$, PF_6^-], [VBmim$^+$, Cl^-], and [VBmim$^+$, NTF_2^-].

		[VBmim$^+$, Cl^-]	[VBmim$^+$, PF_6^-]	[VBmim$^+$, NTF_2^-]
Dipolar moment (Debye)	x	0.149	-7.494	10.192
	y	-7.155	11.619	-7.268
	z	4.724	1.679	.0.0148
	total	8.575	13.928	12.523
Electronic band energies				
E_{total} (keV)		-29.233	-42.310	-66.438
E_{HOMO} (eV)		-5.493	-6.864	-6.996
E_{LUMO} (eV)		-1.660	-1.931	-2.039
Global quantum chemical descriptors				
Gap energy (Δ) (eV)		3.833	4.933	4.957
Ionization potential (I) (eV)		5.493	6.864	6.996
Electron affinity (A) (eV)		1.660	1.931	2.039
Global softness (σ) (eV)		0.522	0.405	0.403
Global hardness (η) (eV)		1.916	2.466	2.478
Global electrophilicity (ω) (eV)		3.337	3.920	4.117
Electronegativity (χ) (eV)		3.576	4.405	4.517
Chemical potential (μ) (eV)		-3.576	-4.397	-4.517

$\Delta = E_{LUMO} - E_{HOMO}$, $I = -E_{HOMO}$, $A = -E_{LUMO}$, $\chi = -[1/2(E_{LUMO} + E_{HOMO})]$, $\eta = 1/2(E_{LUMO} - E_{HOMO})$, $\omega = \chi^2/2\eta$, $\sigma = 1/\eta$, $\mu = [1/2(E_{LUMO} + E_{HOMO})]$.

IV.5.4 Thermal and thermodynamics properties

Some thermodynamic parameters calculated at 298.15 K are collected in the table IV. 4. It can be seen that the vibrational have the highest contribution in the total thermal energy, the entropy and heat capacity of the [VBmim$^+$, Cl^-], [VBmim$^+$, PF_6^-] and [VBmim$^+$, NTF_2^-]. Based on vibrational data, the variation of entropy, heat capacity and enthalpy as a function of temperature were calculated from 150 to 560 K until the stability temperature considered 560 K for all ILs, the results are shown in the figure IV. 6. It has been noted that as the temperature rises, certain thermodynamic functions also rise. In addition, the heat capacities, entropies, enthalpy were fitted by quadratic formulas from (IV. 1) to (IV. 9):

[VBmim$^+$, Cl^-]

S(T)	$280.56 + 1.02T - 2.18\times10^{-4}T^2$	$R^2 = 0.99996$	(IV. 1)
C_p(T)	$018.57 + 0.94T - 3.62\times10^{-4}T^2$	$R^2 = 0.99911$	(IV. 2)
ΔH(T)	$-009.38 + 0.11T + 2.76\times10^{-4}T^2$	$R^2 = 0.99970$	(IV. 3)

[VBmim$^+$, PF_6^-]

S(T)	$307.25 + 1.43T - 3.65\times10^{-4}T^2$	$R^2 = 0.99996$	(IV. 4)
C_p(T)	$033.95 + 1.26T - 5.61\times10^{-4}T^2$	$R^2 = 0.99967$	(IV. 5)
ΔH(T)	$-017.79 + 0.18T + 3.20\times10^{-4}T^2$	$R^2 = 0.99961$	(IV. 6)

[VBmim$^+$, NTF$_2^-$]

S(T)	$365.93 + 1.91T - 5.40\times10^{-4}T^2$	$R^2 = 0.99986$	(IV. 7)
$C_p(T)$	$077.29 + 1.53T - 6.94\times10^{-4}T^2$	$R^2 = 0.99969$	(IV. 8)
$\Delta H(T)$	$-024.05 +0.26T+3.81\times10^{-4}T^2$	$R^2 = 0.99963$	(IV. 9)

Table IV. 4. Thermal parameters of [VBmim$^+$, Cl$^-$], [VBmim$^+$, NTF$_2^-$] and [VBmim$^+$, PF$_6^-$].

[VBmim$^+$, Cl$^-$]			
	E (Thermal)	C_V	S
Total	169.465	058.487	132.396
Electronic	000.000	000.000	000.000
Translational	000.889	002.981	042.253
Rotational	000.889	002.981	033.275
Vibrational	167.688	052.525	059.986
[VBmim$^+$, PF$_6^-$]			
	E (Thermal)	C_V	S
Total	185.379	081.977	167.182
Electronic	000.000	000.000	000.000
Translational	000.889	002.981	043.401
Rotational	000.889	002.981	035.093
Vibrational	183.602	076.016	088.687
[VBmim$^+$, NTF$_2^-$]			
	E (Thermal)	C_V	S
Total	211.932	108.469	211.471
Electronic	000.000	000.000	000.000
Translational	000.889	002.981	044.388
Rotational	000.889	002.981	036.812
Vibrational	210.155	102.507	130.272

Unit of: E (Thermal) (KJ·mol^{-1}),C_v and S (J·mol^{-1}·K^{-1}).

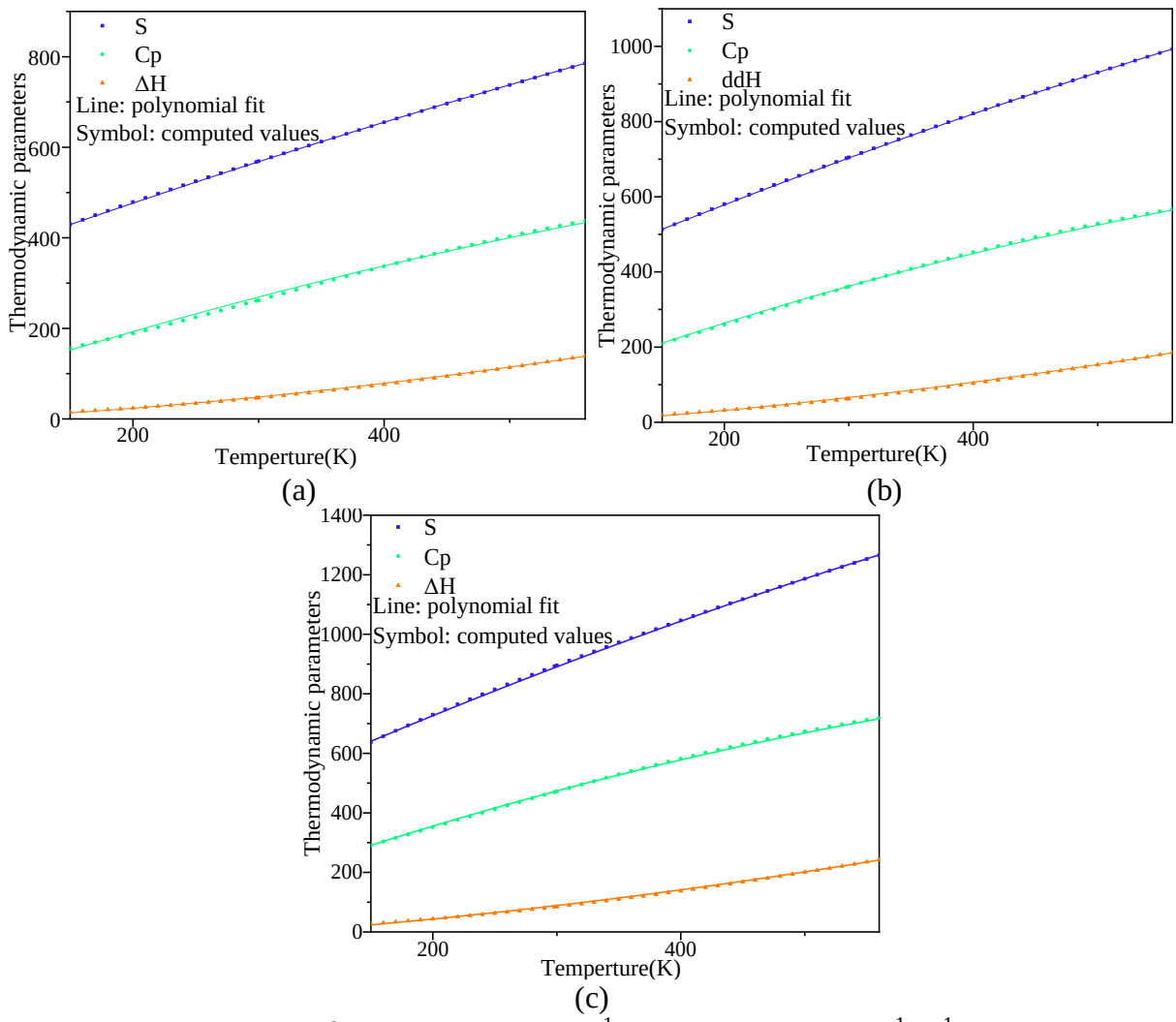

Figure IV. 6. Variation of the enthalpy ($kJ.mol^{-1}$), heat capacity ($J.mol^{-1}.K^{-1}$) and entropy ($J.mol^{-1}.K^{-1}$) as function of temperature for (a): [$VBmim^+$, Cl^-], (b): [$VBmim^+$, PF_6^-] and (c): [$VBmim^+$, NTF_2^-].

IV.5.5 Non-linear optical properties (NLO)

Quantum chemical descriptors like average polarisability ⟨α⟩ and polarisability anisotropy Δα are used in computer studies to describe how an electric field might distort a molecule's electronic cloud. In addition, the nonlinear response of atoms and molecules to a higher-order electric field wave is described by the first order hyper-polarizability β_{tot}. These latter are associated with a wide range of phenomena, from intermolecular interactions to nonlinear optics. In the present work, ⟨α⟩, Δα and β_{tot} were determined using the formulas (IV. 10), (IV. 11) and (IV. 12) [18]:

$$\langle\alpha\rangle = 1/3\ (\alpha_{xx}+\alpha_{yy}+\alpha_{zz}) \qquad \text{(IV. 10)}$$

$$\Delta\alpha = 1/\sqrt{2}[(\alpha_{xx}-\alpha_{yy})^2+(\alpha_{xx}-\alpha_{zz})^2+(\alpha_{yy}-\alpha_{zz})^2+6(\alpha^2_{xy}+\alpha^2_{xz}+\alpha^2_{yz})]^{1/2} \qquad \text{(IV. 11)}$$

$$\beta_{tot}=[(\beta_{xxx}+\beta_{xyy}+\beta_{xzz})^2+(\beta_{yyy}+\beta_{yxx}+\beta_{yzz})^2+(\beta_{zzz}+\beta_{zxx}+\beta_{zyy})^2]^{(1/2)} \quad \text{(IV. 12)}$$

The table IV. 5 lists the calculated values of these parameters using 6-311G++(d, p) basis set. The results are calculted in atomic units (a. u.), and then converted to electrostatic units (esu) (α: 1 a. u.=0.1482×10^{-24} esu; β: 1 a. u.=8.6393×10^{-33} esu).

According to the results, the [$VBmim^+$, NTF_2^-] has the higher linear polarizability and also the higher anisotropy polarizability than [$VBmim^+$, Cl^-] and [$VBmim^+$, PF_6^-]. On the other hand, the [$VBmim^+$, Cl^-] has the high value of the first hyper-polarizability than the other molecules. Moreover, the urea is a model molecule employed as a reference for the NLO features of molecular systems [19]. The table IV. 5 shows that the computed β_{tot} values at B3LYP/ 6-311G++(d, p) level were roughly 8, 5 and 6 times higher than those of the urea, for the [$VBmim^+$, Cl^-], [$VBmim^+$, PF_6^-] and [$VBmim^+$, NTF_2^-] respectively, indicating a non-linear activity of all ILs.

Table IV. 5. Calculated components of polarizability anisotropy (Δα), polarizability (α), and the first order hyper-polarizability (β) of [$VBmim^+$, Cl^-], [$VBmim^+$, PF_6^-] and [$VBmim^+$, NTF_2^-].

	[$VBmim^+$, Cl^-]		[$VBmim^+$, PF_6^-]		[$VBmim^+$, NTF_2^-]	
Units	(a. u.)	(esu)×10^{-24}	(a. u.)	(esu)×10^{-24}	(a. u.)	(esu)×10^{-24}
α_{xx}	248.588	36.841	224.570	33.281	335.962	49.790
α_{yy}	195.524	28.977	209.077	30.985	243.927	36.150
α_{zz}	144.826	21.463	152.589	22.614	201.934	29.927
$\langle\alpha\rangle$	196.313	29.093	195.412	28.960	260.608	38.622
$\Delta\alpha$	99.707	14.777	98.678	14.624	128.811	19.090
Units	(a. u.)	(esu)×10^{-30}	(a. u.)	(esu)×10^{-30}	(a. u.)	(esu)×10^{-30}
β_{xxx}	27.728	0.239	100.559	0.869	127.687	1.103
β_{xxy}	-8.541	-0.0738	201.419	1.740	-185.301	-1.601
β_{xyy}	82.671	0.714	-44.489	-3.843	115.110	0.994
β_{yyy}	-414.338	-3.580	146.462	1.265	-165.878	-1.433
β_{xxz}	-18.280	-0.158	-78.078	-6.745	-2.971	-0.026
β_{xyz}	15.588	0.135	-17.104	-1.478	16.449	0.142
β_{yyz}	235.989	2.039	31.224	2.697	15.520	0.134
β_{xzz}	-11.888	-0.103	-43.317	-3.742	83.654	0.723
β_{yzz}	-164.167	-1.418	58.765	5.077	-70.040	-0.605
β_{zzz}	126.294	1.091	23.921	2.067	28.499	0.246
β_{tot}	687.506	5.940	407.492	3.520	534.491	4.618
β_{tot}/β_{urea}	7.606		4.507		5.913	
β_{urea}			0.781×10^{-30}esu			

IV.5.6 Optical properties

The figure IV. 7 shows the UV-Visible calculated spectra of the studied ionic liquids. All of absorbance spectra illustrate that the studied ionic liquids are transparent in the visible domain, while, they have three-overlapped absorbance sub bands of UV light. For [VBmim$^+$, Cl$^-$] the first at 326 nm corresponds to electronic transitions from HOMO-1 to LUMO, LUMO+1, LUMO+2 and LUMO+3, this sub band has an oscillator strength f=7×10^{-4}. The second sub band at 322 nm is related to the electronic transitions from HOMO-2 to LUMO, LUMO+1, LUMO+2 and LUMO+3, this electronic transitions has an oscillator strength f=4×10^{-4}, the third band at 313 nm relates to electronic transition from HOMO to LUMO (f=1.28×10^{-2}). For [VBmim$^+$, PF_6^-] the first at 243 nm corresponds to electronic transition from HOMO to LUMO, this sub band has an oscillator strength f=1.2×10^{-3}. The second sub band at 237 nm is related to the electronic transitions from HOMO to LUMO+1 and from HOMO to LUMO, LUMO+2, LUMO+3 and LUMO+4, this electronic transitions has an oscillator strength f=4×10^{-4}, the third band at 229 nm is due to the electronic transition from HOMO-1 to LUMO (f=1.3×10^{-3}). For the [VBmim$^+$, NTF_2^-] the first sub band at 242 nm is related to HOMO, LUMO electronic transition with an oscillator strength f=1.5×10^{-3}. The second at 237 nm corresponds to electronic transition from HOMO-2 to LUMO+1 and LUMO+2 and from HOMO-1 to LUMO+1 and LUMO+2, this sub band has an oscillator strength f=1.7×10^{-3}. The third one at 237 nm corresponds to HOMO-1, LUMO electronic transition, this sub band has an oscillator strength f=3×10^{-3}. The table IV. 6 summarizes the electronic transition assignments, oscillator strength and gap energy values characteristic of the [VBmim$^+$, Cl$^-$], [VBmim$^+$, PF_6^-] and [VBmim$^+$, NTF_2^-].

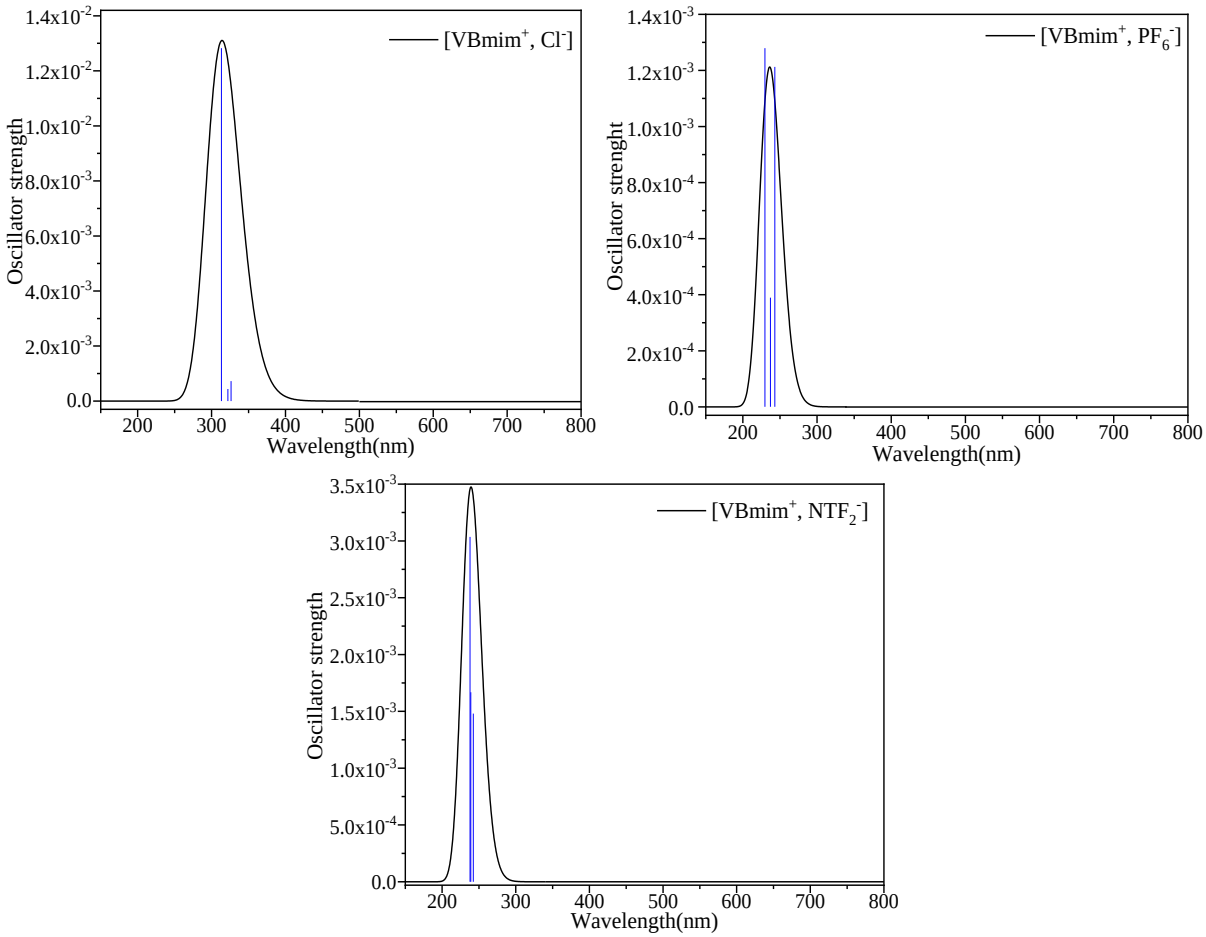

Figure IV. 7. UV-Visible absorption spectra and oscillator strength of [VBmim$^+$, Cl$^-$], [VBmim$^+$, PF$_6^-$] and [VBmim$^+$, NTF$_2^-$].

Table IV. 6. Electronic transition assignments, their corresponding energies, gap energy and oscillator strength values characteristic of the [VBmim$^+$, Cl$^-$], [VBmim$^+$, PF$_6^-$] and [VBmim$^+$, NTF$_2^-$].

λ (nm)	Electronic transition	Oscillator strength (f)	E (eV)
	[VBmim$^+$, Cl$^-$]		
326.31	HOMO-1→LUMO HOMO-1→LUMO+1 HOMO-1→LUMO+2 HOMO-1→LUMO+3	7×10^{-4}	3.80
322.04	HOMO-2→LUMO HOMO-2→LUMO+1 HOMO-2→LUMO+2 HOMO-2→LUMO+3	4×10^{-4}	3.85
313.29	HOMO→LUMO	1.28×10^{-2}	3.96
	[VBmim$^+$, PF$_6^-$]		
243.01	HOMO-1→LUMO+1 HOMO→LUMO HOMO→LUMO+2	1.2×10^{-3}	5.10

	HOMO→LUMO+3 HOMO-1→LUMO+1 HOMO→LUMO		
237.13	HOMO→LUMO+2 HOMO→LUMO+3 HOMO→LUMO+4	4×10^{-4}	5.23
229.76	HOMO-1→LUMO	1.3×10^{-3}	5.40
	[VBmim$^+$, NTF$_2^-$]		
242.31	HOMO→LUMO	1.5×10^{-3}	5.12
238.96	HOMO-2→LUMO+1 HOMO-2→LUMO+2 HOMO-1→LUMO+1	1.7×10^{-3}	5.19
237.94	HOMO-1→LUMO+2 HOMO-1→LUMO	3×10^{-3}	5.21

IV.6 Conclusion

Both experimental and theoretical methods were employed to study the [VBmim$^+$, Cl$^-$], [VBmim$^+$, PF$_6^-$] and [VBmim$^+$, NTF$_2^-$] imidazolium based ionic liquids. Firstly, the molecular structures were optimized using the DFT with B3LYP functional and 6-311G++ (d, p) basis sets. Afterward, the corresponding theoretical FT-IR spectra were compared to the experimental ones, and the various vibration bands were all assigned. In addition, the [VBmim$^+$, Cl$^-$], [VBmim$^+$, PF$_6^-$] and [VBmim$^+$, NTF$_2^-$] exhibit a thermal stability around 270 °C, noting that the anion nature influence the degradation behaviour. Using DFT-theoretical calculations we were able to predict: the molecular orbitals, mapping electrostatic potential, partial charges, dipolar moment and some global quantum chemical descriptors, founding that all ILs exhibit a high value of dipolar moment. According to the GQCDs results, all Ils are hard, kinetic stable and low chemical reactive, and have an acceptor character. From the vibrational data, the heat capacity, entropy, and enthalpy were calculated, and found to increase with the increase of temperature, ranging from 150 to 560 K. The study was extended to analyse the nonlinear optical properties of [VBmim$^+$, Cl$^-$], [VBmim$^+$, PF$_6^-$] and [VBmim$^+$, NTF$_2^-$], the polarizability is highest for [VBmim$^+$, NTF$_2^-$], showing that it has a higher average response to an external electric field, $\Delta\alpha$ also follows this trend, indicating increased anisotropy in the polarizability tensor for [VBmim$^+$, NTF$_2^-$]. β_{tot} is highest for [VBmim$^+$, Cl$^-$], indicating its strong nonlinear optical activity compared to the other ILs. Normalizing β_{tot} with respect to urea, shows that these ionic liquids possess significantly higher hyperpolarizabilities, particularly [VBmim$^+$, Cl$^-$]. From the TD-DFT, all ILs have a total

transmission in the visible domain while, they have three-overlapped absorbance sub bands in UV one.

IV.7 References

[1] M. Belhocine, R. Bourzami, F. Dergal, A. Ammari, Z. Benladghem, A. Haouzi and S. Bouktab, "Physical, chemical and antibacterial properties of 1-methyl-3-(4-vinylbenzyl) imidazol-3-ium chloride ionic liquid: Experimental and ab-initio analysis," *Journal of Molecular Structure*, vol. 1271, p. 133955, Jan. 2023, doi: 10.1016/j.molstruc.2022.133955.

[2] M. Belhocine, R. Bourzami, F. Dergal, A. Ammari, Z. Benladghem, A. Haouzi, F. Hoppenot and S. Bouktab, "Physical, chemical and antibacterial properties of benzethonium chloride: Experimental and ab-initio analysis," *Journal of Molecular Structure*, vol. 1293, p. 136299, Dec. 2023, doi: 10.1016/j.molstruc.2023.136299.

[3] Y. Bellal, S. Keraghel, F. Benghanem, G. Sigircik, R. Bourzami, A. Ourari, "A New Inhibitor for Steel Rebar Corrosion in Concrete: Electrochemical and Theoretical Studies," *International Journal of Electrochemical Science*, vol. 13, no. 7, pp. 7218–7245, Jul. 2018, doi: 10.20964/2018.07.91.

[4] N. Stanley, V. Sethuraman, P. T. Muthiah, P. Luger, and M. Weber, "Crystal Engineering of Organic Salts: Hydrogen-Bonded Supramolecular Motifs in Pyrimethamine Hydrogen Glutarate and Pyrimethamine Formate," *Crystal Growth & Design*, vol. 2, no. 6, pp. 631–635, Nov. 2002, doi: 10.1021/cg020027p.

[5] Z. Fellahi, H. C. Ait Youcef, D. Hannachi, A. Djedouani, L. Ouksel, M. François, S. Fleutot, R. Bourzami, "Synthesis, X-ray crystallography, Hirshfeld surface analysis, thermal properties and DFT/TD-DFT calculations of a new material hybrid ionic (C10H18N2O82+.2ClO4−.4H2O)," *Journal of Molecular Structure*, vol. 1244, p. 130955, Nov. 2021, doi: 10.1016/j.molstruc.2021.130955.

[6] R. Bourzami, H. C. AitYoucef, N. Hamdouni, and M. Sebais, "Synthesis, crystal structure, vibrational spectra and thermal properties of novel ionic organic-inorganic hybrid material," *Chemical Physics Letters*, vol. 711, pp. 220–226, Nov. 2018, doi: 10.1016/j.cplett.2018.08.002.

[7] M. Belhocine, A. Ammari, A. Haouzi, F. Dergal, M. Debdab, and H. Belarbi, "Intercalation effect of 1-methyl-3-(4-vinylbenzyl) imidazol-3-ium chloride ionic liquid on Na-exchanged montmorillonite: Synthesis, characterizations, and dielectric spectroscopic analysis," *Journal of Physics and Chemistry of Solids*, vol. 169, p. 110846, Oct. 2022, doi: 10.1016/j.jpcs.2022.110846.

[8] Y. Chaker, H. Ilikti, M. Debdab, T. Moumene, E. H. Belarbi, A. Wadouachi, O. Abbas, B. Khelifa and S. Bresson, "Synthesis and characterization of 1-(hydroxyethyl)-3-methylimidazolium

sulfate and chloride ionic liquids," *Journal of Molecular Structure*, vol. 1113, pp. 182–190, Jun. 2016, doi: 10.1016/j.molstruc.2016.02.017.

[9] E. Rynkowska, K. Dzieszkowski, A. Lancien, K. Fatyeyeva, A. Szymczyk, J. Kujawa, S. Koter, S. Marais, A. Wolan and W. Kujawski, "Physicochemical properties and pervaporation performance of dense membranes based on cellulose acetate propionate (CAP) and containing polymerizable ionic liquid (PIL)," *Journal of Membrane Science*, vol. 544, pp. 243–251, Dec. 2017, doi: 10.1016/j.memsci.2017.09.031.

[10] K. Malek, A. Puc, G. Schroeder, V. I. Rybachenko, and L. M. Proniewicz, "FT-IR and FT-Raman spectroscopies and DFT modelling of benzimidazolium salts," *Chemical Physics*, vol. 327, no. 2–3, pp. 439–451, Sep. 2006, doi: 10.1016/j.chemphys.2006.05.021.

[11] M. Boumediene, B. Haddad, A. Paolone, M. Drai, D. Villemin, M. Rahmouni, S. Bresson and O. Abbas, "Synthesis, thermal stability, vibrational spectra and conformational studies of novel dicationic meta-xylyl linked bis-1-methylimidazolium ionic liquids," *Journal of Molecular Structure*, vol. 1186, pp. 68–79, Jun. 2019, doi: 10.1016/j.molstruc.2019.03.019.

[12] D. Hadji, B. Haddad, S. A. Brandán, S. K. Panja, A. Paolone, M. Drai, D. Villemin, S. Bresson and M. Rahmouni, "Synthesis, NMR, Raman, thermal and nonlinear optical properties of dicationic ionic liquids from experimental and theoretical studies," *Journal of Molecular Structure*, vol. 1220, p. 128713, Nov. 2020, doi: 10.1016/j.molstruc.2020.128713.

[13] M. Boumediene, B. Haddad, A. Paolone, M. A. Assenine, D. Villemin, M. Rahmouni and S. Bresson, "Synthesis, conformational studies, vibrational spectra and thermal properties, of new 1,4-(phenylenebis(methylene) bis(methyl-imidazolium) ionic liquids," *Journal of Molecular Structure*, vol. 1220, p. 128731, Nov. 2020, doi: 10.1016/j.molstruc.2020.128731.

[14] B. Brunetti, A. Ciccioli, G. Gigli, A. Lapi, G. Simonetti and E. Toto, "Evaporation/Decomposition Behavior of 1-Butyl-3-Methylimidazolium Chloride (BMImCL) Investigated through Effusion and Thermal Analysis Techniques," *Thermo*, vol. 3, no. 2, pp. 248–259, Apr. 2023, doi: 10.3390/thermo3020015.

[15] S. Majumder, S. Hazra, S. Dutta, P. Biswas, and S. Mohanta, "Syntheses, structures and electrochemistry of manganese(III) complexes derived from N,N′-o-phenylenebis(3-ethoxysalicylaldimine): Efficient catalyst for styrene epoxidation," *Polyhedron*, vol. 28, no. 12, pp. 2473–2479, Aug. 2009, doi: 10.1016/j.poly.2009.04.034.

[16] R. Kannappan, S. Tanase, I. Mutikainen, U. Turpeinen, and J. Reedijk, "Low-spin iron(III) Schiff-base complexes with symmetric hexadentate ligands: Synthesis, crystal structure,

spectroscopic and magnetic properties," *Polyhedron*, vol. 25, no. 7, pp. 1646–1654, May 2006, doi: 10.1016/j.poly.2005.11.005.

[17] E. E. Ebenso, D. A. Isabirye, and N. O. Eddy, "Adsorption and Quantum Chemical Studies on the Inhibition Potentials of Some Thiosemicarbazides for the Corrosion of Mild Steel in Acidic Medium," *IJMS*, vol. 11, no. 6, pp. 2473–2498, Jun. 2010, doi: 10.3390/ijms11062473.

[18] S. Guidara, A. B. Ahmed, Y. Abid, and H. Feki, "Molecular structure, vibrational spectra and nonlinear optical properties of 2,5-dimethylanilinium chloride monohydrate: A density functional theory approach," *Spectrochimica Acta Part A: Molecular and Biomolecular Spectroscopy*, vol. 127, pp. 275–285, Jun. 2014, doi: 10.1016/j.saa.2014.02.028.

[19] A. Eşme and S. Sagdinc, "The linear, nonlinear optical properties and quantum chemical parameters of some sudan dyes," Jun. 2016. Accessed: Feb. 11, 2024. [Online]. Available: https://www.semanticscholar.org/paper/The-linear%2C-nonlinear-optical-properties-and-of-E%C5%9Fme-Sagdinc/bffb4897b72d155eefb0a9322cd0ff62afb7f42f

Corrosion inhibition and carbon paste electrodes elaboration applications

V. Corrosion inhibition and carbon paste electrodes elaboration applications

V.1 Corrosion inhibition

The first topic we did in this chapter was to study the effectiveness of DH4MPMP and H4MPMPA ester and acid phosphonates molecules as inhibitors of XC48 corrosion when exposed to hydrochloric acid. A number of methods were employed, including weight loss measurements, electrochemical impedance spectroscopy (EIS), and the Tafel polarization curve approach. We also investigated the surface with atomic force microscopy (AFM). The simulation of the interface configuration between the phosphonates molecules and the steel surface using molecular dynamic simulation. Organic corrosion inhibitors, while effective; often have limitation [1] due to cost; toxicity and negative effects on the environment. It is important to mention other effective systems that are revealed to be safe and environmental friendly inhibitors of the steel corrosion in different media [2]. For this reason, the second topic is the study of the effectiveness of the ionic materials $C_3H_8N_6^{2+}.2ClO_4^-.H_2O$ and [$VBmim^+$, Cl^-] at preventing XC48 corrosion when exposed to hydrochloric acid using weight loss measurements and investigate the surface with atomic force microscopy (AFM).

V.1.1 Weight loss measurements

V.1.1.1 Organic molecules

The table V. 1 shows that the corrosion rate decreases by increasing the concentration of DH4MPMP or H4MPMPA in the 1M solution of HCl; consequently, the inhibitory efficiency increases and reaches the maximum value (91 and 93 respectively) at 0.4 mM. The latter also shows the effect of temperature on the behavior of steel in the acid solution. As the temperature of the aggressive solution rises from 298 to 328 K, we observe that the corrosion rate rises as well from 0.155 to 0.95 $mg.h^{-1}.mm^{-2}$ for the DH4MPMP and from 0.12 to 0.71 $mg.h^{-1}.mm^{-2}$ for the H4MPMPA.

Table V. 1. Corrosion rate and inhibition efficiency of DH4MPM and H4MPMPA vs concentrations in acidic medium.

Concentrations (mM)	T = 298 K			T = 328 K		
	Θ	CR ($mg.h^{-1}.cm^{-2}$)	EI_w (%)	θ	CR ($mg.h^{-1}.cm^{-2}$)	EI_w (%)
	DH4MPMP					
0.0	-	1.720	-	-	5.93	-
0.1	0.77	0.395	77	0.70	1.78	70
0.2	0.83	0.292	83	0.76	1.42	76
0.3	0.85	0.258	85	0.78	1.30	78
0.4	0.91	0.155	91	0.84	0.95	84
	H4MPMPA					
0.0	-	1.720	-	-	5.93	-
0.1	0.78	0.378	78	0.74	1.54	74
0.2	0.86	0.241	86	0.80	1.19	80
0.3	0.88	0.206	88	0.83	1.01	83
0.4	0.93	0.120	93	0.88	0.71	88

V.1.1.2 Ionic material

V.1.1.2.1 Ionic organic-inorganic hybrid material

The table V. 2 presents the results of the gravimetric tests of the XC48 carbon steel in 1M of HCl solution in presence and in absence of the various concentrations of the 2,4,6-triamino-1,3,5-triazin-1,3-dium bisperchlorate monohydrate. It shows a decrease in the corrosion rate and increase in the inhibition efficiency with an increase of the inhibitor concentration. The inhibition efficiency reached the maximum of 95 % in presence of 2,4,6-triamino-1,3,5-triazin-1,3-dium bisperchlorate monohydrate hybrid material. This finding indicates that adding the inhibitor to the corrosive solution lowers carbon steel corrosion.

Table V. 2. Corrosion rate and inhibition efficiency of 2,4,6-triamino-1,3,5-triazin-1,3-dium bisperchlorate monohydrate vs concentrations in acidic medium.

Concentration (mol/L)	CR (mmy)	IEw (%)	θ
0	77.43	/	/
10^{-4}	3.83	95.00	0.95
0.5×10^{-4}	3.64	95.30	0.95
10^{-5}	4.67	93.96	0.94
0.5×10^{-5}	4.26	93.50	0.93

V.1.1.2.2 Ionic liquid

The table V. 3 presents the results of the weight loss measurements of the XC48 carbon steel in 1M of HCl solution in presence and in absence of the various concentrations of the

[VBmim$^+$, Cl$^-$], it shows a decrease in the corrosion rate and increase in the inhibition efficiency with an increase of the inhibitor concentration. The inhibition efficiency reached the maximum of 97 % in presence of [VBmim$^+$, Cl$^-$]. This result indicates that the adding of the inhibitor into the corrosive solution reduces the corrosion of the carbon steel may be by the formation of a protective film on the metal surface.

Table V. 3. Corrosion rate and inhibition efficiency of [VBmim$^+$, Cl$^-$] vs concentrations in acidic medium.

Concentration (mol/L)	CR (mm.y)	IE_W (%)	θ
0	77.43	/	/
10^{-4}	4.33	94.41	0.944
10^{-6}	1.67	97.85	0.978

V.1.2 Atomic Force Microscopy

V.1.2.1 Organic molecules

The AFM images of XC48 surface before and after 24 h of immersion in acidic solution without and with the presence of the studied inhibitors are showed in the figure V. 1.

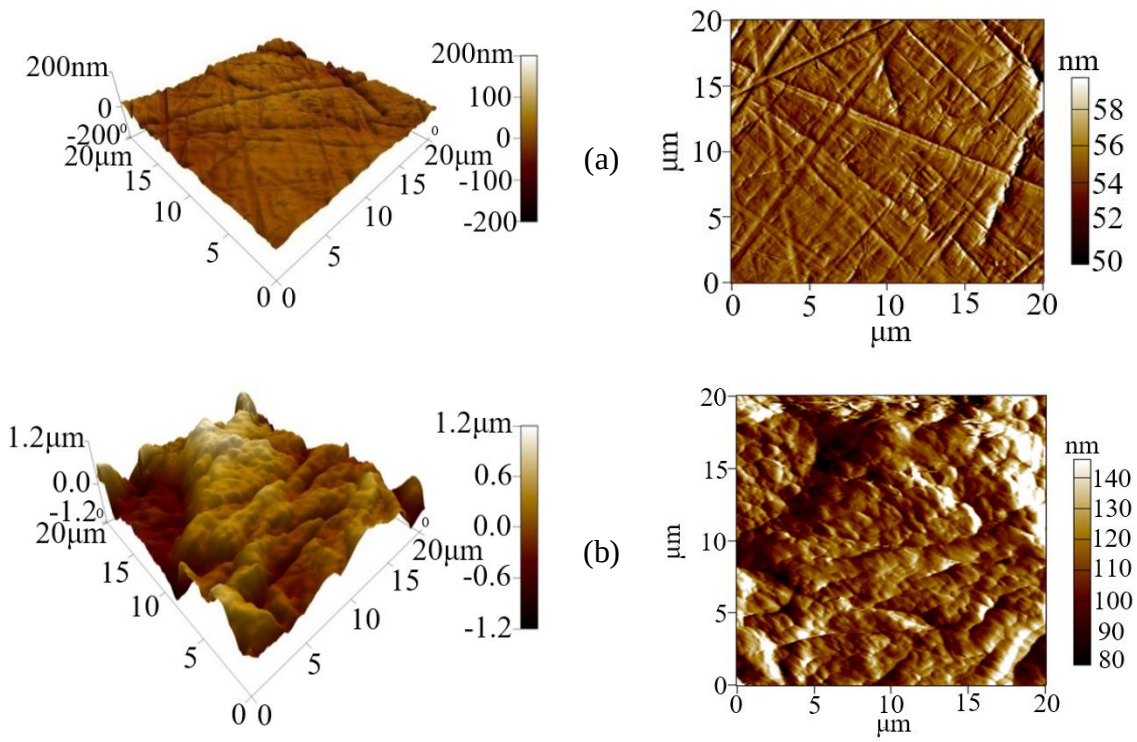

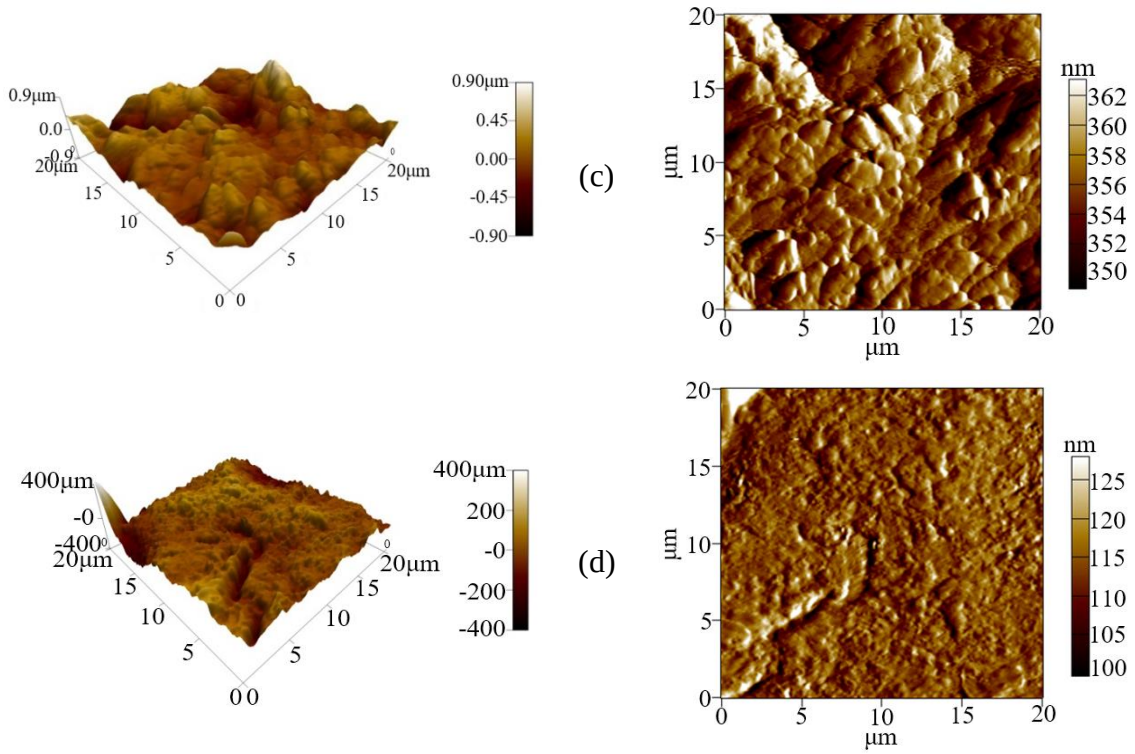

Figure V. 1. AFM images of the XC48 steel surface, (a) Before immersion, (b) after 24 h immersion in HCl, (c) After 24 h immersion in HCl /0.4 mM DH4MPMP, (d) After 24 h immersion in HCl /0.4 mM H4MPMPA.

The table V. 4 provides an overview of the roughness of XC48 steel after immersion in acidic solution with and without inhibitors. Although, the average roughness of the corroded XC48 steel (360.5 nm) was larger than the polished one (15.8 nm), this parameter was decreased in the presence of DH4MPMP or H4MPMPA to 169.78 and 60.70 nm respectively. These findings show that the acid damages the steel surface while the molecules of the adsorbed inhibitors slow corrosion and surface deterioration. Finally, it can be concluded that the AFM supports the findings of the weight loss measurements.

Table V. 4. Surface roughness of XC48 steel in the presence and absence of DH4MPMP and H4MPMPA.

XC48 steel surface	Roughness (nm)
Polished	015.80
Immersed in acidic solution	360.50
Immersed in acidic solution/DH4MPMP (0.4 mM)	169.78
Immersed in acidic solution/H4MPMPA (0.4 mM)	060.70

V.1.2.2 Ionic material

V.1.2.2.1 Ionic organic-inorganic hybrid material

It can be seen visually that in the presence of the 2,4,6-triamino-1,3,5-triazin-1,3-dium bisperchlorate monohydrate that the surfaces are less rigorous (Figure V. 2). The values of the peak to valley are 0.254 and 0.284 µm, while the RMS values are 0.726 and 0.330 µm for the pieces without and with 2,4,6-triamino-1,3,5-triazin-1,3-dium bisperchlorate monohydrate inhibitor.

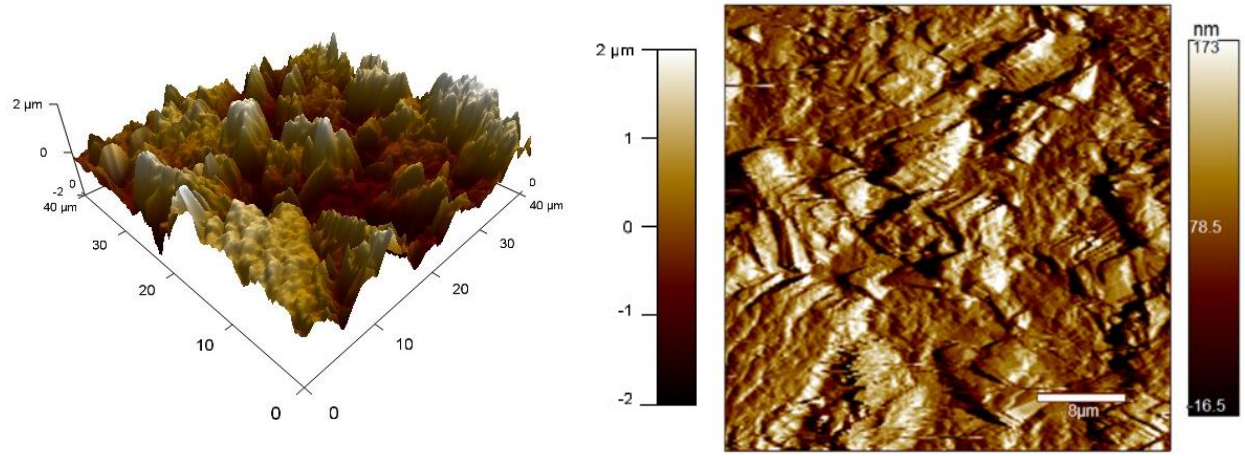

Without inhibitor

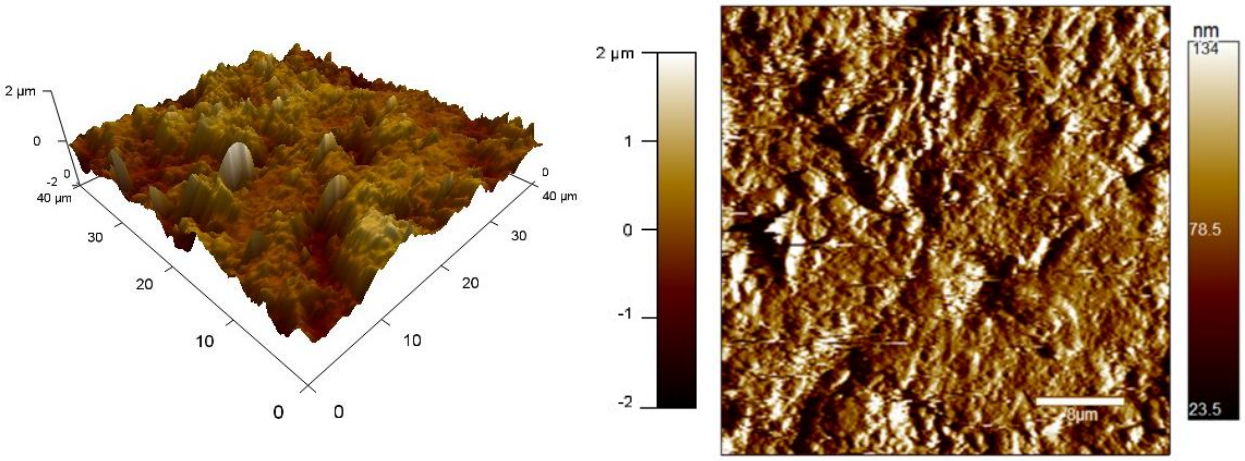

With inhibitor

Figure V. 2. AFM images of the XC48 steel surface, immersion in 1M HCl solution without with the 2,4,6-triamino-1,3,5-triazin-1,3-dium bisperchlorate monohydrate inhibitor.

V.1.2.2.2 Ionic liquid

Figure V. 3 represents the morphologies of the XC48 steel after 6 h of immersion in acidic solution without and with the presence of 10^{-6} M [$VBmim^{+}$, Cl^{-}] inhibitor . It is clearly seen that

in the presence of the inhibitor the surfaces are less rough. The values of the peak to valley are 0.254 and 0.137 µm, while the RMS values are 0.726 and 0.148 µm for the pieces without and with [VBmim$^+$, Cl$^-$] inhibitor.

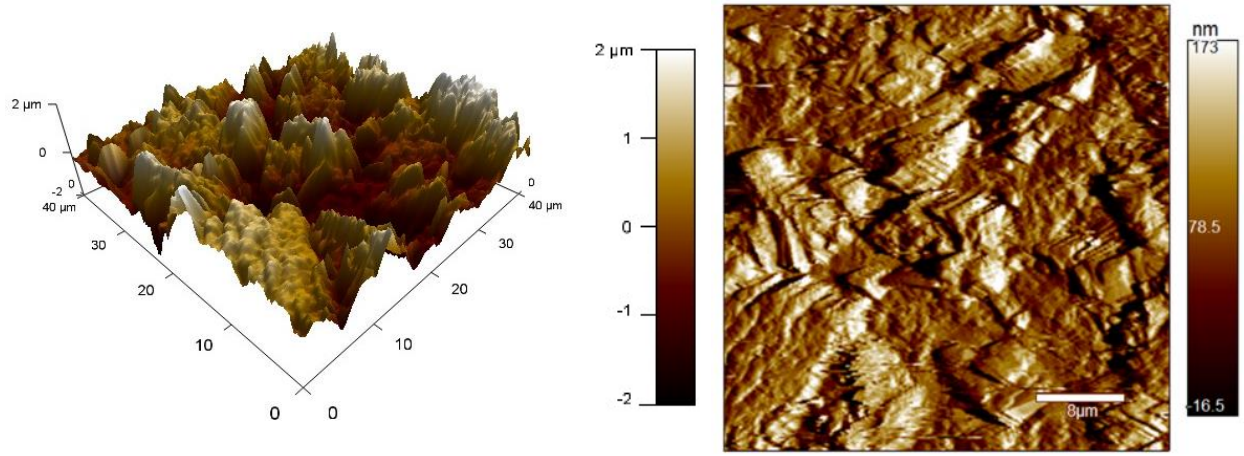

Without inhibitor

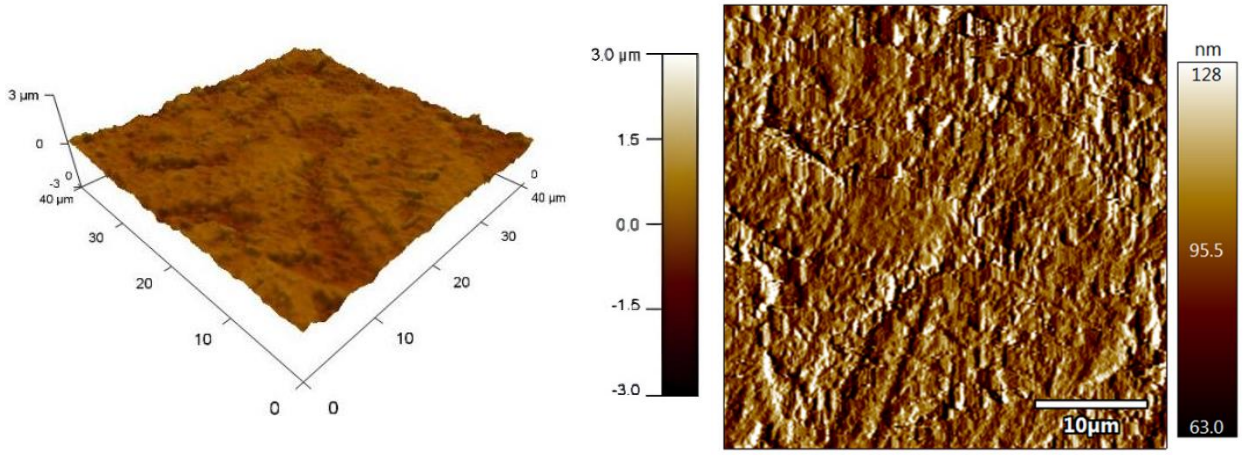

With inhibitor

Figure V. 3. AFM images of the XC48 steel surface, immersion in 1M HCl solution without with the [VBmim$^+$, Cl$^-$] inhibitor.

V.1.3 Electrochemical results

This paragraph summarizes the electrochemical results obtained for the two phosphonates molecules (DH4MPMP and H4MPMPA), other similar and comparative investigation are always in progress on the ionic materials, and they will be published in future works.

V.1.3.1 Polarization studies

The Tafel curves established for XC48 steel in 1M of HCl solution, without and with different concentrations of DH4MPMP or H4MPMPA are presented in the figure V. 4. It can be

observed that, the addition of DH4MPMP or H4MPMPA to the aggressive solution shifts the cathodic and anodic branches of the polarization curves towards the lowest current values, this behaviour demonstrates that mixed cathodic and anodic processes control the inhibition corrosion. The corrosion parameters drawn from the polarization curves are given in the table V. 5, the corrosion current density i_{corr} decreases significantly in the presence of DH4MPMP (28,22 µA/cm^2) or H4MPMPA (13 µA/cm^2) and the inhibition efficiency increases and reaches maximum value of 83 and 92 % at a concentration of 0.4mM of DH4MPMP and H4MPMPA respectively. These values are the same order than those found for good inhibitors [3] [4].

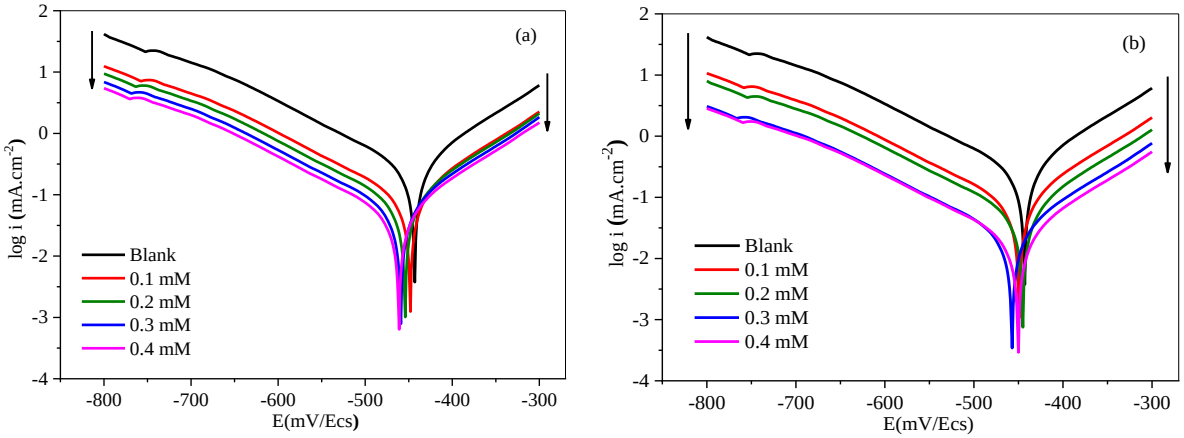

Figure V. 4. Tafel curves of XC48 steel obtained at 293 K in HCl 1N solution for various concentrations of (a) DH4MPMP and (b) H4MPMPA.

Table V. 5. Electrochemical parameters derived from Tafel curves.

C	E_{corr}	i_{corr}	$ß_a$	$ß_C$	IE_p
Blank	-443	166	66,8	-92	-
0.1	-448	54.78	65.1	-91	67
0.2	-454	44.82	63.9	-89	73
0.3	-459	34.86	60.1	-87	79
0.4	-461	28.22	58.3	-86	83
Blank	-443	166	66.8	-92	-
0.1	-449	48.1	65.3	-90	71
0.2	-445	33.2	63.7	-89	80
0.3	-457	14.9	61.4	-85	91
0.4	-450	13	60.5	-83	92

C(mM), E_{corr}(mV/SCE), i_{corr} (µA/cm^2), $ß_C$ (mV/dec), $ß_a$ (mV/dec), IE_p(%)

V.1.3.2 Electrochemical impedance spectroscopy (EIS)

The results obtained using this technique in 1M HCl medium are illustrated in the form of Nyquist diagrams (Figure V. 5).

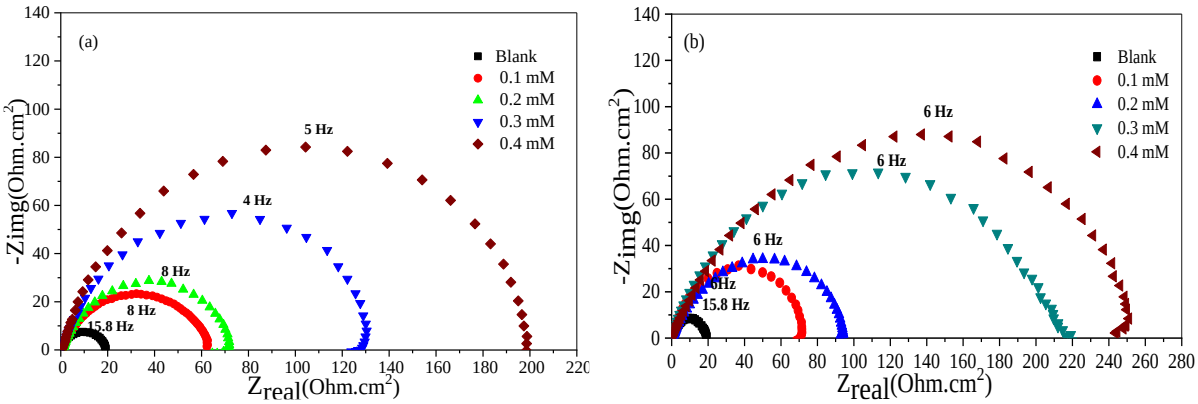

Figure V. 5. Nyquist impedance plots of XC48 steel obtained at 298K in HCl 1N solutions containing different concentrations of (a): DH4MPMP and (b): H4MPMPA.

The table V. 6 lists the values of the electrochemical parameters and the inhibitory efficiency, obtained by Electrochemical Impedance Spectroscopy (EIS). The addition of DH4MPMP and H4MPMPA leads to an increase in the value of R_p (199 and 258 $\Omega.cm^2$ respectively) and a decrease in the double layer capacitance C_{dl} (140,50 and 58,6 $\mu F.cm^{-2}$ respectively). Consequently, the inhibition efficiency increases and reaches maximum value of 90,4 and 92,6 % at a concentration of 0.4 mM of DH4MPMP and H4MPMPA respectively. This decrease is related to the adsorption of DH4MPMP or H4MPMPA on the steel surface.

Table V. 6. Electrochemical parameters derived from impedances diagrams.

	C	R_p	C_{dl}	IE_{EIS}
DH4MPMP	Blank	19	530.43	-
	0.1	63	312.50	62.7
	0.2	72	298.20	73.6
	0.3	128	199.30	85.1
	0.4	199	140.50	90.4
H4MPMPA	Blank	19	530.43	-
	0.1	72	345	73.6
	0.2	95	268	80.0
	0.3	211	60.3	91.0
	0.4	258	58.6	92.6

C(mM), $R_p(\Omega.cm^2)$, $C_{dl}(\mu F.cm^{-2})$, $IE_{EIS}(\%)$.

V.1.4 Molecular Dynamic Simulation (MDS)

The adsorption of DH4MPMP and H4MPMPA on the Fe (110) adsorbent was computationally evaluated using molecular dynamic simulations based on Monte Carlo theory, and the most equilibrium configurations are shown in the figure V. 6. Three different molecular configurations for the both ester and acid can be observed (Figure V. 6 (b, e)), that are largely

deformed comparatively to the relaxed DFT-optimized structures, giving considerable deformation energy, these various configurations maximize the surface coverage until forming a film on the metal surface. Otherwise, the water molecules were observed to be adsorbed in a hollow site of Fe (110) (Figure V. 6 (g and h)).

The proposed adsorption mechanism of molecules on the metal surface can be discussed via the interactions between molecules DH4MPMP or H4MPMPA and the Fe metal surface. The Fe-O and Fe-π distances are respectively about 2.84 and 3.02Å (Figure V. 6 (b and e)) for the acid molecules and about 3.08 and 3.67Å for the ester molecules, in such situation, the covalent bonding is uncommon due to the interface's significant width. Additionally, and as predicted previously, oxygen atoms in DH4MPMP and in H4MPMPA can donate electrons to the unoccupied d-orbital of iron to form coordinate bonds (chemical interaction), and anti-bonding orbital of π-electrons in the ring can accept electrons to form dative bonds [5] [6] [7] [8]. Furthermore, physical interactions may occur between DH4MPMP or H4MPMPA and the metal surface driven by van der Waals and electrostatic interactions (Figure V. 6 (c and f)), and caused by the high dipolar moment and the non-homogeneous distribution of the partial charges. Moreover, hydrogen bonds between adsorbent surface or adsorbate and water molecules can give us a prediction about the role of water molecules in the adsorption process which is represented in the ability to catch molecules and pull them to the surface of the metal. From these findings, it can be concluded that the physisorption dominates.

Moreover, from the table V. 7 it is clear that the adsorption of molecules on the metal surface is spontaneous, due to the minus sign of the adsorption energy [3]. The rigid adsorption energy of acid molecules and ester molecules are almost the same, while the deformation energy of ester molecule is greater than that acid molecules, indicating that the adsorption of acid on metal is more stable than that of ester. The found computed adsorption energy values are relatively in the same order than those of the good inhibitors [3] [4].

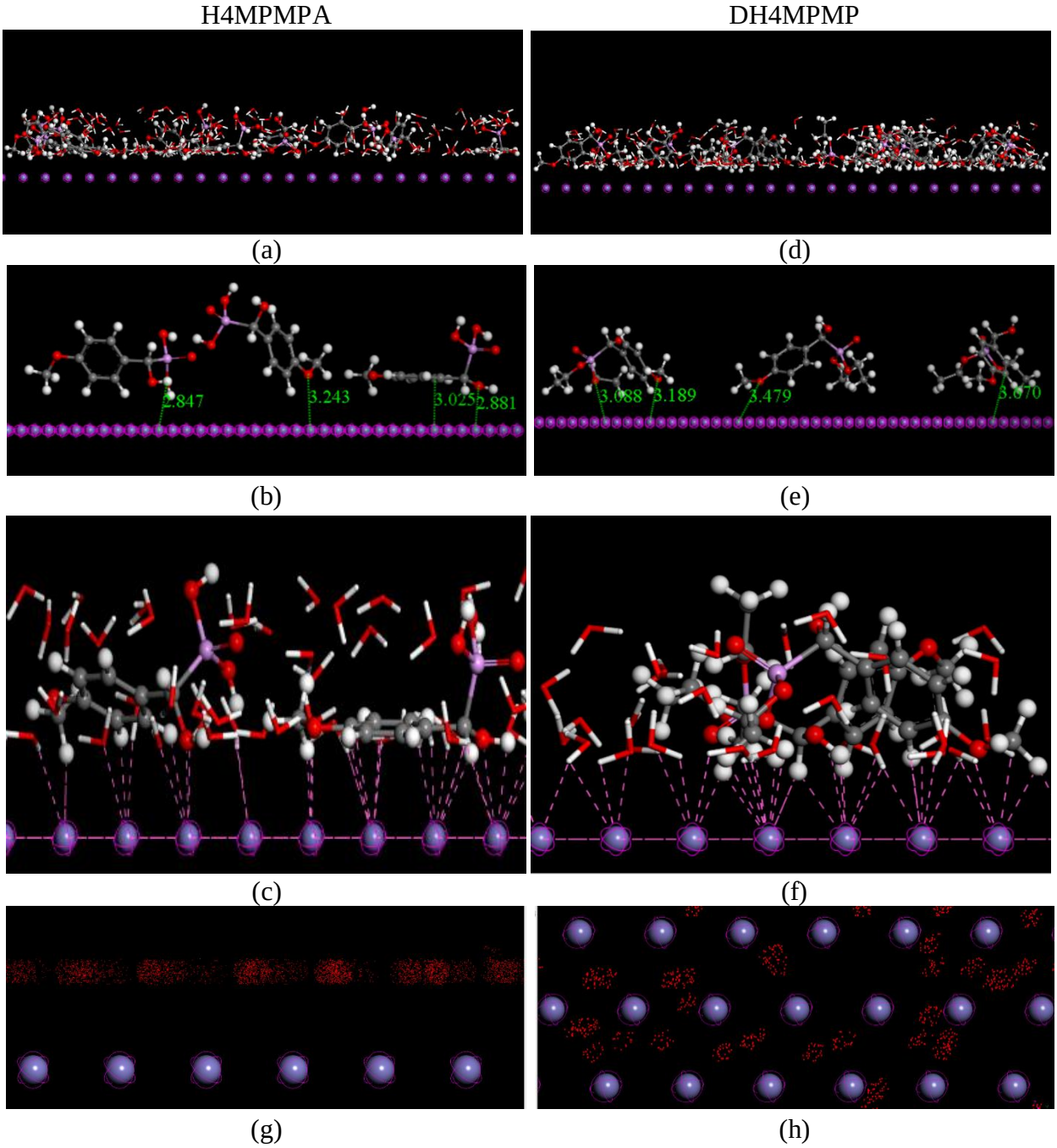

Figure V. 6. Equilibrium configurations of DH4MPMP (d, e, f), H4MPMPA (a, b, c), and water field on the Fe (110) surface.

Table V. 7. Adsorption energies (kJ.mol^{-1}) of DH4MPMP or H4MPMPA and water molecules on the Fe (110) surface.

	Total energy	Adsorption energy	Rigid adsorption energy	Deformation energy	dE_{ad}/dNi	
					Molecule	H_2O
H4MPMPA/Fe(110)	76.57	-47.10	-4.13	-42.96	-47.10	/
DH4MPMP/Fe(110)	81.26	-65.77	-5.84	-59.93	-65.77	/
H_2O/Fe(110)	-0.49	-1.40	-0.49	-0.90	/	-1.40
10H4MPMPA/Fe(110)/ 150H_2O	616.86	-755.07	-198.24	-556.83	-50.54	-0.94
10DH4MPMP/Fe(110)/ 150H_2O	639.95	-965.60	-240.38	-725.22	-69.52	-0.97

V.2 Electronic transport property of ionic liquids

Carbon paste electrodes (CPEs) are commonly used in academic and industrial researches due to their ease of manufacture and modification [9]. The electro-catalytic activity of carbon paste electrodes (CPEs) can be considerably increased by modifying them with ionic liquids (ILs) [10]. ILs enhance the electrode's conductivity, stability, and selectivity by providing a more conductive and stable surface for electron transport [11]. This change minimizes over potentials and promotes faster electrons exchange reactions, increasing the electrodes' efficiency [12]. Tailoring the characteristics of ILs allows the creation of highly selective electrodes for sensing, energy conversion, and environmental monitoring [11].

V.2.1 Current-voltage characteristic (I-V)

The figure V. 7 shows the electrochemical response of carbon paste electrode and modified carbon paste electrode with [VBmim$^+$, PF_6^-], [VBmim$^+$, Cl^-], and [VBmim$^+$, NTF_2^-]. It obvious that in the range of -1.5 to 1.23, the current remains close to zero. The flat zone suggests that no major electrochemical reactions are taking place in this potential range. Around 1.23 V, the current begins to rise significantly, peaking at 1.5 V. This increase indicates the start of an electrochemical process, in which the electrode potential is high enough to promote electron transfer with the species in the electrolyte.

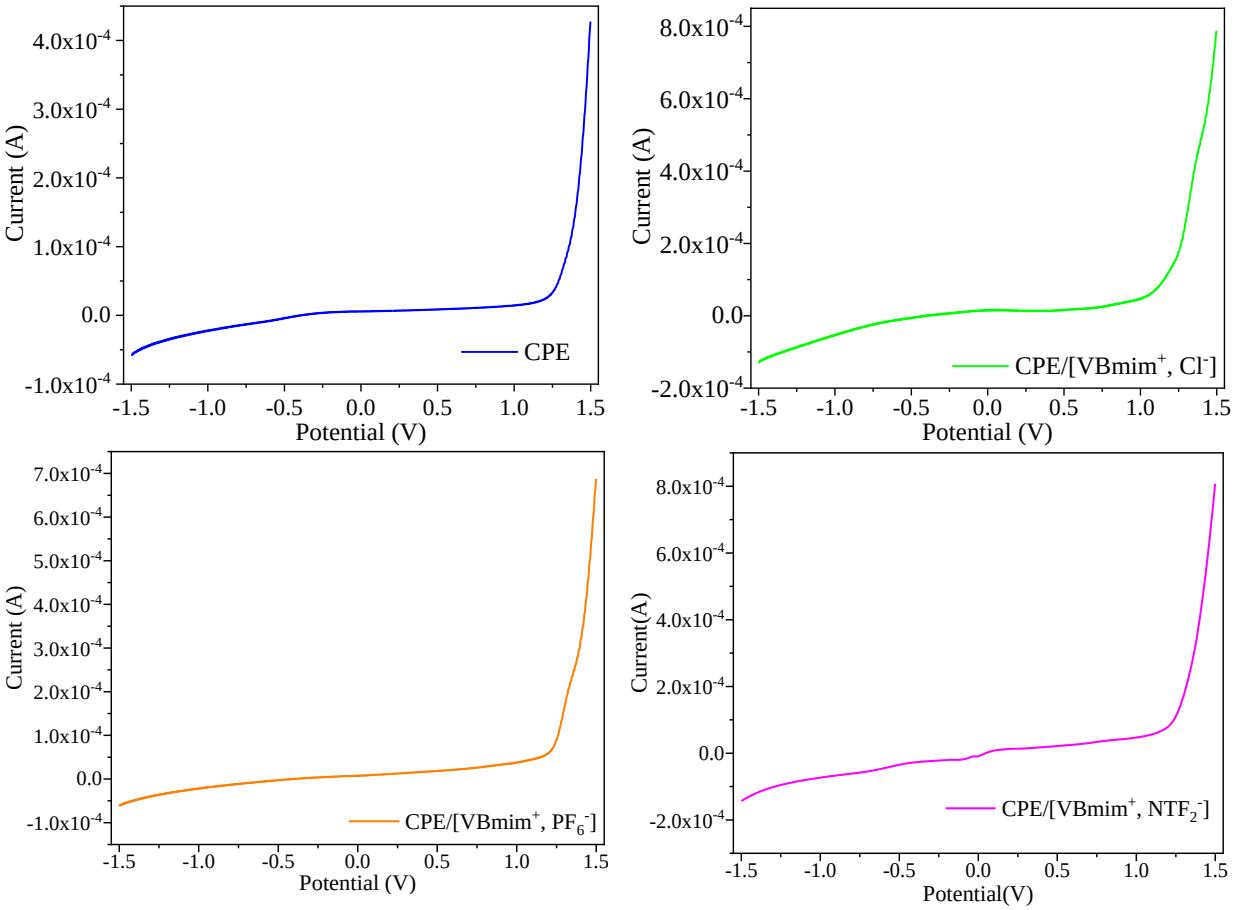

Figure V. 7. Curves of current voltage of CPE, CPE/[VBmim$^+$, Cl$^-$], CPE/[VBmim$^+$, PF$_6^-$] and CPE/[VBmim$^+$, NTF$_2^-$], in 0.1 M of KCl and 0.1 M of Fe(CN)$_6^{3-/4-}$ solution and a scan rate of 100 mV/s

V.2.2 Cyclic voltammetry analysis (CV)

The figure V. 8 shows the electrochemical response of unmodified and modified carbon paste electrode with the [VBmim$^+$, PF$_6^-$], [VBmim$^+$, Cl$^-$], and the [VBmim$^+$, NTF$_2^-$]. It is obvious that the presence of peak pair indicates the presence of electron transfer. For the unmodified CPE, peak-to-peak potential distance ΔEp was 0.393 V, According to a process of irreversible electron transfer. While for the modified CPE, the ΔEp was decreased to 0.293, 0.248 and 0.261 V for CPE/[VBmim$^+$, Cl$^-$], CPE/[VBmim$^+$, PF$_6^-$] and CPE/[VBmim$^+$, NTF$_2^-$] respectively, indicating a less irreversible electron transfer process. Furthermore, the anodic peak currents of Fe(CN)$_6^{3-/4-}$ for the CPE/[VBmim$^+$, Cl$^-$], CPE/[VBmim$^+$, PF$_6^-$], CPE/[VBmim$^+$, NTF$_2^-$] and CPE are 1.3, 1.82, 1.61 and 1.037 (10^{-3} A) respectively. While the cathodic peak current of Fe(CN)$_6^{3-/4-}$ for the CPE/[VBmim$^+$, Cl$^-$], $^-$], CPE/[VBmim$^+$, PF$_6^-$], CPE/[VBmim$^+$, NTF$_2^-$] and CPE are -1.24, -1.85, -1.41 and -0.75 ($\times 10^{-3}$ A) respectively. According to the experimental results above, all ILs modified CPE outperformed unmodified CPE in terms of increasing sensitivity and reversibility.

The usage of ILs as a modifier has been attributed for all of them. Consequently, ILs were crucial in enhancing the modified CPE's conductivity performance.

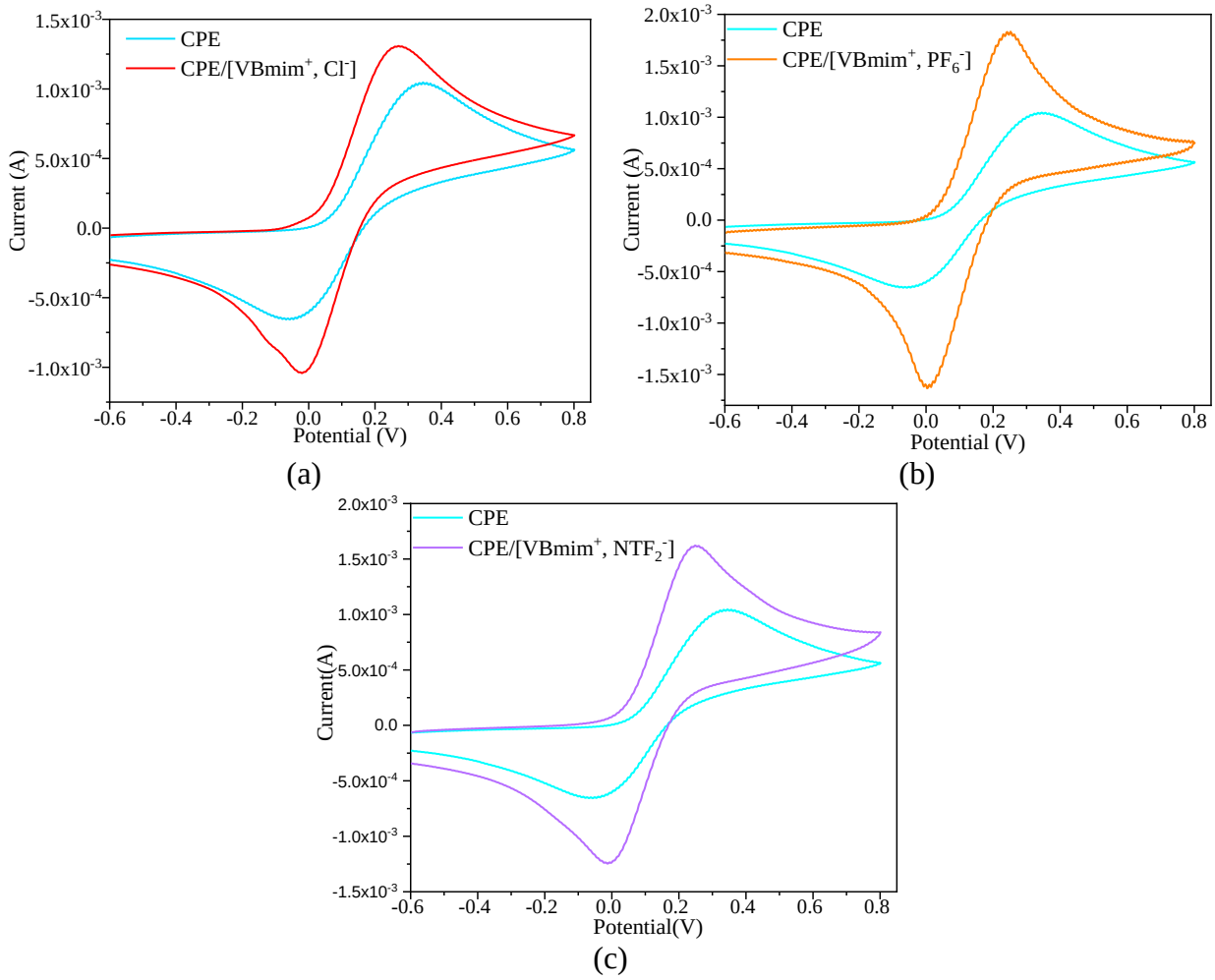

Figure V. 8. Cyclic voltammograms of unmodified CPE and modified CPE with (a):the [VBmim$^+$, Cl$^-$], (b): the [VBmim$^+$, PF$_6^-$] and (c): the [VBmim$^+$, NTF$_2^-$] in 0.1 M of KCl and 0.1 M of Fe(CN)$_6^{3-/4-}$ solution and a scan rate of 100 mV/s.

V.2.3 Electrochemical impedance spectroscopy (EIS)

The figure V. 9 shows the impedance measurements of the unmodified CPE and the modified CPE with ILs CPE/[VBmim$^+$, Cl$^-$], CPE/[VBmim$^+$, PF$_6^-$], and CPE/[VBmim$^+$, NTF$_2^-$] in 0.1 M of Fe(CN)$_6^{3-/4-}$ redox couple and 0.1 M of KCl solution as elecrolyte. It is obvious that each Nyquist plot partially represents a depressed semicircle in the mid-frequency region, which can be related to the charge transfer mechanism during the electrochemical reaction.Moreover, the slope of the straight line showed in the low-frequency region indicating the mass transfer [13]. When the ionic liquid is added, the depressed semicircle diameter decreases this indicates a decrease in

the electronic transfer resistance value, and the module of the impedance decrease indicating an increase in the capacitance value.

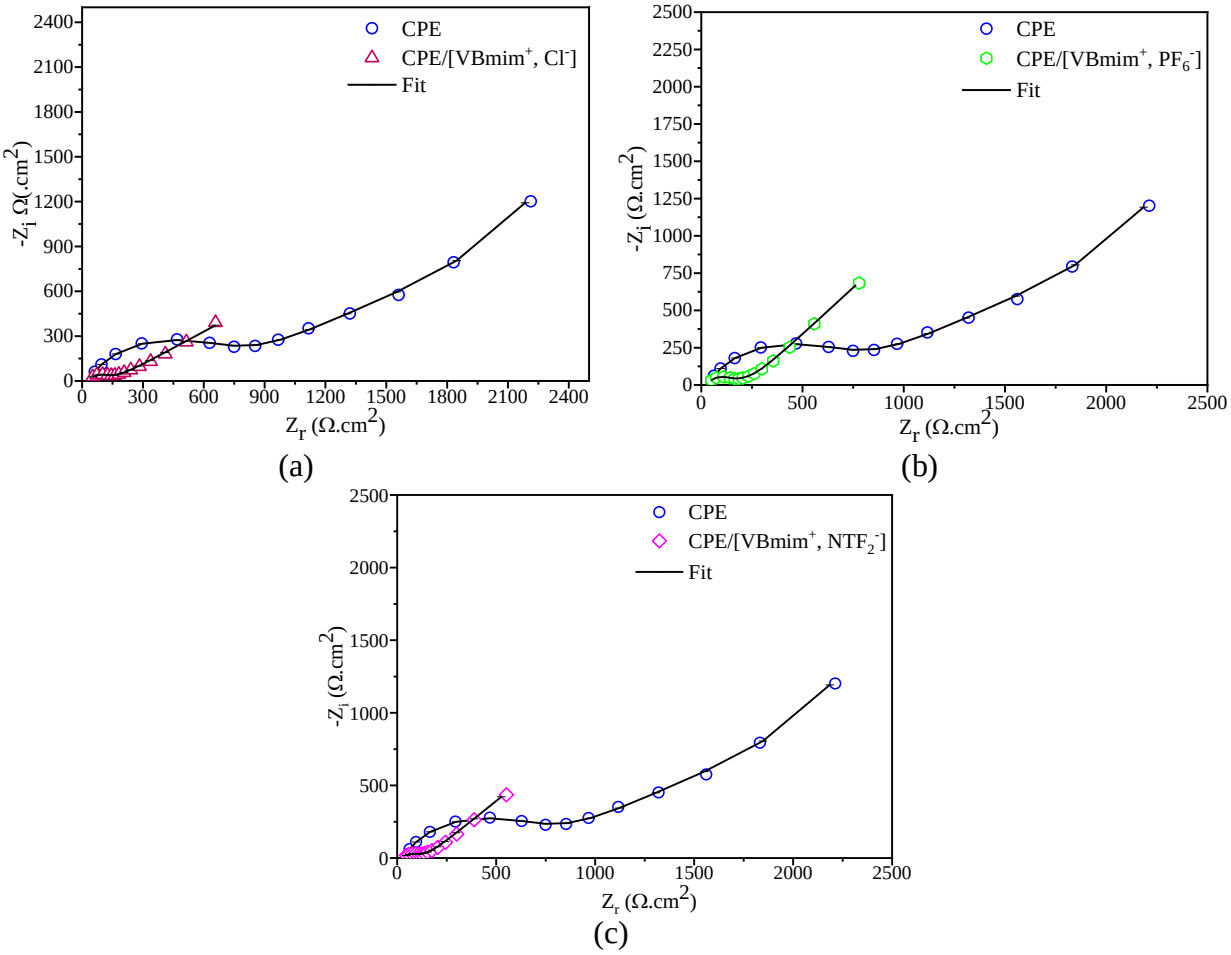

Figure V. 9. Nyauist plots of unmodified CPE and modified CPEs with (a):the [VBmim$^+$, Cl$^-$], (b): the [VBmim$^+$, PF$_6^-$] and (c): the [VBmim$^+$, NTF$_2^-$]in 0.1M KCl and 0.1 M $Fe(CN)_6^{3-/4-}$ solution, and a scan rate of 100 mV/s.

A proposal of an electric circuit to modulate the electrical behaviour of electrodes involves that the impedance could be fitted using R_s(CPE (R_{ct}W)) model (Figure V. 11). Each element in the equivalent circuit explain a part of electrodes impedance. Were R_s indicates the solution resistance, CPE represents the constant phase element in this case it represents the non-ideal double layer capacitance, R_{ct} is the resistance to the charge transfer, and W indicates the Warburg impedance to explain the mass transfer resistance.

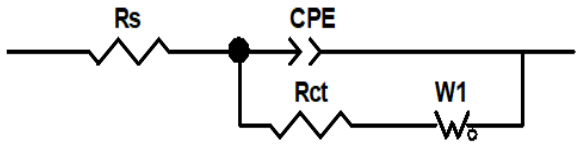

Figure V. 10. Proposed electrical equivalent circuit.

The charge transfer resistance (R_{ct}) for the unmodified CPE takes a value of 637 Ohm, while it takes 25.67, 86.38, and 41.2 Ohm in the case of CPE/[VBmim$^+$, Cl$^-$], CPE/[VBmim$^+$, PF$_6^-$], and CPE/[VBmim$^+$, NTF$_2^-$] modified CPE respectivelly. For the Warburg impedance values, it takes values 0.3690, 0.0055, 0.2868, and 0.2658 S.sec^5 for the unmodified CPE, CPE/[VBmim$^+$, Cl$^-$], CPE/[VBmim$^+$, PF$_6^-$], and CPE/[VBmim$^+$, NTF$_2^-$] modified CPE respectively.

Table V. 8. Fit results of the experimental EIS data.

	R_s [Ω.cm^2]	CPE [S.sec^n]	R_{ct} [Ω.cm^2]	W [S.sec^5]
CPE	35.81	2.10×10^{-6}	637	0.3690
CPE/[VBmim$^+$, Cl$^-$]	40.67	3.90×10^{-7}	25.67	0.0055
CPE/[VBmim$^+$, PF$_6^-$]	34.78	7.96×10^{-7}	86.38	0.2868
CPE/[VBmim$^+$, NTF$_2^-$]	34.76	3.06×10^{-6}	41.2	0.2658

V.2.3.1 Mechanism of conductivity (charge transfer)

It obvious that the addition of the ILs in the CPE influences the charge transfer process within the electrode, the fit indicates a change of the constant phase element value; this change can be related to variation the charge of electrodes surface or in the surface roughness [14]. In addition, a rise in the charge and mass transfers was remarked owing to the ionic conductivity and the liquid aspect of ILs. Additionally to the charge and the mass transfer provided by the graphite, novel ways were generated within minority ILs phase.

V.3 Conclusions

From the corrosion inhibition study, the weight loss measurement indicates that the phosphonates molecules DH4MPMP and H4MPMPA exhibit an inhibition efficiency reaching a maximum at 0.4 mM of 91 and 93 %, while for the ionic materials it reaches 95% for 2,4,6-triamino-1,3,5-triazin-1,3-dium bisperchlorate monohydrate at 0.5×10^{-4} M and 97 % at 10^{-6} M for [VBmim$^+$, Cl$^-$]. In addition, polarization studies demonstrate the mixed inhibitory effect for DH4MPMP and H4MPMPA. The decrease of C_{dl} and the rises of R_{ct} estimated by EIS confirm that DH4MPMP and H4MPMPA were well adsorbed on the metal/electrolyte surface. The

calculations based on MD simulations confirm the experimental findings and predict that the inhibitors have strong ability to be adsorbed on the metal surface.

The electrocatalytic activity of the prepared electrodes was studied via I-V, CV, and EIS analysis. The I-V curves indicate that all electrodes are stable within the potential domain from -1.5 to 1.23 V. For the modified CPEs, CVs present an intense oxidation and reduction pics, indicating more efficiency and sensitivity. The modified CPEs presented also faster redox reactions appear by diminishing the peak-to-peak potential separation. EIS confirms the above conclusions by weaker impedances for modified-CPE and investigate the conductivity of the modified and unmodified CPS, it was found that the ILs enhance the conductivity within the electrodes.

V.4 References

[1] Y. L. Kobzar and K. Fatyeyeva, "Ionic liquids as green and sustainable steel corrosion inhibitors: Recent developments," *Chemical Engineering Journal*, vol. 425, p. 131480, Dec. 2021, doi: 10.1016/j.cej.2021.131480.

[2] S. Gurjar, S. K. Sharma, A. Sharma, and S. Ratnani, "Performance of imidazolium based ionic liquids as corrosion inhibitors in acidic medium: A review," *Applied Surface Science Advances*, vol. 6, p. 100170, Dec. 2021, doi: 10.1016/j.apsadv.2021.100170.

[3] R. Bourzami, L. Ouksel, and N. Chafai, "Synthesis, spectral analysis, theoretical studies, molecular dynamic simulation and comparison of anticorrosive activity of an ester and an acid α-Hydroxyphosphonates," *Journal of Molecular Structure*, vol. 1195, pp. 839–849, Nov. 2019, doi: 10.1016/j.molstruc.2019.06.012.

[4] L. Ouksel, R. Bourzami, S. Chafaa, and N. Chafai, "Solvent and catalyst-free synthesis, corrosion protection, thermodynamic, MDS and DFT calculation of two environmentally friendly inhibitors: Bis-phosphonic acids," *Journal of Molecular Structure*, vol. 1222, p. 128813, Dec. 2020, doi: 10.1016/j.molstruc.2020.128813.

[5] S. Şafak, B. Duran, A. Yurt, and G. Türkoğlu, "Schiff bases as corrosion inhibitor for aluminium in HCl solution," *Corrosion Science*, vol. 54, pp. 251–259, Jan. 2012, doi: 10.1016/j.corsci.2011.09.026.

[6] N. Chafai, S. Chafaa, K. Benbouguerra, D. Daoud, A. Hellal, and M. Mehri, "Synthesis, characterization and the inhibition activity of a new α-aminophosphonic derivative on the corrosion of XC48 carbon steel in 0.5M H2SO4: Experimental and theoretical studies," *Journal of the Taiwan Institute of Chemical Engineers*, vol. 70, pp. 331–344, Jan. 2017, doi: 10.1016/j.jtice.2016.10.026.

[7] S. M. Wetterer, D. J. Lavrich, T. Cummings, S. L. Bernasek, and G. Scoles, "Energetics and Kinetics of the Physisorption of Hydrocarbons on Au(111)," *J. Phys. Chem. B*, vol. 102, no. 46, pp. 9266–9275, Nov. 1998, doi: 10.1021/jp982338+.

[8] S. Abbout, R. Hsissou, L. Ouksel, R. Bourzami, H. Erramli, D. Chebabe and N. Hajjaji, "Anticorrosion propriety of new resin epoxy derived from phosphorus as inhibitor of steel

corrosion in 0.5 M H_2SO_4," *Journal of Molecular Structure*, vol. 1294, p. 136491, Dec. 2023, doi: 10.1016/j.molstruc.2023.136491.

[9] I. Švancara, K. Vytřas, K. Kalcher, A. Walcarius, and J. Wang, "Carbon Paste Electrodes in Facts, Numbers, and Notes: A Review on the Occasion of the 50-Years Jubilee of Carbon Paste in Electrochemistry and Electroanalysis," *Electroanalysis*, vol. 21, no. 1, pp. 7–28, Jan. 2009, doi: 10.1002/elan.200804340.

[10] N. Maleki, A. Safavi, and F. Tajabadi, "Investigation of the Role of Ionic Liquids in Imparting Electrocatalytic Behavior to Carbon Paste Electrode," *Electroanalysis*, vol. 19, no. 21, pp. 2247–2250, Nov. 2007, doi: 10.1002/elan.200703952.

[11] S. Šekuljica, V. Guzsvány, J. Anojčić, T. Hegedűs, M. Mikov, and K. Kalcher, "Imidazolium-based ionic liquids as modifiers of carbon paste electrodes for trace-level voltammetric determination of dopamine in pharmaceutical preparations," *Journal of Molecular Liquids*, vol. 306, p. 112900, May 2020, doi: 10.1016/j.molliq.2020.112900.

[12] M. Opallo and A. Lesniewski, "A review on electrodes modified with ionic liquids," *Journal of Electroanalytical Chemistry*, vol. 656, no. 1–2, pp. 2–16, Jun. 2011, doi: 10.1016/j.jelechem.2011.01.008.

[13] A. Sanou, M. Coulibaly, S. R. N'dri, T. L. Tămaș, L. Bizo, T. Frentiu, E. Covaci, K. D. M. Abro, P. J.-M. R. Dablé, K. B. Yao, C. L. Forat and G. L. Turdean, "Raw clay material-based modified carbon paste electrodes for sensitive heavy metal detection in drinking water," *J Mater Sci*, vol. 59, no. 30, pp. 13961–13977, Aug. 2024, doi: 10.1007/s10853-024-09945-2.

[14] C. L. Alexander, B. Tribollet, and M. E. Orazem, "Contribution of Surface Distributions to Constant-Phase-Element (CPE) Behavior: 1. Influence of Roughness," *Electrochimica Acta*, vol. 173, pp. 416–424, Aug. 2015, doi: 10.1016/j.electacta.2015.05.010.

General conclusion

General conclusion

This research investigates the structural, electrical, thermal, optical, and optoelectronic properties of two ionic materials types: the first one is ionic organic-inorganic crystals, and the second is ionic liquids.

Starting with the results related to the first type of ionic materials, two new hybrid ionic crystals: 2,4-diamino-6-phenyl-1,3,5-triazinium perchlorate ($C_9H_{10}N_5^+.ClO_4^-$) and 2,4,6-triamino-1,3,5-triazin-1,3-dium bisperchlorate monohydrate ($C_3H_8\ N_6^{2+}.2Cl\ O_4^-.H_2O$) were successfully elaborated. The structures of the ionic hybrid crystals was studied experimentally by single crystal XRD, showing that 2,4-diamino-6-phenyl-1,3,5-triazinium perchlorate crystalizes in monoclinic system, while 2,4,6-triamino-1,3,5-triazin-1,3-dium bisperchlorate monohydrate crystalizes in triclinic system. The weak interactions maintain the structure's stability, giving a hybrid ionic crystals type I. The optoelectronic properties have been studied experimentally by UV-Visible spectroscopy, illustrating two absorption bands in the UV domain located at the maxima of 204 and 247nm for the 2,4-diamino-6-phenyl-1,3,5-triazinium perchlorate. While for 2,4,6-triamino-1,3,5-triazin-1,3-dium bisperchlorate monohydrate have two absorbance bands in the UV domain located at the maxima of 207 and 235nm, noting a good transparency in ultraviolet-visible and entire visible domains. Various infrared modes were indicated and assigned, in which various modes confirm the presence of inter molecular hydrogen bonds within the crystals. The 2,4-diamino-6-phenyl-1,3,5-triazinium perchlorate title is stable until 290 °C, while, the 2,4,6-triamino-1,3,5-triazin-1,3-dium bisperchlorate monohydrate is stale until 256 °C, making them suitable for thermal applications.

The second type of the studied ionic materials, both experimental and theoretical methods were employed to study the [$VBmim^+$, Cl^-], [$VBmim^+$, PF_6^-] and [$VBmim^+$, NTF_2^-] imidazolium based ionic liquids. Firstly, the molecular structures were optimized using the DFT with B3LYP functional and 6-311G++ (d, p) basis sets. Afterward, the corresponding theoretical FT-IR spectra were compared to the experimental ones, and the various vibration bands were all assigned. In addition, the [$VBmim^+$, Cl^-], [$VBmim^+$, PF_6^-] and [$VBmim^+$, NTF_2^-] exhibit a thermal stability around 270 °C, noting that the anion nature influence the degradation behaviour. Using DFT-theoretical calculations we were able to predict: the molecular orbitals, mapping electrostatic potential, partial charges, dipolar moment and some global quantum chemical descriptors, founding that all ILs exhibit a high value of dipolar moment. According to the GQCDs results, all

Ils are hard, kinetic stable and low chemical reactive, and have an acceptor character. From the vibrational data, the heat capacity, entropy, and enthalpy were calculated, and found to increase with the increase of temperature, ranging from 150 to 560 K. The study was extended to analyse the nonlinear optical properties of [$VBmim^+$, Cl^-], [$VBmim^+$, PF_6^-] and [$VBmim^+$, NTF_2^-], the polarizability is highest for [$VBmim^+$, NTF_2^-], showing that it has a higher average response to an external electric field, $\Delta\alpha$ also follows this trend, indicating increased anisotropy in the polarizability tensor for [$VBmim^+$, NTF_2^-]. β_{tot} is highest for [$VBmim^+$, Cl^-], indicating its strong nonlinear optical activity compared to the other ILs. Normalizing β_{tot} with respect to urea shows that these ionic liquids possess significantly higher hyperpolarizabilities, particularly [$VBmim^+$, Cl^-]. From the TD-DFT, all ILs have a total transmission in the visible domain while, they have three-overlapped absorbance sub bands in UV one.

A corrosion inhibition study on the ionic materials using the weight loss measurement indicates that 2,4,6-triamino-1,3,5-triazin-1,3-dium bisperchlorate monohydrate at 0.5×10^{-4} M reaches 95%, and 97% at 10^{-6} M for [$VBmim^+$, Cl^-], While for the phosphonates molecules DH4MPMP and H4MPMPA exhibit an inhibition efficiency reaching a maximum at 0.4 mM of 91 and 93%. In addition, polarization studies demonstrate the mixed inhibitory effect for DH4MPMP and H4MPMPA. The decrease of C_{dl} and the rises of R_{ct} estimated by EIS confirm that DH4MPMP and H4MPMPA were well adsorbed on the metal/electrolyte surface. The calculations based on MD simulations confirm the experimental findings and predict that the inhibitors have strong ability to be adsorbed on the metal surface. This study was performed first on the phosphoric molecules for optimising the work protocol and it is already in progress on the studied ionic materials.

The electro-catalytic activity of the prepared electrodes was studied via I-V, CV, and EIS analysis. The I-V curves indicate that all electrodes are stable within the potential domain from -1.5 to 1.23 V. For the modified CPEs, CVs present an intense oxidation and reduction pics, indicating more efficiency and sensitivity. The modified CPEs presented also faster redox reactions appear by diminishing the peak-to-peak potential separation. EIS confirms the above conclusions by weaker impedances for modified-CPE and investigate the conductivity of the modified and unmodified CPS, it was found that the ILs enhance the conductivity within the electrodes.

Perspectives

Perspectives

The work of this PhD reached various results, and makes a lot of point to elucidate, that can be classified for the continuation of the work as: short and long term perspectives, as well as, perspectives needing collaborations.

a/ *Short-term perspectives:*

- Continue the study of the ionic materials for their corrosion inhibition activities.
- Conducting DFT calculations on the ionic organic-inorganic crystals to study the electronic properties.
- Study the use of the modified carbon paste electrodes with ionic liquids as detectors.

b/ Long-term perspectives:

- Study the possibility of the use of ionic liquids as electrolyte support in energy storage batteries.

c/ Perspectives needing collaborations

- Study the dielectric properties of the ionic materials.
- Test of the biological activities: anti-oxidant and anti-bacterial as well as their molecular docking.
- Study experimentally the ionic single crystals for their non-linear optical response.
- Use the MOFs' in our work along with the ionic materials.

Publications

Journal of Molecular Liquids 417 (2025) 126659

Contents lists available at ScienceDirect

Journal of Molecular Liquids

journal homepage: www.elsevier.com/locate/molliq

A comprehensive exploration of structural, vibrational, optical, thermal and corrosion inhibition properties of trihexyl(tetradecyl)phosphonium dicyanamide ionic liquid: Experimental and theoretical methods

Rima Kiche [a,b], Riadh Bourzami [c,*], Louiza Ouksel [b], Mohamed Belhocine [d,e], Lotfi Boudjema [c,f], Fayçal Dergal [g,h]

[a] Department of Physics, Faculty of Sciences Ferhat Abbas, University Sétif-1, Algeria
[b] Laboratory of Electrochemistry and Materials (LEM), Ferhat Abbas, University Sétif-1, Algeria
[c] Research Unit on Emergent Materials, Ferhat Abbas, University Sétif-1, Algeria
[d] Laboratory of Synthesis and Catalysis, Ibn-Khaldoun University, Tiaret, Algeria
[e] Department of Matter Sciences, Faculty of Science and Technology, Tissemsilt University, Tissemsilt, Algeria
[f] Department of Chemistry, University College London, 20 Gordon St., London WC1E 6BT, United Kingdom
[g] Center for Scientific and Technical Research in Physico-chemical Analyses (CRAPC), Bp 384, Bousmail, Algeria
[h] Laboratory of Catalysis and Synthesis in Organic Chemistry (LCSCO), Faculty of Sciences, University of Tlemcen, BP 119, 13000 Tlemcen, Algeria

ARTICLE INFO

Keywords:
Trihexyl(tetradecyl)phosphonium dicyanamide
Ionic LIQUID
Electrochemistry
Density functional theory
Nonlinear optic
Grand canonical Monte Carlo

ABSTRACT

The aim of the present study is to investigate the physical, chemical, and corrosion inhibition properties of the trihexyl(tetradecyl)phosphonium dicyanamide $[P_{666,14}][N(CN)_2]$ combining both experimental and theoretical approaches. The molecular structure was optimized using DFT-calculations, as well as, mapping electrostatic potential, molecular orbitals and partial charges. $[P_{666,14}][N(CN)_2]$ was characterized by global quantum physic-chemical descriptors that showed its chemical hardness, stability, and low-reactivity. The FTIR/RAMAN vibration modes were identified thanks to the DFT, and correlated with the molecular structure. Furthermore, thermal analysis revealed a high thermal stability up to 423 °C. On the other hand, the nonlinear optical response was discussed using the calculated polarizability, illustrating a considerable performance compared to urea. Finally, electrochemical methods were used to investigate the corrosion inhibition of XC48-steel, and molecular dynamics simulations of interfacial configurations: $[P_{666,14}][N(CN)_2]$–H_2O/Fe(1 1 0) and $[P_{666,14}][N(CN)_2]$–H_2O/Fe_2O_3(1 0 4), that were used to propose an inhibition mechanism.

1. Introduction

The ionic bonding of positively and negatively charged ions produces ionic compounds, which are atoms or molecules with an electric charge (cations or anions); table salt (sodium chloride, NaCl) is a common example [1]. Ionic liquids (ILs) are salts in the liquid state defined by a low melting point below 100 °C [2] and are characterized by various of physical properties [3], such as low volatility [4,5], non-flammability, high ionic conductivity [6,7], and thermal and chemical stability [8]. Ionic liquids have been clearly identified as green and designer materials [9,10].and may be used in low-melting mixture solvents [11]. Otherwise, ionic liquids might absorb water from the air due to their hygroscopic nature. It has been shown that in ionic liquids, water molecules absorbed from the air are mostly present in the "free" (not self-associated) state, bound via H-bonding with $[N(CN)_2]^-$ at the concentrations of dissolved water in the range of 0.2–1.0 mol·dm^{-3} [12].

Typically, phosphorus molecular materials refer to a class of chemical compounds or materials where phosphorus atoms are the primary building blocks and covalent bonds bind them together to form molecules. Although covalent connections can range from 1 to 6, the most typical coordination numbers for the phosphorus atom are 3, 4, or 5 which offer various geometries [13]. These materials encompass a wide range of chemical compounds, such as phosphorus-containing organic molecules [14]. Phosphoric compounds have many applications in organic chemistry [15], biology [16], materials science [17], and the semiconductor industry [18]. In addition, some ionic compounds have phosphorus ions as one of their constituent ions. For example, calcium phosphate, $Ca_3(PO_4)_2$ [19], hydroxyapatite, $Ca_5(PO_4)_3OH$ [20], and

* Corresponding author.
E-mail address: riadh_bourzami@hotmail.com (R. Bourzami).

https://doi.org/10.1016/j.molliq.2024.126659
Received 22 June 2024; Received in revised form 28 November 2024; Accepted 1 December 2024
Available online 5 December 2024
0167-7322/© 2024 Elsevier B.V. All rights are reserved, including those for text and data mining, AI training, and similar technologies.

ISSN 0036-0244, Russian Journal of Physical Chemistry A, 2024. © Pleiades Publishing, Ltd., 2024.

ELECTROCHEMISTRY. GENERATION AND STORAGE OF ENERGY FROM RENEWABLE SOURCES

Synthesis and Investigations of Corrosion Inhibition Performance of an Ester and Acid α-Hydroxyphosphonates Combining Experimental, Density Functional, and Monte Carlo Methods

Rima Kiche[a,c], Louiza Ouksel[a], and Riadh Bourzami[b,*]

[a] *Laboratoire d'Electrochimie des Matériaux (LEM), Département de Génie des Procédés, Faculté de Technologie Université Ferhat Abbas, Sétif-1, 19000 Algeria*

[b] *Emerging Materials Research Unit, Ferhat Abbas University Sétif-1, Sétif-1, 19000 Algeria*

[c] *Département de Physique, Faculté des Sciences Université Ferhat ABBAS Sétif-1, Sétif-1, 19000 Algeria*

** e-mail: riadh_bourzami@hotmail.com*

Received July 18, 2023; revised September 11, 2023; accepted September 12, 2023

Abstract—[Hydroxy(4-methoxyphenyl) methyl]-phosphonate acid (H4MPMPA) and diethyl-[hydroxy(4-methoxyphenyl) methyl] phosphonate (DH4MPMP) were synthetized. Chemical and electrochemical techniques were used to examine their effectiveness at preventing XC48 corrosion when exposed to HCl. The weight loss method demonstrate the production of a protector film that obey to Langmuir isotherm, the polarization measurements prove that the inhibition process are mixt, and EIS shows that the efficiencies rise in parallel with the inhibitors' concentration. According to AFM, the corroded XC48's average roughness (360.5 nm) was higher than that obtained in the presence of DH4MPMP or H4MPMPA 169.78 and 60.70 nm, respectively. DFT calculates several thermodynamic and electronic parameters and investigates whether electron transfer affects inhibition. It also reveals that the nucleophile and electrophile zones are situated around oxygen and hydrogen atoms respectively. MDS simulates the interface configuration, demonstrating interfacial distances of 2.84/3.67 and 3.02/3.08 Å for Fe–O/Fe-π of H4MPMPA and DH4MPMP respectively, supporting mixt process at these distances.

Keywords: α-hydroxyphosphonate, corrosion inhibition, AFM, DFT calculation, MD simulations

DOI: 10.1134/S0036024424020171

1. INTRODUCTION

One of the greatest issues in human society is generally recognized to be metal corrosion. In addition to having an economic impact, it also has social and environmental ones since it poses health and safety risks to people who work in the related industries or reside in nearby cities [1]. Metal corrosion owing to changes in the external environment or the actions of the metal's heterogeneities. Acidic aqueous solutions are typically the most aggressive media for metals and their alloys. Moreover, the corrosion impact can be lessened or completely stopped through using inhibitors, which are compounds introduced to the media in low concentrations [2]. In this way, several organic substances have been investigated for their involvement in the corrosion process and are actually used as steel corrosion inhibitors against acidic conditions, these organic inhibitors can replace the pre-adsorbed acid and water molecules at the interface by forming a barrier between the surface of a metal and solution [3]. Organic inhibitors are formed by organic molecules with heteroatoms such as oxygen, nitrogen, sulfur and phosphorus, and/or formed by aromatic rings and π conjugate bonds [4]. In addition, the adhesion of organic inhibitors to metallic surfaces and the nature of interactions between the molecule and the metal are both governed by the physicochemical properties of the molecule, the metallic surface, and the electrolytic solution [5].

Due to their high stability, low toxicity, and good adsorption affinity on metal surface [6–9], organophosphorus compounds are commonly utilized as corrosion inhibitors of metals and alloys [8, 10]. Among the organophosphorus, numerous studies show the use of phosphonate to protect carbon steel from corrosion under various conditions [11, 12], moreover, considerable attention has been given to α-hydroxyphosphonate compounds as inhibitor [13], as well as antibacterial, antiviral, anti-cancer and antioxidant agents [14], they are also precursors for a significant phosphonate derivative [15, 16]. Few researches used the α-hydroxyphosphonate as a corrosion inhibitor.

In continuation of our work on α-hydroxyphosphonate and their properties, this paper reports a facile synthesis of H4MPMPA and DH4MPMP, and the study of their inhibition performances for XC48 steel

Diamond & Related Materials 125 (2022) 109022

Contents lists available at ScienceDirect

Diamond & Related Materials

journal homepage: www.elsevier.com/locate/diamond

Effect of high rGO ratio on structural properties, photoluminescence and adsorptive & photocatalytic performances under 365 nm-UV and simulated solar lightsofNaTaO$_3$/rGO heterojunction composites

Riadh Bourzami [a,*], Youcef Messai [b], Louiza Ouksel [c], Rima Kiche [c], Mohamed Khalil Guediri [d], Abdelmounaim Chetoui [e]

[a] Emerging Materials Research Unit, Ferhat Abbas University Sétif 1, Sétif 19000, Algeria
[b] Laboratoire d'Etude des Surfaces et Interfaces de la Matière Solide (LESIMS), Université Badji Mokhtar, Annaba 23000, Algeria
[c] Laboratoire d'électrochimie et Matériaux (LEM), département de génie de procédés, Faculté de Technologie, Université Ferhat Abbas-Sétif-1, Route de Bejaia, Sétif 19000, Algeria
[d] Département de Génie des Procédés, Laboratoire de Génie des Procédés Chimiques, Faculté de Technologie, Université Ferhat Abbas Setif 1, 19000, Setif, Algeria
[e] Centre de recherche en technologies des semiconducteurspourl'énergétique (CRTSE), 02, Bd. Dr. Frantz Fanon, B.P. 140, 7 Merveilles, Alger, Algeria

ARTICLE INFO

Keywords:
Perovskite
NaTaO$_3$
Heterojunction
Reduced graphene oxide
Photoluminescence
Adsorption
Photocatalysis

ABSTRACT

Perovskite NaTaO$_3$ nanocrystals were synthesized using hydrothermal route, and were employed as substrate to deposit several high rGO mass ratios (NaTaO$_3$/rGO$_x$, x = 0, 10, 15 and 20%). X-Ray Diffraction (XRD) proved that NaTaO$_3$ has an orthorhombic perovskite crystalline structure; this phase was conserved after the deposit of rGO, noting a varying of the orientation at the interface. The composites were analyzed by Infrared-spectroscopy (IR), which the absorbed frequencies were all ascribed to different vibrational modes inside the NaTaO$_3$ and rGO structures. Scanning Electron Microscope (SEM) images illustrate the formation of the heterojunction and the mixing of NaTaO$_3$ and rGO sheets with grain seize around 300 nm, and RAMAN-spectroscopy illustrates the obtaining of weak stacked graphene and disordered nano-graphene sheets. In addition, Photoluminescence (PL) reveals large Stocks shift about 60 nm, both XRD and PL reveal that the electronic and structural properties are affected by the deposited rGO. The composites were evaluated for their enhanced adsorptive performance, about 12 mg/g was measured for NaTaO$_3$/rGO$_{20\%}$; and various kinetic models were employed for the adsorption, proving that the adsorption mechanism is governed by film-diffusion and/or chemical reactions process. Finally, the combined process adsorption-photocatalysis for NaTaO$_3$/rGO$_x$ illustrate a total elimination of pollutant compared to pristine NaTaO$_3$.

1. Introduction

Environmental remediation deals with the deletion of pollutions or contaminants from environmental media, such as: soil, sediment, surface water or ground water [1,2]. In the two last decades, in-situ oxidation technology becomes popular way for remediation of water [3,4]. Using nanoparticles as reactive agents to immobilize or degrade water's pollutants is named nano-remediation of water [5–8]. The nanoparticles brought into direct contact with water, immobilize pollutants by adsorption or more degrade them through redox reactions [9–12], this last way is based mainly on catalytic water splitting. Recently, the use of catalyst nanoparticles suspended in water has been intensively studied and used by dint of their eco-friendship, cleanliness and reproducibility of the process [13–21]. Among the catalyst nanoparticles, the perovskite ones has been widely proposed [22–25]. A perovskite is any compound with a crystal structure similar to the mineral called Perovskite, which consists of calcium titanium oxide (CaTiO$_3$) [26]. The mineral was first discovered in the Ural Mountains of Russia by Gustav Rose in 1839 and named after by the mineralogist L. A. Perovski bearing his name [27]. The general chemical formula of perovskite compounds is ABX$_3$, where, 'A' and 'B' are two cations, often of very different sizes, and X is an anion (frequently oxygen atom) that bonds to both cations, the 'A' atoms are generally larger than the 'B' atoms, where these lasts are 3d, 4d, and 5d transition metal elements. A large combination of metallic elements are stable inperovskite structure [28]. Furthermore, four main categories of charge dependent cation-

* Corresponding author.
E-mail address: riadh_bourzami@hotmail.com (R. Bourzami).

https://doi.org/10.1016/j.diamond.2022.109022
Received 30 October 2021; Received in revised form 10 March 2022; Accepted 2 April 2022
Available online 6 April 2022
0925-9635/© 2022 Published by Elsevier B.V.

Algerian Journal of Engineering Architecture and Urbanism Vol. 5 Nr. 5 2021
ISSN: 2588-1760

Self-assembly construction of new supramolecular material, nonlinear, thermodynamic and thermal properties: experimental and theoritical approaches

Louiza Ouksel
PhD, Laboratoire d'Electrochimie et Matériaux (LEM), Département de génie des procédés, Faculté de Technologie, Université Ferhat Abbas, Sétif-1,19000. Algérie, l.ouksel@univ-setif.dz

Riadh Bourzami
PhD, Research unit of emergent materials, university Ferhat Abbas, Sétif-1, Algeria, riadh_bourzami@hotmail.com

Rima Kiche
Doctorante, Laboratoire d'Electrochimie et Matériaux (LEM). Département de physique, Faculté des sciences, université Ferhat Abbas, Sétif-1, Algérie, kiche.rima@univ-setif.dz

Abstract:
The present work performes an example of elaboration of a molecular phosphorus material, named Diethyl [hydroxy (4-methoxyphenyl) methyl] phosphonate (DH4MPMP). The structure was resolved using SXRD, then compared to the optimized geometry, the FTIR, NMR, UV-Vis. spectroscopies results were discussed experimentally and theoretically. The UV-Vis. spectrum exhibits a strong absorption in middle UV domain and an optical transmission in the visible one, the experimental thermal decomposition behavior was discussed through TGA analysis. Moreover, to be close from the experimental results, all DFT methods based on B3LYP/6-31G (d,p) calculated the frontier molecular orbitals and their energies were calculated. The calculations were again extended to the molecular electrostatic potential mapping; it shows negative potential areas localized around oxygen atoms as well as the positive localized around the hydrogen atoms. And also, the DFT calculates the second-order nonlinear optical properties based on the first static hyperpolarizability (β), the results show that the material might have nonlinear optical properties. At the end, the thermodynamic functions (entropy, enthalpy and heat capacity) were calculated from spectroscopic data as function of temperature adopting statistical method in the temperature range 100–1000K.

Keywords: *Bottom-up, self-assembly, spectral characterizations, nonlinear optic, thermochemistry, TGA, DFT.*

Introduction:

A decades after their discovery the phosphonate materials present various applications and are wieldy used in technologies by dint of their low cost and found potential application in the pharmaceutical industry and in optic.

The large literature related to the chemistry of phosphonates demonstrates an interesting field with many research and development opportunities. (Wu, 2010; Tajbakhsh, 2007; Goldeman, 2006; Mehri, 2018).

Organophosphonates are a type of functionally organophosphorus material with a particularly stable C–P bonds that has a wide range of uses in materials science and biological

Creative Commons Attribution-NonCommercial-NoDerivatives 4.0 International License (CC BY-NC-ND)

CCDC (/)

My Structure Details

Back to My Structures (/mystructures/)

Datablock: AYH3
Space Group: P-1, **Cell:** *a* 5.669Å *b* 7.554Å *c* 11.919Å, *α* 102.781(2)° *β* 94.472(2)° *γ* 110.550(2)°
Formula: C3 H7 N6 1+,Cl1 O4 1-,H2 O1, Temperature: 150 K

User Details

Reliability Score	2
2D Diagram	True
2D/3D Match	Full
2D/3D Last Edited	
User Compound Name	2,4,6-triamino-1,3,5-triazin-1-ium perchlorate monohydrate
User Identifier	Click to add some data

Additional Details

Deposition Number	2261769
Data Citation	Riadh Bourzami, Hakima Ait Youcef, Kiche Rima, Louiza Ouksel, CCDC 2261769: Experimental Crystal Structure Determination, 2023, DOI: 10.5517/ccdc.csd.cc2fxk97 (http://dx.doi.org/10.5517/ccdc.csd.cc2fxk97)
Refcode	OGAYEE
Compound Name	2,4,6-triamino-1,3,5-triazin-1-ium perchlorate monohydrate
Deposited On	08/05/2023
Additional Depositors	
Status	Published

Associated Publications

Publication	Created on	Modified on
Riadh Bourzami, Hakima Ait Youcef, Kiche Rima, Louiza Ouksel, *CSD Communication*, 2023	08/05/2023	08/05/2023

Add Publication

Structure Shared With

Name	Edit Rights	Sharing Rights

Share Structure

Associated Data

Raw data DOI

New Associated Data

Crystallographer details

Crystallographer name: Riadh Bourzami

Publishing name: Riadh Bourzami

Email address: riadh_bourzami@hotmail.com

Affiliation: University of Setif

ORCID iD: 0000-0002-3092-0006

Chemical diagram

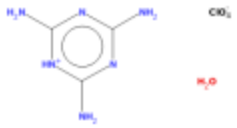

Source Information

File Name
AYH3_150K_12mar20_D8V_VD_archive_file001.cif

Datablock
data_AYH3

Deposition Type
web

Download Files (/mystructures/downloadmystructure/37bf2c90-97ed-ed11-96b9-00505695f620) Add files
View in Access Structures (/mystructures/viewinaccessstructures/37bf2c90-97ed-ed11-96b9-00505695f620)

Associated Files
AYH3_150K_12mar20_D8V_VD_archive-data_AYH3_file002.html

Subsets

Back to My Structures (/mystructures/)

Terms of Use (/TermsAndConditions/) Privacy Policy (/privacy/)

Follow CCDC:

CCDC (/)

My Structure Details

Back to My Structures (/mystructures/)

Datablock: LO2
Space Group: P-1, **Cell:** *a* 5.67Å *b* 7.684Å *c* 11.911Å, *α* 73.977(3)° *β* 85.455(3)° *γ* 66.927(3)°
Formula: C3 H7 N6 1+,Cl1 O4 1-,H2 O1, Temperature: 150 K

User Details

Reliability Score	2
2D Diagram	True
2D/3D Match	Full
2D/3D Last Edited	
User Compound Name	2,4,6-triamino-1,3,5-triazin-1-ium perchlorate monohydrate
User Identifier	Click to add some data

Additional Details

Deposition Number	2261403
Data Citation	Hkima Ait Youcef, Riadh Bourzami, Louiza Ouksel, Kiche Rima, CCDC 2261403: Experimental Crystal Structure Determination, DOI: 10.5517/ccdc.csd.cc2fx5h1 (http://dx.doi.org/10.5517/ccdc.csd.cc2fx5h1)
Refcode	OFUFOO
Compound Name	2,4,6-triamino-1,3,5-triazin-1-ium perchlorate monohydrate
Deposited On	08/05/2023
Additional Depositors	
Status	Published

Associated Publications

Publication	Created on	Modified on	
Hkima Ait Youcef, Riadh Bourzami, Louiza Ouksel, Kiche Rima, *CSD Communication*, 2023	08/05/2023	08/05/2023	
Hkima Ait Youcef, Riadh Bourzami, Louiza Ouksel, Kiche Rima	08/05/2023	08/05/2023	Edit

Add Publication

Structure Shared With

Name	Edit Rights	Sharing Rights

Share Structure

Associated Data

Raw data DOI

New Associated Data

Crystallographer details

Crystallographer name: Riadh Bourzami

Publishing name: Riadh Bourzami

Email address: riadh_bourzami@hotmail.com

Affiliation: University of Setif

ORCID iD: 0000-0002-3092-0006

Chemical diagram

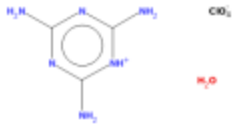

Source Information

File Name
LO2_150K_24oct19_D8V_VD_archive_file001.cif

Datablock
data_LO2

Deposition Type
web

Download Files (/mystructures/downloadmystructure/56fe05b3-96ed-ed11-96b9-00505695f620) Add files
View in Access Structures (/mystructures/viewinaccessstructures/56fe05b3-96ed-ed11-96b9-00505695f620)

Associated Files
LO2_150K_24oct19_D8V_VD_archive-data_LO2_file002.html

Subsets

Back to My Structures (/mystructures/)

Terms of Use (/TermsAndConditions/) Privacy Policy (/privacy/)

Follow CCDC: (ht... (ht... (ht... (ht...

CCDC (/)

My Structure Details

Back to My Structures (/mystructures/)

Datablock: MH1x3
Space Group: P21/c, **Cell:** *a* 13.798Å *b* 5.071Å *c* 16.647Å, *α* 90° *β* 91.869(2)° *γ* 90°
Formula: C9 H10 N5 1+,Cl1 O4 1-, Temperature: 150 K

User Details

Reliability Score	2
2D Diagram	True
2D/3D Match	Full
2D/3D Last Edited	
User Compound Name	2,4-diamino-6-phenyl-1,3,5-triazinium perchlorate
User Identifier	Click to add some data

Additional Details

Deposition Number	2412879
Data Citation	Kiche Rima, Louiza Ouksel, Riadh BOURZAMI, CCDC 2412879: Experimental Crystal Structure Determination, 2024, DOI: 10.5517/ccdc.csd.cc2lzst6 (http://dx.doi.org/10.5517/ccdc.csd.cc2lzst6)
Refcode	YUGVUV
Compound Name	2,4-diamino-6-phenyl-1,3,5-triazinium perchlorate
Deposited On	25/12/2024
Additional Depositors	
Status	Published

Associated Publications

Publication	Created on	Modified on
Kiche Rima, Louiza Ouksel, Riadh BOURZAMI, *CSD Communication*, 2024	25/12/2024	25/12/2024

Add Publication

Structure Shared With

Name	Edit Rights	Sharing Rights

Share Structure

Associated Data

Raw data DOI

New Associated Data

Crystallographer details

Crystallographer name: Riadh Bourzami

Publishing name: Riadh Bourzami

Email address: riadh_bourzami@hotmail.com

Affiliation: Setif university

ORCID iD: 0000-0002-3092-0006

Previous Revisions

Deposited O…	Email (/mystructures/structure…	CIF Filename (/mystruct…	Structure Factor Filenam…	Deposition Ty…
09/01/2025	riadh_bourzami@hotmail.com	Cif_file001.cif		web

1 5 items per page

1 - 1 of 1 items (/mystructures/structuredetails/716714dd-9cc2-ef11-96cd-00505695281c)

Chemical diagram

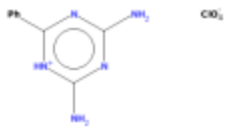

Source Information

File Name
MH1x3_Tamb_07juin24_APEX_VD_archive_file001.cif

Datablock
data_MH1x3

Deposition Type
web

Download Files (/mystructures/downloadmystructure/716714dd-9cc2-ef11-96cd-00505695281c) Add files
View in Access Structures (/mystructures/viewinaccessstructures/716714dd-9cc2-ef11-96cd-00505695281c)

Associated Files
MH1x3_Tamb_07juin24_APEX_VD_archive-data_MH1x3_file002.html

Subsets

Back to My Structures (/mystructures/)

Terms of Use (/TermsAndConditions/) Privacy Policy (/privacy/)

Follow CCDC:

Abstract

This study investigates two new ionic organic-inorganic hybrid materials—2,4-diamino-6-phenyl-1,3,5-triazinium perchlorate and 2,4,6-triamino-1,3,5-triazin-1,3-dium bisperchlorate monohydrate,—and ionic liquids (ILs). The hybrid materials exhibit good transparency in the visible range and UV absorbance, with thermal stabilities of 290 °C and 256 °C, respectively, stabilized by hydrogen bonding. The ILs demonstrate high thermal stability (>300 °C), a low glass transition temperature (-34 °C), anisotropic optical responses, and visible transparency, with overlapping UV absorption bands. Density Functional Theory (DFT) calculations reveal high hardness, stability, and low reactivity for the ILs, providing insights into molecular orbitals and electrostatic potentials. Modified carbon paste electrodes (CPEs) show high sensitivity, faster redox reactions, and efficient charge transfer, confirmed by electrochemical studies. These findings highlight the potential of hybrid materials and ILs for optoelectronic and electrocatalytic applications.

Résumé

Cette étude porte sur deux nouveaux matériaux hybrides ioniques organiques-inorganiques : le perchlorate de 2,4-diamino-6-phényl-1,3,5-triazinium (monoclinique) et le 2,4,6-triamino-1,3,5-triazine- Bisperchlorate de 1,3-dium monohydraté (triclinique) — ainsi que des liquides ioniques (IL), analysant leurs propriétés structurelles, thermiques, optiques et électrocatalytiques. Les matériaux hybrides présentent une bonne transparence dans le domaine visible et une bonne absorbance UV, avec des stabilités thermiques de 290 °C et 256 °C, respectivement, stabilisées par liaison hydrogène. Les IL démontrent une stabilité thermique élevée (> 300 °C), une faible température de transition vitreuse (-34 °C), des réponses optiques anisotropes et une transparence visible, avec des bandes d'absorption UV qui se chevauchent. Les calculs de la théorie fonctionnelle de la densité (DFT) révèlent une dureté, une stabilité et une faible réactivité élevées pour les IL, fournissant ainsi un aperçu des orbitales moléculaires et des potentiels électrostatiques. Les électrodes en pâte de carbone modifiée (CPE) présentent une sensibilité élevée, des réactions redox plus rapides et un transfert de charge efficace, confirmés par des études électrochimiques. Ces résultats mettent en évidence le potentiel des matériaux hybrides et des IL pour les applications optoélectroniques et électrocatalytiques.

الملخص

تبحث هذه الدراسة في مادتين هجينتين عضويتين وغير عضويتين أيونيتين جديدتين 2،4 -ديامينو-6-فينيل-1،3،5-تريازينيوم بيركلورات (أحادية الميل) و2،4،6-تريامينو-1،3،5-تريازين- 1،3 ثنائي كلورات الصوديوم أحادي الهيدرات (تريكلينك) - إلى جانب السوائل الأيونية(ILs) ، لتحليل خصائصها الهيكلية والحرارية والبصرية والتحفيزية الكهربائية. تُظهر المواد الهجينة شفافية جيدة في النطاق المرئي وامتصاصًا للأشعة فوق البنفسجية، مع ثبات حراري يبلغ 290 درجة مئوية و256 درجة مئوية، على التوالي، ويتم تثبيته بواسطة الروابط الهيدروجينية. تُظهر ILs ثباتًا حراريًا عاليًا (<300 درجة مئوية)، ودرجة حرارة منخفضة للتزجج (-34 درجة مئوية)، واستجابات بصرية متباينة الخواص، وشفافية مرئية، مع نطاقات امتصاص للأشعة فوق البنفسجية متداخلة. تكشف حسابات نظرية الكثافة الوظيفية (DFT) عن صلابة عالية واستقرار وتفاعل منخفض لـILs ، مما يوفر نظرة ثاقبة للمدارات الجزيئية والإمكانات الكهروستاتيكية. تُظهر أقطاب معجون الكربون المعدلة (CPEs) حساسية عالية، وتفاعلات الأكسدة والاختزال الأسرع، ونقل الشحنة بكفاءة، وهو ما تؤكده الدراسات الكهروكيميائية. تسلط هذه النتائج الضوء على إمكانات المواد الهجينة و ILsللتطبيقات الإلكترونية البصرية والتحفيز الكهربائي.